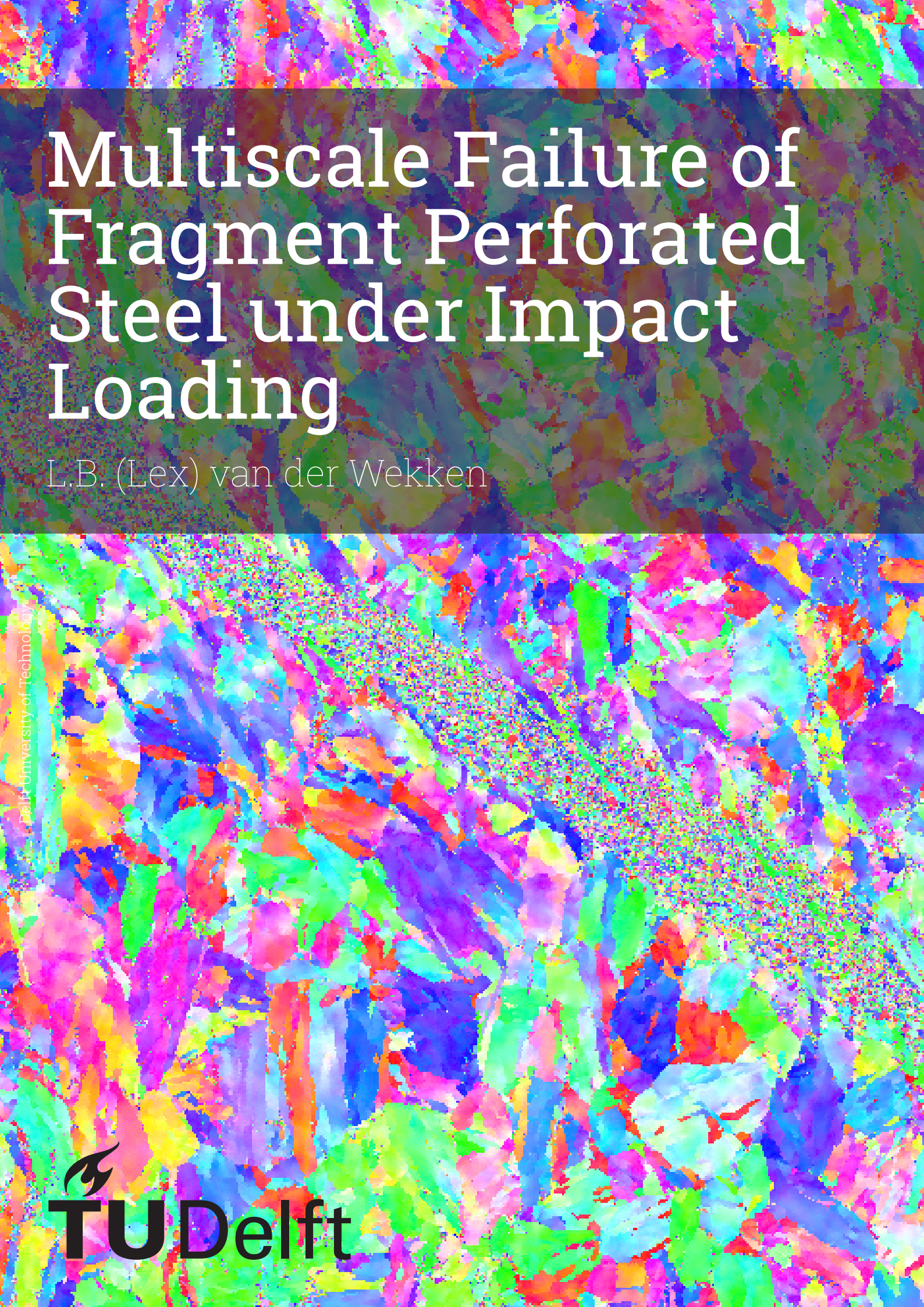
Multiscale Failure of Fragment Perforated Steel under Impact Loading

L.B. (Lex) van der Wekken



Delft University of Technology

TU Delft

Multiscale Failure of Fragment Perforated Steel under Impact Loading

by

L.B. (Lex) van der Wekken

Student number 4282574

Master thesis date 19 / 09 / 2025







Commando Materieel en IT
Ministerie van Defensie

Supervisor TU Delft:	Dr. Vera Popovich
Supervisor TNO:	Dr. Casper Versteylen
Faculty:	Mechanical Engineering, Delft
Department:	Materials Science and Engineering

Abstract

The survivability of armour steel under multi-threat loading is influenced by microstructural damage initiated by fragment perforation. This damage affects the way the material deforms and fractures under subsequent blast-induced loading. This thesis investigates the failure micro-mechanisms in Armox 440T after perforation by 20 mm Fragment Simulating Projectiles (FSPs) at 900 m/s and 1600 m/s, followed by Drop-Weight Impact (DWI) loading that simulates blast-induced blast wave loading. A multiscale approach using high-speed digital image correlation (DIC), fractography using Optical Microscopy (OM) and Scanning Electron Microscopy (SEM), Electron Backscatter Diffraction (EBSD) with Kernel Average Misorientation (KAM) mapping, and microhardness profiling reveals the microstructural response to plastic deformation and failure by the formation of adiabatic shear bands (ASBs) and the ductile crack growth phenomena.

Fragment perforation produces complex networks of deformed (dASB) and transformed (tASB) adiabatic shear bands concentrated at the hole surface. With increasing FSP velocity, (I) plug and hole size increases, (II) local hardness peaks intensify reaching $\approx$ 650 HV0.01 within tASBs, and (III) The number of ASBs, branching and junction frequency increases. Microcracks are commonly found near dense tASB clusters at the hole surface and internally in tASB junctions indicating a reduced dynamic fracture tolerance.

Under DWI, cracks initiate at the hole surface and initially propagate perpendicular to the length of the plate, then change direction to $\approx 45^{\circ}$ shear accompanied by pronounced necking. All fracture surfaces show ductile microvoid coalescence behaviour. The crack centre fails under tensile tearing, which transition into shear failure towards the edges. OM and SEM reveal that microcracks from perforation form under microvoid coalescence and void sheeting. EBSD/KAM mapping on adiabatic shear bands shows ultrafine equiaxed grains and low dislocation density within tASBs, confirming severe strain localisation and dynamic recrystallisation.

Collectively, the results show that tASB networks constitute preferential crack paths that lower the energy absorption capacity in blast impact loading. These findings offer new insights into ASB-enabled damage evolution and provide critical microstructural constraints for modelling and design of armour systems capable of withstanding multi-threat environments.

Keywords: Armox 440T, adiabatic shear bands, ballistic perforation, blast impact, plugging, failure mechanisms.

Acknowledgements

It is with deep gratitude that I reflect on the journey that led to the completion of this thesis, a process enriched by the support, guidance, and encouragement of many exceptional people and organisations.

First and foremost, I would like to express my heartfelt gratitude to my TU Delft supervisor, Dr. Vera Popovich, whose wisdom, patient guidance, and support were invaluable at every stage of my research. Your insightful feedback and encouragement have greatly contributed to the shape and substance of this work. I am equally grateful to my TNO supervisor, Dr. Casper Versteylen, for his practical perspective and for challenging me to think concisely while maintaining a critical approach. The thoughtful questions and constructive feedback of both supervisors have helped refine my arguments and strengthen my conclusions for which I am deeply grateful.

I am sincerely grateful to my collaborators and colleagues in the TU Delft Mechanical Engineering Labs, especially Dr. Virgínia Morete Barbosa Bertolo for her support, technical assistance, motivation, and patience during the initial phase of this thesis. Her scientific dedications and guidance have helped me significantly. Her expertise with EBSD has helped me greatly and provided me with valuable insight. My thanks go out to the technical staff at the TU Delft and at TNO who have provided me with valuable resources and acquired measurement data. I specifically thank Ir. Arjun Sood for his contribution regarding the final EBSD results, Dhr. R.W.A. Hendrikx for the XRF results, Ir. J. de Moraes Siedschlag for her LECO combustion analysis, and Drs. R.M. Huizinga for his XRD measurements and ASB phase recognition.

I would like to express my sincere appreciation to TNO for their generous support, technical expertise, insight and feedback, access to their advanced resources, facilities, and work environment. A sincere thanks to the numerous colleagues that I have had the pleasure to work with, who have challenged me and that have contributed to this wonderful experience.

This research would not have been possible without the generous support and resources provided by Commando Materieel en IT (COMMIT) to the project. I am forever grateful for this opportunity, their interest and focus in this thesis research, and the stimulating multidisciplinary environment that they have offered throughout my thesis. In particular, I would like to thank Weihong He and Wouter Nederstigt for their close collaboration, engaging discussions, and insightful expertise that have contributed to this thesis.

On a more personal note, a heartfelt thanks goes to my parents and my partner, their empathy, patience, and endless support have been my greatest comfort during the most challenging times. Their unconditional love and encouragement have provided me with the motivation and perseverance required to complete my academic journey.

To my friends and all those who brightened my days with laughter, support, and advice, thank you. Each of you has contributed, directly or indirectly, to the completion and quality of this thesis and for that I am profoundly grateful.

Thank you all.

L.B. (Lex) van der Wekken
Delft, September 2025

Contents

Abstract i

Acknowledgements ii

Nomenclature ix

1 Introduction 1

Introduction 1
1.1 Current Challenges . . . 2
1.2 Master thesis objectives . . . 3
1.3 Thesis Outline . . . 3

2 Literature review 5
2.1 Armour steels . . . 5
2.1.1 Ballistic conditions . . . 5
2.1.2 Ballistic testing methods . . . 7
2.2 Fragment impact . . . 8
2.2.1 Fragment simulating projectiles . . . 9
2.2.2 Ballistic limit . . . 10
2.2.3 Perforation by plugging . . . 10
2.3 Adiabatic shear bands . . . 13
2.3.1 Adiabatic shear band formation . . . 13
2.3.2 strain-rate effect . . . 14
2.3.3 Shear band temperature . . . 15
2.3.4 Flow stress and fracture strain . . . 16
2.3.5 Strain hardening . . . 18
2.3.6 Plasticity models . . . 18
2.3.7 Crack initiation and failure . . . 18
2.4 Blast impact loading . . . 20
2.4.1 Stress state models . . . 22
2.4.2 Stress concentration . . . 24

3 Material & Methodology 27
3.1 Armox 440T . . . 27
3.2 Ballistic testing methods . . . 27
3.2.1 Material and test geometry . . . 28
3.2.2 FSP Perforation procedure . . . 29
3.2.3 Drop Weight Impact Testing . . . 29
3.3 Microstructural characterisation . . . 29

4 Results and discussion 33
4.1 Fragment perforated hole . . . 33
4.1.1 Material deformation . . . 36
4.2 Adiabatic shear band characterisation . . . 42
4.3 Blast impact failure . . . 50
4.3.1 Fractography . . . 50
4.3.2 Strain energy absorption . . . 52

5 Conclusions 55

6 Recommendations 56

References **58**

A Appendix A: Base material and sample characterisation **64**
A.1 Optical microscopy of base material 64
A.2 Sample characterisation 66
A.3 Fractured surface cross section analysis 66
A.4 Adiabatic shear bands along hole surface 70
A.5 EDS results of Adiabatic shear band 71

B Appendix B: External result files **72**
B.1 XRF results on Armox 440T 72
B.2 XRD results on Armox 440T focussed on tASB and undeformed material 74
B.3 Extended Drop Weight Test DIC analysis 78

List of Figures

1.1 Dutch Hr.Ms Zeven Proviciën firing a Harpoon anti-ship missile (AGM-84) [4]. 2
1.2 HMS Boxer(F92) after being hit by 2 Harpoon anti-ship missiles during a SINKEX test [5]. 2

2.1 Sketch of missile strike, adapted from [19]. 6
2.2 Simulation of pressure distribution from 1-5 GPa in a depleted uranium alloy penetrator at 1650 m/s [10, 29]. 6
2.3 Collection of fragments from physical test by Hiroe et al. [35]. 9
2.4 Technical drawing of the MIL-DTL-46593B standard 20 mm FSP (dimensions in inches) [39]. 9
2.5 Post-impact 20 mm FSPs from tests on Armox 440T, a) steel FSP shot at 373 m/s, b) copper FSP shot at 328 m/s, c) steel FSP shot at 1016 m/s [36]. 10
2.6 (a) Schematic of stress wave generation, (b) Generic penetration process indicating different failure modes [12, 23, 24]. 11
2.7 Stress wave diagram on same material impact [28, 45]. 11
2.8 Schematic illustration of (a) plugging, and (b) photograph of plugging failure by FSP along adiabatic shear bands [10, 12, 33]. 12
2.9 Photographs of post impact panels impacted at various velocities of Armox 440T with 20 mm FSP [36]. 12
2.10 Three stage model of plug formation and shear stresses: (a) Stage I, (b) during stage II, (c) end of stage II, (d) Stage III [49]. 13
2.11 Shear band formation (A) Grid patterns shown in the three separate stages at a strain-rate of 1600 s^{-1} (B) A partial fracture shown at a local shear strain of 500% [25][52]. . . 14
2.12 Different types of adiabatic shear bands and crack formation under compression in Armox 500T deformed at 3900 s^{-1}: (a) optical micrographs, (b) IPF and grain size distribution in tASB [31, 53]. 15
2.13 Evolution of adiabatic shear band, a) Progression scheme, b) (a-e) Schematic illustration dynamic recrystallisation; (a) dislocation distribution, (b) cell elongation, (c) subgrain dislocation accumulation, (d) subgrain breakup, (e) reorientation and boundary formation [47, 53]. 16
2.14 Inverse pole figure of transformed adiabatic shear band in an interstitial free steel [47]. . 17
2.15 Thermal diffusion distance and strain-rate for copper, steel and titanium. The horizontal line indicates a typical sample size [55]. 18
2.16 Evolution of the Integral Taylor-Quinney coefficient with strain for different materials, strain and strain-rates [61]. 19
2.17 The effect of strain-rate of high strength armour grade steels on (a) strength and (b) ductility [13]. 20
2.18 Flow stress unloading surrounding material, t1 and t2 represent the material stress lines at different moments in time [67]. 20
2.19 Instantaneous strain hardening exponent n for different materials [61]. 21
2.20 (a) Fracture found in plugged region in armour steel, (b) Ductile microvoid coalescence in tASB [25, 44]. 22
2.21 Static blast pressure parameters and terminology used for analyses of far-field blast [12]. 23
2.22 Propagation of blast wave and rupture of structure up to 7.2 ms, with red to blue indicating high to low low pressure distribution [19]. 24
2.23 Through thickness crack loaded from both sides [80]. 24
2.24 Stress concentration on a plate with a circular hole under horizontal tensile loading [82]. 25
2.25 Through thickness plastic zone at the crack tip in a plate of intermediate thickness [80]. 26
2.26 Planes of maximum shear stress at the crack tip for (a) plane stress and (b) plane strain [80]. 26

2.27 Single shear fracture and transition from double to single shear fracture during tensile tests on a centre cracked specimen [80]. 26

3.1 Armox 440T martensite microstructure, (a) 3D presentation at 300X zoom and (b) magnification X2000, the black dots are impurities from the preparation process, no inclusions, precipitates or impurities are found. 28
3.2 Tensile test samples, (a) technical drawing drop weight tower samples, plate thickness is 6.4 mm, (b) Orientation relation with respect to the rolling direction and sample length [84]. 30
3.3 Loading condition icons with colour coding related to the the perforation velocity in m/s as indicated. 31
3.4 Drop weight impact tower setup at TNO Structural Dynamics lab. 32

4.1 Drop weight impact test (a) DIC result of strain at crack initiation and, (b) top view of plate after perforation and drop weight tower test. 34
4.2 Perforated plates and fractured halves after DWI loading, (a-b) Photograph of perforated plates at 900 m/s entrance and exit side, optical microscopy of fractured halves of (c-d) two plates shot at 900 m/s and (e) at 1600 m/s,all scale bars are 2000 μm. 35
4.3 Shear angle strain measurements of global deformation on A4-1600 sample divided into three sections, entranceside, exitside and near hole shear angle. 36
4.4 Material flow on similar cross-sections of holes as indicated in (a), Material flow behaviour where the red arrows indicate shear deformation lines and the blue lines follow global deformation behaviour, (b) Shot at 900 m/s, (c) shot at 900 m/s and drop weight tested, (d) shot at 1600 m/s and drop weight tested, scale bar of b-d is 1000 μm. 38
4.5 Perforated at 900 m/s, (a) micrograph of cross-section with section indication for the similar samples (b-c), scalebar is 1000 μm, (b) micrograph of lower area at end of entrance effect, scale bar is 100 μm, (c) micrograph of upper area with remnant piece of tASB scale bar is 20 μm 39
4.6 Microscopy of sample cross-sections with (a-c), Optical microscopy of H1, A1, A4; (d-f) According hardness profiles H1, A1, A4. 40
4.7 Average hardness from hardness profiles of base material, cross-sections near holes shot at 900 m/s and 1600 m/s and micro hardness measurements of transformed adiabatic shear bands 41
4.8 Hardness profile of high hole surface region 1600 m/s shot plate with (a) Optical micrograph with section indication, (b) 1000x magnification showcasing several ASBs and profile indication, (c) hardness profile of deformed area near ASB 42
4.9 High magnification SEM of crack initiation and ASB interactions in the entrance region of 900 m/s-H1, (a) micrograph with highlighted sections, (b) SEM of crack initiation in tASB at the surface plate front, (c) SEM of ASB interaction in the transition region. 44
4.10 Adiabatic shear bands in 900 m/s-A1 plate, (a) OM showcasing presence of adiabatic shear bands and section indication, (b) higher magnification at entrance side, red arrows indicate cracks, blue arrows indicate ASB branching, (c) SEM of crack initiation and growth in tASB at hole surface, (d) SEM of crack tip of central crack growing out of ASB. 45
4.11 Presence of adiabatic shear bands in 1600 m/s-A4, (a) showcases the location and abundance of ASBs, (b) section near hole surface, red arrows indicate cracks, blue arrows indicate ASB branching, and highlighted sections for SEM micrographs (c-d) of high density ASB region with thickness measurements, (d) Shows clear void coalescence crack growth behaviour. 46
4.12 EBSD of Base material in Rolling - Normal direction with a) Image Quality map, b) Inverse Pole figure map and c) Prior Austenite from Nishiyama-Wassermann relation 48
4.13 EBSD of a drop weight loaded 1600 m/s sample of a centrally located tASB at 1 mm from hole surface a) Image Quality map, c) Inverse Pole figure map, e) Kernel average misorientation map and an tASB at the entrance side surface at 2 mm from the hole surface b) Image Quality map, d) Inverse Pole figure and f) Kernel Misorientation map . 49

4.14 Photograph (a) of fracture surface, (b-c) surface sectioned at the fracture direction transition of two fracture surfaces of 1600 m/s samples; left horizontal crack, right diagonal crack direction. Both show increased necking behaviour in diagonal crack direction (right side). 51
4.15 Cross section of shear direction fractured surface of a sample shot at 900 m/s used for quantification of necking. 52
4.16 SEM of fractured surfaces (a) Center of initially grown crack(b) at the edge of perpendicular crack, (c) fractured surface at change in direction, (d) higher magnification around crack deflection region. 54

A.1 Base material cross-section with horizontally the transverse and vertically the normal direction, (a) Full thickness, (b) 500X magnification 64
A.2 Base material cross-section with horizontally the rolling and vertically the normal direction, (a) Full thickness, (b) 500X magnification 65
A.3 Base material surface with horizontally the rolling and vertically the transverse direction, (a) Polished top surface of plate, (b) 500X magnification 65
A.4 Overview of fracture surface samples as taken from A1-900 and A4-1600 66
A.5 Cross section of fractured surface of plate A1-900 m/s, cross section 2b in shear direction of the full fracture, (a) Full cross section, (b) Zoomed in on central crack, (c) higher magnification of local crack interruption. 67
A.6 Cross section of fractured surface of plate A4-1600 m/s, cross section 1b in initial section of the full fracture, (a) Full cross section, (b) Zoomed in on the backside of the plate showing adiabatic shear band formation from DWI test. 68
A.7 Cross section of fractured surface of plate A4-1600 m/s in shear direction of the full fracture showing clear necking behaviour, (a) cross section 3 showing V crack shape, (b) cross section 4 showing single shear direction crack shape. 69
A.8 Leftover transformed adiabatic shear band pieces along shot hole surface at 900 m/s . 70
A.9 EDS results on transformed adiabatic shear band from sample A4-1600 m/s, showing no elemental segregation. 71

List of Tables

2.1 Characteristics of different strain-rate, mechanical and material responses, and stress states. Adapted from [12]. . . . 7
2.2 Armour steel classes defined by DEF(AUST) 8030 with specified hardness and impact toughness limits [13]. . . . 8
2.3 Johnson-Cook material parameters for Armox 440T and a Mild steel [76]. . . . 19

3.1 Mechanical properties of Armox 440T based on SSAB certificate. . . . 27
3.2 Chemical composition of Armox 440T. . . . 27
3.3 Sample FSP velocity and drop weight height . . . 28
3.4 Ballistic testing induced strain-rate. . . . 29

4.1 Perforation diameter and crack length of full fracture with comparison of perpendicular and diagonal crack growth. . . . 33
4.2 The average shear deformation expressed in von Mises equivalent strain for perforation at 900 m/s and 1600 m/s. . . . 37
4.3 Adiabatic shear band analysis comparing 900 m/s and 1600 m/s. . . . 47
4.4 Material grain size at different positions with respect to the perforation at 1600 m/s. . . . 48
4.5 Necking behaviour of full fracture at different crack directions, perpendicular to plate length (horizontal) and in shear direction (diagonal). . . . 50
4.6 Fracture surface dimple size comparison . . . 53

A.1 Sample characteristics and hole diameter. . . . 66
A.2 Sample full fracture analysis, total length of surface of the sections perpendicular and diagonal to the loading direction. . . . 66

Nomenclature

Abbreviations

Abbreviation	Definition
ARL	Association of Research Libraries
ASB	Adiabatic Shear Band
BCC	Body Centred Cubic
BCT	Body Centred Tetragonal
COMMIT	Commando Materieel & IT
dASB	Deformed Adiabatic Shear Band
DBTT	Ductile to Brittle Transition Temperature
DIC	Digital Image Correlation
DRX	Dynamic Recrystallisation
DWI	Drop Weight Impact
EBSD	Electron Backscatter Diffraction
EDS	Energy Dispersive Spectroscopy
FCC	Face Centred Cubic
FSP	Fragment Simulating Projectile
HAZ	Heat Affected Zone
HBW	Brinell Hardness Wolfram
HRTEM	High Resolution Transmission Electron Microscopy
IPF	Inverse Pole Figure
KAM	Kernel Average Misorientation
OM	Optical Microscopy
SEM	Scanning Electron Microscopy
SSAB	Swedish Steel Oxelösund AB
TAM	Thermal activation model
tASB	Transformed Adiabatic Shear band
TNO	Nederlandse Organisatie voor toegepast natuur-wetenschappelijk onderzoek
TRIP	Transformation Induced Plasticity
XRD	X-ray Diffraction
XRF	X-ray Fluorescence

Symbols

Symbol	Definition	Unit
a	Crack length	$[nm]$

Symbol	Definition	Unit
B	Flow stress	$[MPa]$
C	Stress concentration factor	$-$
C	Strain-rate parameter	$-$
C_p	Specific heat coefficient	$-$
d	Grain size	nm
ΔG_0	Activation energy	J
K_B	Carbon sensitive constant	$[^\circ C/nm]$
k_y	Hall-Petch Strengthening constant	$MPa\ \sqrt{nm}$
m	Thermal softening parameter	$-$
M_f	Martensite Finish temperature	$^\circ C$
M_s	Martensite Start temperature	$^\circ C$
n	Strain hardening parameter	$-$
T	Temperature	$^\circ C$
T_R	Referemce temperature	$^\circ C$
ΔT	Temperature difference	$^\circ C$
V	Velocity	m/s
${V_V}^{\alpha'}$	Martensite volume fraction	$-$
W	Work	J
x	Sample value	$-$
$\bar{x}$	Sample mean average	$-$
α	Thermal diffusivity	$\frac{m^2}{s}$
β	Taylor-Quinney capacity	$\frac{J}{kg\ K}$
$\dot{\epsilon}$	Strain-rate	$-$
$\dot{\epsilon}$	Reference strain-rate	$-$
ρ	Density	$\frac{kg}{m^3}$
σ	Flow stress	MPa
σ_0	Standards stress for dislocation movement	MPa
σ_0^*	Temperature dependent flow stress	MPa
σ_G	Athermal dependent flow stress	MPa
σ_y	Yield stress	MPa
$\sigma_{st.h}$	Standard Deviation Hardness	$HV1.0$

1

Introduction

The material behaviour of steel under ballistic conditions has been a subject of research since the construction of armoured vehicles in 1915 [1]. Subsequently, these foundational studies have been extended to naval vessel protection, guiding the engineering of steel hulls and armour systems. The advancements in modern weaponry leading to an increasing threat of anti-ship missiles, and the persistent threats posed by high-velocity fragmentation and blast events present an urgent challenge to the safety, survivability, and operational integrity of naval vessels. Steel remains a primary material for critical structures, bulkheads, protective shielding, and hulls because of its high tensile strength, toughness, and cost-effectiveness.

Ballistic impact presents a critical hazard in both civilian and military applications. High-velocity fragments can cause catastrophic failure, material fragmentation, and loss of life. The global frequency of ballistic and blast incidents is increasing, driven by geopolitical distress that affects an increasing number of people. Cross-border conflicts as seen in Ukraine-Russia, humanitarian crisis targeting infrastructure and civil areas between Israel and Palestine, rebels targeting cargo ships as seen near the Yemen coast, and civil war seen in Sudan and the Democratic Republic of Congo, leading to causalities by landmines, improvised explosive devices, rocket-propelled grenades, aerial missile and drone strikes, and anti-ship missile strikes. These events may form high-velocity fragments and debris that induce localised damage or penetrate the material upon impact. Subsequently, the high-pressure blast wave produced by the explosion impacts these structures to compromise structural integrity. Consequently, understanding metallic failure under high-rate impact has become an increasingly relevant research field in weapon and defence applications.

Among the many potential targets, marine structures and infrastructure are at the intersection of these threats. The maritime sector has long served as the cornerstone of the global economy by facilitating international trade, energy supply chain through infrastructure such as pipelines and cable networks, as well as oil, gas and offshore wind. Beyond these economic functions, maritime activities contribute to environmental sustainability, cultural exchange, and global security. To protect the global stability, naval vessels must be able to resist a wide variety of threats during peacekeeping missions. These threats range from small-arm weaponary to high-velocity anti-ship missiles. Anti-ship missiles such as the Harpoon (AGM-84) shown in Figure 1.1 can be fired from land, aircraft, and frigates. The destructive force of anti-ship missiles poses a major threat. Naval vessels need to be well protected. Advanced defence systems are essential in both the efficiency of naval deployment and crew safety. When effective close-in weapon systems, such as the Dutch Goalkeeper system [2] fails to intercept an incoming missile, the ship relies on its passive defences [3].

Upon impact the missile penetrates the hull and explodes inside the ship's compartments. The resulting damage typically occurs in two rapid phases. First, high-velocity fragments perforate and compromise the blast resistance of the internal structure. Then, the subsequent blast wave inflicts further damage aiming to incapacitate vital equipment, immobilise the crew, and undermine the structural integrity, cascade damage to multiple ship compartments and cause flooding and fires. Figure 1.2 illustrates the

damage caused after two Harpoon anti-ship missile strikes on the British HMS Boxer during a SINKEX test. Resistance to this missile threat can be enhanced by the addition of armour steel plates to the internal structure.



Figure 1.1: Dutch Hr.Ms Zeven Provinciën firing a Harpoon anti-ship missile (AGM-84) [4].

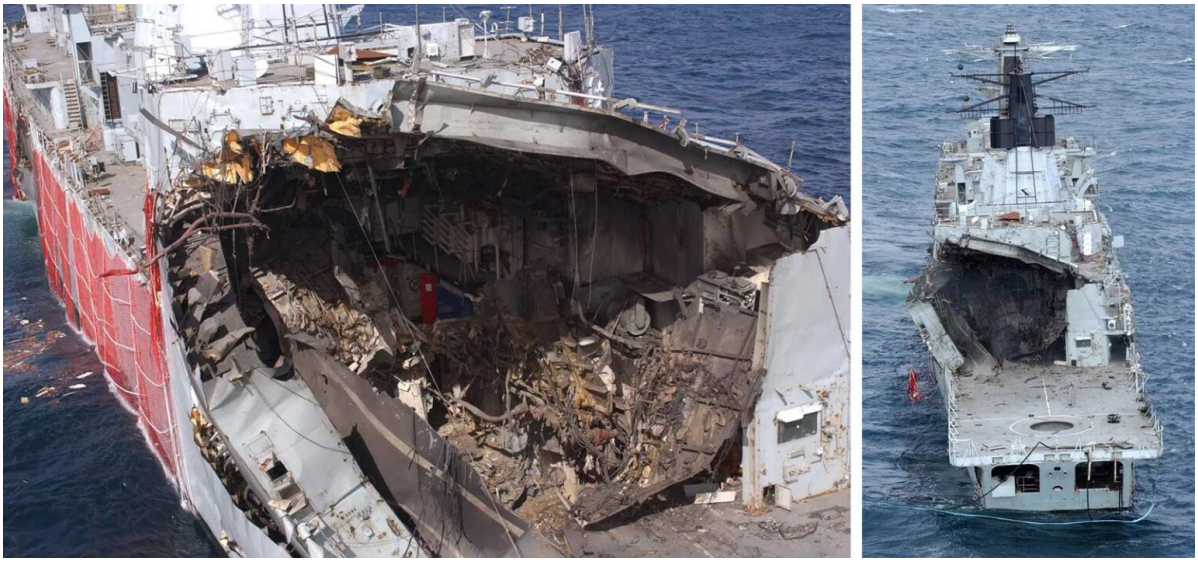


Figure 1.2: HMS Boxer(F92) after being hit by 2 Harpoon anti-ship missiles during a SINKEX test [5].

1.1. Current Challenges

Considerable research on material resistance to projectile and fragment perforation and blast impact loading is available [1, 6–9]. However, the same microstructural characteristics that provide high hardness needed for resistance against perforation can promote strain localisation at extreme strain-rates. The central engineering problem is that after fragment perforation the material has a significantly distorted and damaged microstructure, dominated by adiabatic shear bands (ASBs). These ASBs are narrow zones of intense plastic deformation that induce a material property gradient, act as crack initiators, and facilitate crack growth paths compromising the residual impact resistance [10, 11].

Current design methods under-represent this coupling: they treat perforation and blast largely in isolation, with limited microstructure-based links between the two. The failure criteria for homogeneous steel plates remain insufficiently characterised, from the onset of microstructural damage to macrostructural collapse [12–15].

The urgency of understanding these failure mechanisms is emphasised by the rapid evolution of military threats and the operational demands placed on modern fleets. Without a robust predictive framework for multiscale failure designs and vulnerabilities, underestimating risk and vulnerabilities can result in catastrophic failure. The performance of steel in dynamic impact conditions directly influences the survivability of key compartments, the safety of the crew, and the seaworthiness of the naval vessel. By advancing predictive tools that link microstructural behaviour with macrostructural performance, this thesis aims to enhance next-generation design strategies that guarantee safety and improve operational readiness.

Despite extensive investigations into the geometric and material discontinuities induced by complex strain localisation, dynamic fracture mechanisms, and scale-dependent energy dissipation, conventional modelling approaches often fail to capture these phenomena accurately at the relevant scales. Experimental studies face additional challenges in reproducing the high strain-rates and boundary conditions characteristic of naval environments with sufficient accuracy.

1.2. Master thesis objectives

This thesis is part of a larger project regarding failure mechanisms of ballistically perforated steel under impact loading was initiated by the Commando Materieel en IT (COMMIT) departments of the Dutch Ministry of Defence, in collaboration with the Dutch organisation for Toegepast Natuurwetenschappelijk Onderzoek (TNO) and TU Delft. The steel grade Armox 440T used for this thesis is seen as an interesting candidate to resist the combined effect of fragment perforation and blast loading. TNO has performed destructive testing using Fragment Simulating Projectiles (FSP) and a Drop Weight Impact (DWI) test setup as means to impose controlled blast loading conditions.

This thesis aims to establish microstructural to macrostructural links between fragment perforation and blast-induced deformation in Armox 440T. Optical microscopy and scanning electron microscopy (SEM) are used to determine microstructural changes around the perforation and enables high magnification fractography, Micro-hardness profiling is applied to determine localised changes in the mechanical properties due to deformation and the presence of adiabatic shear bands. Electron Backscatter Diffraction (EBSD) microscopy enables microstructural characterisation in and around adiabatic shear bands. Further results are backed by X-Ray Fluorescence (XRF) and X-Ray Diffraction (XRD) results. These results aim to answer the following research questions.

- **How do the microstructural changes induced by fragment perforation affect the residual impact resistance of Armox 440T?**
- **What are the dominant failure mechanisms during fragment perforation?**
- **Which micro-mechanisms govern failure under blast impact loading?**
- **How does adiabatic shear band formation influence blast resistance after fragment perforation?**

By integrating advanced microscopy techniques and mechanical profiling, this thesis aims to uncover the micro-mechanisms that govern failure in Armox 440T under multi-threat conditions. The insights gained will inform the design of steel structures with enhanced survivability in naval environments.

1.3. Thesis Outline

This thesis provides the reader with a comprehensive scientific research report on the characterisation and failure mechanisms of material at the micro-scale and macro-scale of Armox 440T and provides answers to the stated objectives. The content is structured to provide a clear understanding of the current available literature, present the applied methodology, results, and discussion, finishing with the conclusions and recommendations as listed below:

- **Chapter 2 - Literature Review:** Reviews present literature on armour steels, ballistic impact

physics, ASB formation and evolution, and blast loading mechanics. Establishes the theoretical basis for linking perforation-induced microstructural damage with blast impact failure.

- **Chapter 3 - Materials & Methodology:** Describes material properties of Armox 440T, sample geometries, ballistic and drop weight impact loading methods and an intricate set of material characterisation techniques.
- **Chapter 4 - Results and Discussion:** Presents results separated into three sections:
  - **Section 4.1 - Fragment perforation:** Provides measurements and microscopy of hole geometry, deformation zones, morphology and material flow.
  - **Section 4.2 - Adiabatic shear band characterisation:** Analysis and characterisation of ASBs, crack nucleation, and failure mechanism related to fragment perforation.
  - **Section 4.3 - Blast impact failure:** Describes the evolution of the crack path under DWI, the analysis of the fracture surface, and the correlations with pre-existing ASB networks.
- **Chapter 5 - Conclusions:** Presents the key findings to directly answer the research questions, highlighting the mechanisms by which perforation damage dictates blast performance.
- **Chapter 6 - Recommendations:** Offers methodological refinements, experimental extensions, and future research directions to improve predictive models and armour design.

2

Literature review

2.1. Armour steels

Over the past century, armour steels have undergone significant advancements. Early protective systems relied on heavy medium carbon, low alloy steel grades such as rolled homogeneous armour plates of $260 - 310$ Brinell Hardness (HBW) exceeding 100 mm in thickness. However, advances in kinetic energy weaponry and armour-piercing rounds during the 1980s and early 2000s required more sophisticated armour designs. This evolution led to the development of ultra-high hardness steels of $360 - 620$ HBW intended as add-on systems, as demonstrated by Swedish Steel AB (SSAB) Armox grades and collaborations with the Association of Research Libraries (ARL) [16, 17]. These materials are engineered not only to resist penetration by high-speed fragments but also to absorb and dissipate the energy imparted by subsequent blast loading. However, toughness decreases with increasing hardness. The continual refinement of alloy compositions and heat treatment processes has enabled these steels to achieve yield strengths that often exceed 1100 MPa, coupled with a good work hardening capacity essential for dynamic impact resistance and prevention of brittle failure [13–15].

2.1.1. Ballistic conditions

Modern naval vessels employ a compartmentalised internal structure, where watertight compartments are separated by robust metal bulkheads [18]. This design not only reinforces the structural integrity of the vessel, but also limits the spread of damage by confining failures to individual compartments. In the event of an anti-ship missile strike, the missile penetrates the hull and detonates within one of these compartments. An illustration is given in Figure 2.1, the subsequent explosion releases a cloud of high-speed fragments, followed by an intense pressure wave [19]. Together, these loading conditions challenge the armour performance. The fragments impose severe localised perforation threats, blast loads subject the weakened bulkhead to widespread dynamic pressures. The primary objective of armour plating is thus twofold. Protect vital equipment and contain inflicted damage within a single compartment [20, 21].

The ballistic conditions related to the detonation of a missile can be separated into high-speed fragment impact ranging $500 - 2000$ m/s [22], and the shock wave impact load of the concurrent blast [12]. Upon fragment impact the armour material and the projectile deform at the surface without full penetration. Depending on the angle of attack, the initial velocity, and the geometry, the fragment may experience plastic deformation and shatter, perforation or ricochet [12, 23, 24].

Figure 2.2 illustrates the stress state during high-velocity fragment perforation, and it clearly shows a sharp local pressure gradient at the interface between the projectile and the armour material. As the fragment begins to penetrate further, the armour material must accommodate rapid, localised flow under extreme high strain-rate conditions $10^5 s^{-1}$ to $10^7 s^{-1}$ [25], elevated temperatures [25, 26], and extreme local pressures. Experiments by Recht (1964) [27] indicate a local shear zone temperature of 650 $^\circ C$ in titanium, and Dao and Shockey (1979) [26] predict a local temperature of 500 $^\circ C$ in steel.

In the scenario where the fragment is arrested, the sudden drop in strain-rate leaves the rear side

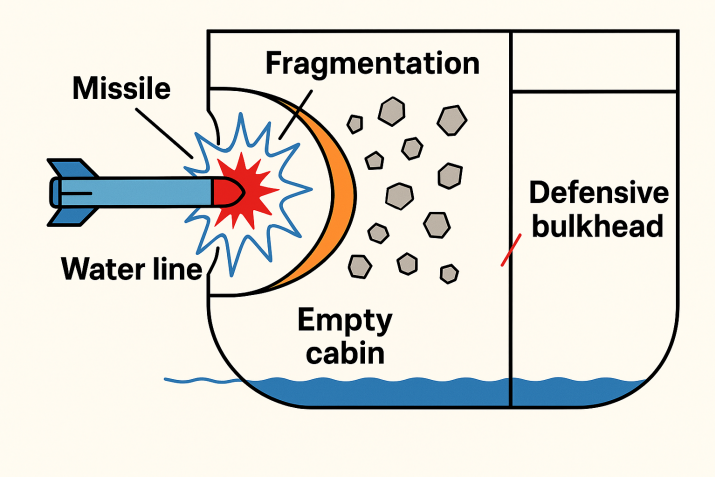


Figure 2.1: Sketch of missile strike, adapted from [19].

of the armour to the concentrated force of the impact, potentially stretching and triggering different modes of material failure, locally confined in adiabatic shear bands (ASB) and crack initiation. In case of perforation these localised failure mechanisms grow into cracks and lead to material failure. The fragment perforates the material and leaves a hole surrounded by highly deformed material. In either scenario the weakened material is vulnerable to subsequent blast wave loading. Research on the combined effects is limited, therefore this review adopts a separate but interrelated approach to these complex conditions [12, 28].

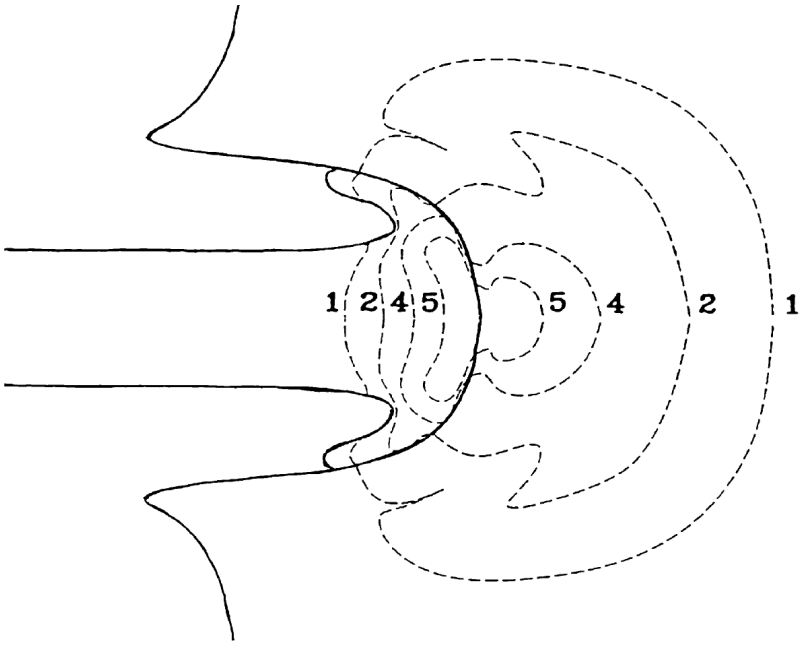


Figure 2.2: Simulation of pressure distribution from 1-5 GPa in a depleted uranium alloy penetrator at 1650 m/s [10, 29].

Both fragment impact and blast loading impose large strains and occur at high strain-rates, yet they provoke distinct material responses. Table 2.1 shows that from some steel the strain-rate can span several orders of magnitude. For instance, during fragment impact, strain-rate typically ranges from $10^5 s^{-1}$ to $10^7 s^{-1}$, while under blast loading the rate falls within the $10^2 s^{-1}$ to $10^4 s^{-1}$ interval. The specific stress state and material behaviour is related to geometric factors as well. Generally thin plates experience plane strain at lower strain-rate conditions.

Rapid release of energy during these deformations is capable of locally increasing the temperature to between 40% and 100% of the melting temperature of the material [30, 31]. At strain-rate exceeding $10^2 s^{-1}$ the material response becomes increasingly adiabatic, which results in elevated local temperature, strain localisation, and reduction of the flow stress. Moreover, as the strain-rate exceeds $10^5 s^{-1}$, for thinner sheets the stress state evolves from plane stress to a more plane strain state, which changes material behaviour from ductile to more brittle failure [12, 32].

Table 2.1: Characteristics of different strain-rate, mechanical and material responses, and stress states. Adapted from [12].

strain-rate (s^{-1})	10^{-8} to 10^{-6}	10^{-4} to 10^{-2}	10^0	10^2 to 10^4	10^5 to 10^6
Type of test	Creep	Quasistatic	Intermediate strain-rate	Bar impact	High-velocity plate impact
Type of physical response			Mechanical resonance in machines and specimen	Elastic-plastic wave propagation	Shock wave propagation
Type of material response	Isothermal		Adiabatic		
Importance of inertial forces	Inertia forces neglected		Inertia forces important		
Stress state	Plane stress				Plane strain
Level of stress	Increasing stress levels				

The diverse loading conditions demand an optimal balance between impact toughness and hardness. In general, high impact toughness is essential for blast load resistance, because it enables the material to absorb energy without catastrophic failure. In contrast, high hardness is critical to resist perforation. This inherent trade-off requires careful material selection and design. Standards such as the Australian Defence 8030 specification given in Table 2.2, set precise hardness and impact toughness thresholds. These design criteria are essential to ensure that the correct armour steel is selected for the specific application [13]. In general, material responses under ballistic conditions are complex and strongly influenced by strain-rate, deformation mode, and temperature. Chapters 2.2, 2.3 and 2.4 further elaborate on failure micro-mechanisms under these severe loading conditions and elaborate on strategies to optimise both resistance to perforation and blast-induced failures.

2.1.2. Ballistic testing methods

Evaluating the dynamic response of armour steels requires specialised experimental techniques. This section provides a short list of common test methods. This thesis makes use of the Fragment Simulating Projectile (FSP) and the Drop-weight impact test. These methods will be further described in Section 2.2 and 2.4 respectively.

- **Fragment Simulating projectile (FSP) Tests**
  FSP tests are standardised under guidelines such as STANAG 2920 [33] and replicate the realistic impact of fragments using controlled projectile mass, geometry and velocity. These tests serve as a reliable method to assess perforation threshold values [34].
- **Split-Hopkinson Pressure Bar (SHPB)**
  The SHPB technique enables an accurate measurement of high strain-rate behaviour. It is used to create controlled stress states, in compression, tension, or shear, and is often coupled with high-speed digital image correlation (DIC) to capture complex deformation fields [30].
- **Drop-weight impact tests**
  This method uses a weight, height, and mass to apply a specific load. Impact pressure is deter-

Table 2.2: Armour steel classes defined by DEF(AUST) 8030 with specified hardness and impact toughness limits [13].

ARMOX 440T	Hardness (HB)	Min. Charpy Toughness (J)	Intended Application
C1	n/a	n/a	Use of structural QT steel in protective structures
C2	260–310	40	Protection against blast and fragment loading with structural capacity
C3	340–390	20	Ballistic protection with structural capacity
C4	370–430	18	Higher ballistic protection than C3 with similar structural capacity
C5	420–470	16	Higher ballistic protection than C4, tougher than C6
C6	477–534	16	Applique armour class, can be used in structural applications
C7	570+	12	Non-structural class, higher ballistic protection than C6
C8	570+	8.1	Non-structural class, higher ballistic protection than C7 with a lower toughness

mined by the sample weight and geometry. These tests are used to simulate moderate dynamic load, similar to automotive crash conditions, and provide insight into how strain-rate affect the ductility and energy absorption capabilities of the steel [32].

- **Hole Expansion test**
  Specifically applied to assess local deformation capacities surrounding the perforation sites, these tests produce information on the residual ductility and resistance to further damage after an initial impact [32].

Having defined the experimental landscape, the examination of fragment characteristics and impact conditions which dictate penetration modes and the onset of localised shear in armour steels is to be investigated.

2.2. Fragment impact

This section investigates fragment formation, perforation, material behaviour under high strain-rate conditions, and failure. When an explosive charge of a kinetic energy missile detonates inside the ship, the explosion leads to a nearly instantaneous pressurisation and fragmentation of a missile casing. As the casing fractures, highly pressurised gases escape, generating a shock wave that propels fragments of varying shapes and sizes at extremely high velocities. Study by Xiangshao Kong et al. (2013) [22] presents both numerical simulations and physical experiments on the explosive fragmentation of a A235 mild steel casings. Their simulation shows how large steel strips form and shatter into fine and larger fragments, the far end caps form relatively large fragments. Due to the position of the TNT charge in the cask, typically located near one end of the casing, the fragments generated at the opposite end experience enhanced acceleration from the initially reflected pressure waves. Their study reports that fragment velocity on the cylindrical sides of the casing and those near the charge reach approximately 1210 m/s. Fragments from the far end of the cask reach velocities of approximately 1613 m/s [22]. Research by Hiroe et al. (2008) [35] confirms that a wide range of fragment shapes and sizes is produced during the explosion. Figure 2.3 shows the fragments formed by an explosion in a SS304 thin walled steel cask. Most fragments display a near 1:1 aspect ratio, although some fragments originating from the circumferential walls exhibit an aspect ratio's up to 1:5, these originate from the initial long strips that scatter into smaller fragments.



Figure 2.3: Collection of fragments from physical test by Hiroe et al. [35].

2.2.1. Fragment simulating projectiles

To ensure reproducible testing conditions in ballistic research. A variety of fragment simulating projectiles (FSPs) have been introduced. These projectiles are specifically designed to replicate the size, mass, shape, and kinetic behaviour of real fragments. FSPs provide a standardised method for evaluating the performance of protective systems in different laboratories and test scenarios. Within NATO, FSP specifications are compliant with the test Standardization Agreement 2920 (STANAG 2920) and associated Allied Engineering Publication (AEP 2920) and MIL-DTL-46593B, which establish the criteria for fragment geometry, mass tolerances, and hardness requirements. Figure 2.4 provides the technical drawing of a 20 mm FSP as stated in the MIL-DTL-46593B standard. These standards are determined for an FSP diameter ranging from $2.54 - 20$ mm. Figure 2.5 shows several 20mm FSPs that have been impacted Armox 440T at different velocities. The standard FSP is made of cold rolled and annealed 4337H or 4340H medium strength steel, with a Vickers hardness of $277 - 292\ HV$, which is close to typical munition and shell material and therefore undergoes similar plastic deformation and impact behaviour. These projectiles can be fired at velocities up to 2000 m/s [36–38].

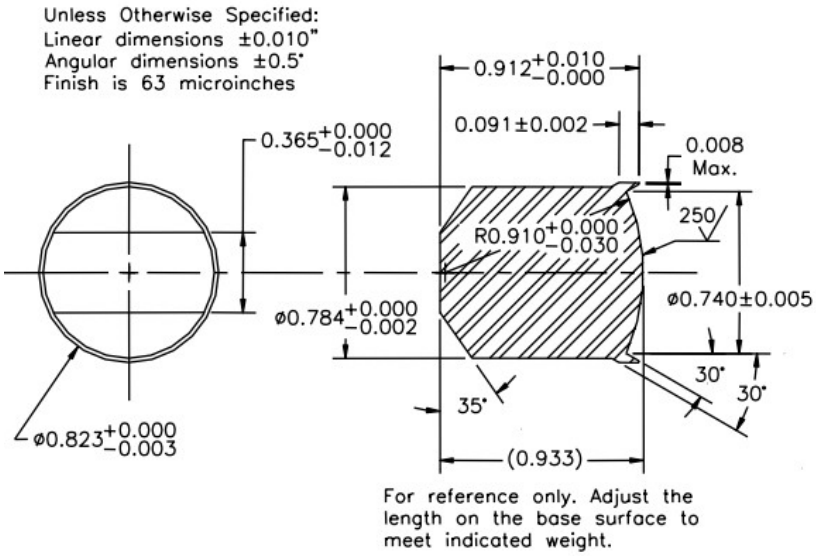


Figure 2.4: Technical drawing of the MIL-DTL-46593B standard 20 mm FSP (dimensions in inches) [39].



Figure 2.5: Post-impact 20 mm FSPs from tests on Armox 440T, a) steel FSP shot at 373 m/s, b) copper FSP shot at 328 m/s, c) steel FSP shot at 1016 m/s [36].

2.2.2. Ballistic limit

When high-velocity fragments impact armoured materials, several scenarios can occur. Depending on factors such as kinetic energy and impact angle, a fragment can ricochet, shatter, partially, or fully penetrate the target plate. The critical velocity at which a fragment of a specific mass penetrates the armour successfully is known as the ballistic limit. For ballistic testing, the V_{50} ballistic limit is commonly applied, this value represents the impact velocity that yields a 50% probability of perforation. Upon perforation the residual velocity of the fragment is an important parameter in determining the remaining threat. Recht and Ipson (1960) [40] developed an analytical relation to estimate the theoretical ballistic limit given by Equation 2.1 using the residual projectile velocity V_R, the impact velocity V_I, ballistic limit V_{BL}, mass of the debris or plug m, and M_P the projectile mass. The ballistic limit can be determined following the rewritten version of Equation 2.2. However this relation does not take target geometry into account. Work by Iannucci et al. (2015) [36] shows that the ballistic limit of a steel 20 mm FSP on Armox 370T and Armox 440T is close to 290 m/s and 330 m/s respectively.

$$V_R = \frac{1}{1 + \frac{m}{M_P}} \sqrt{V_I^2 - V_{BL}^2} \tag{2.1}$$

$$V_{BL} = \sqrt{V_I^2 - V_R^2 (1 + \frac{m}{M_P})^2} \tag{2.2}$$

Perforation criteria may differ across applications: in army settings, the limit is often defined by the formation of a cracked bulge through which light passes, whereas in naval applications, especially for larger projectiles, the limit is reached only upon complete penetration. In the context of protection tests, the ballistic limit is determined when a witness plate positioned behind the armour is perforated [41].

The ballistic limit is influenced by projectile parameters, including mass, nose shape, and angle of attack. The angle of attack is often characterised in terms of obliquity, which is defined as the angle between the projectile's trajectory and the normal plane, perpendicular to the plate surface. A 0° obliquity corresponds to a direct, perpendicular impact. Increasing obliquity results in a more angled impact, up to 90° for which the trajectory is parallel to the plate. The relation between nose shape and obliquity significantly affects the penetration, deformation, and failure modes under impact [34].

The paper by Iqbal et al. (2012) [34] reports an extensive investigation on 12 mm thick Weldox 460E steel plates, with a yield strength of 490 MPa, to elucidate the effect of these parameters on both the critical ricochet angle and the ballistic limit velocity. They found that for a fixed impact angle, an increase in the projectile nose angle leads to a reduction of the ballistic limit. The ballistic limit is highest at an incidence angle of 60°, while normal impact at 0° generally demonstrates the lowest ballistic limit. From these results it follows that normal impact from a flat surface projectile shows the lowest ballistic limit [34, 42].

2.2.3. Perforation by plugging

High-speed impact events in solid materials are governed by two interrelated phenomena: the strain-rate-dependent material behaviour and the propagation of shock waves. Both aspects require careful investigation through experiments and numerical simulations [28]. Experimental studies have shown that when a high-velocity fragment strikes an armour plate, the interaction generates stress waves that

quickly propagate through the material at speeds approaching the steel sound velocity which is roughly between $5000 - 6000$ m/s [43]. Because this velocity far exceeds that of most projectiles, the induced stress waves reflect multiple times within the target before the penetrator produces significant localised damage. These reflections not only contribute to the complex stress state ahead of the penetrator, as shown in Figure 2.2, but also induce plastic deformation. The interaction and reflection of stress waves is illustrated in Figure 2.6a. Figure 2.6b illustrates the deformation of the penetrator and where different failure modes initiate in the plate material [23, 34]. Initially, a high-speed elastic wave, known as the ”elastic precursor,” travels at the longitudinal wave speed and stresses the material up to the elastic limit. Figure 2.7 shows that the first wave is typically observed as a rapid increase in the velocity signal. Following the elastic wave front, a plastic pressure wave propagates through the material, deforming the material as it pushes the stress state into the plastic region. As the elastic wave reflects off the rear surface of the target, it interacts with the advancing plastic wave to create additional velocity steps. These features are more pronounced at lower impact velocities. These complex stress wave interactions influence the failure mode initiated in the target, where factors such as plate thickness, hardness, and projectile geometry play decisive roles. The thickness of the plate and projectile, for example, determines the position of the spallation fracture plane [28, 44, 45].

Since plugging localises shear into narrow zones, the next section focuses on adiabatic shear bands, microstructural features that concentrate strain, temperature, and damage and preferential sites for crack initiation.

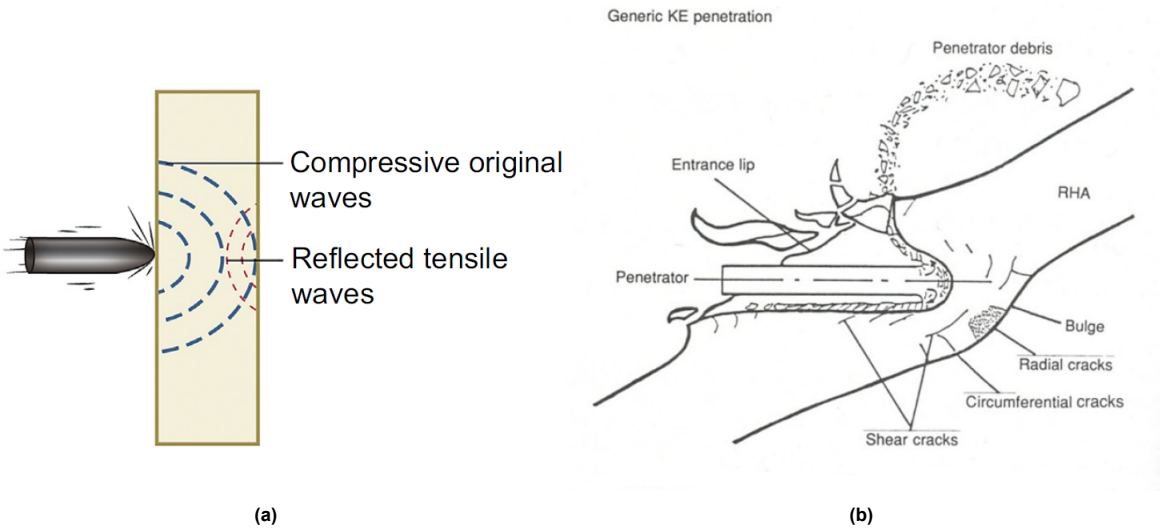


Figure 2.6: (a) Schematic of stress wave generation, (b) Generic penetration process indicating different failure modes [12, 23, 24].

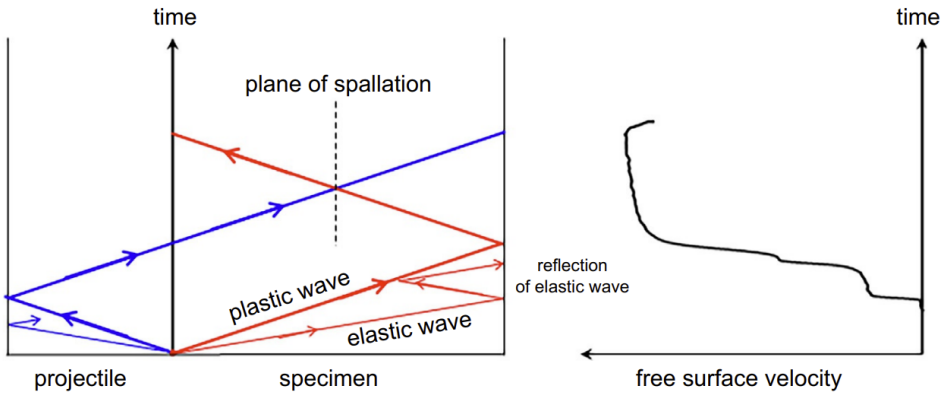


Figure 2.7: Stress wave diagram on same material impact [28, 45].

Plugging failure

Plugging is a failure mode typically associated with blunt projectile impacts on monolithic armour of moderate thickness and high hardness [1]. When a blunt projectile impacts the target, the material at the front accelerates, while the remaining plate material remains relatively stationary. This induces a narrow zone of intense shear under largely adiabatic conditions. The shear strain, strain-rate, and temperature are locally very high, often leading to localised transverse shear failure as illustrated in Figure 2.8 and 2.8b. Certain steel grades are more susceptible to plugging due to the phenomenon of adiabatic shear failure, a localised deformation mode characterised by the formation of a narrow shear band with significantly reduced resistance. Two general concepts are common with respect to this phase transformation. One hypothesis describes post-deformation recrystallisation as result of the elevated temperature. The other concept of dynamic recrystallisation states that transformation is induced by the combined effort of temperature and deformation energy [25, 46, 47]. However, the exact processes remain the subject of ongoing investigation.

Plugging and spalling are characterised by a cylindrical shear stress distribution that results in the extrusion of a relatively intact plug from the target. Because little plastic deformation occurs compared to ductile hole growth, plugging absorbs significantly less kinetic energy. However, the ejected plug itself may serve as a dangerous secondary projectile. The susceptibility to plugging is particularly pronounced when the diameter of the projectile is nearly equal to the target thickness, this 1:1 ratio promotes shear failure in thin steel plates. For the case of Armox440T, Figure 2.9 shows post-impact panels of Armox 440T perforated by 20 mm FSPs, these holes show a clear indication of plugging [36]. Consequently, armour designers have developed countermeasures, such as laminated targets, such as adhesively bonded layers or steel-composite laminates, to suppress plugging by disrupting through-thickness shear [42].

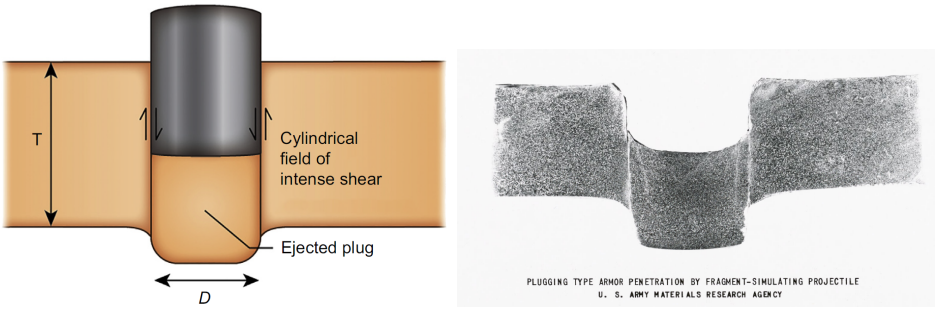


Figure 2.8: Schematic illustration of (a) plugging, and (b) photograph of plugging failure by FSP along adiabatic shear bands [10, 12, 33].

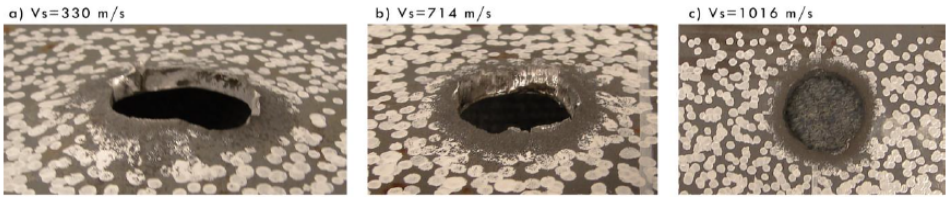


Figure 2.9: Photographs of post impact panels impacted at various velocities of Armox 440T with 20 mm FSP [36].

Failure by plugging poses the highest risk to the structure due to the low energy absorption of the material, and it is shown that Armox 440T displays plugging behaviour. Modelling following the structural approach examines the development of stresses and strains that not only drive the formation of the plug, but also determine the overall resistance of the structure. This method relies on the conservation of linear and angular momentum and divides the penetration process into two primary stages. In the first stage, the projectile and the plug travel together at a common velocity and, as the plug moves through the target, the effective contact length is reduced, causing shear forces. These shear forces induce bending in the surrounding target material, consequently expanding the hole radius. In the sec-

ond stage, the focus shifts to the enlargement of a secondary target zone, with perforation occurring once the target strains as a result of stretching and bending moments [6, 48]. Building on this foundation, the three-stage penetration model treats forward motion as that of a variable mass body, with the forces involved as illustrated in Figure 2.10 [49–51].

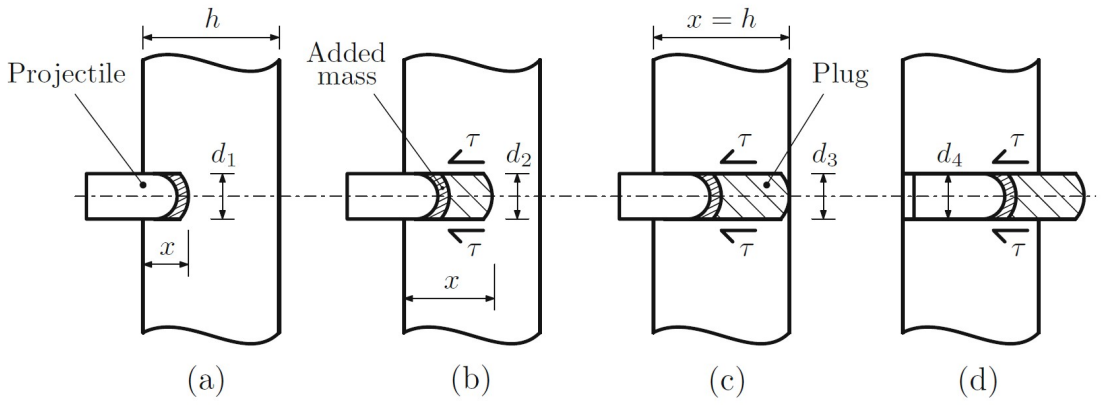


Figure 2.10: Three stage model of plug formation and shear stresses: (a) Stage I, (b) during stage II, (c) end of stage II, (d) Stage III [49].

Together, these studies underscore the multifaceted nature of ballistic impact on armour materials. The intricate interplay between high strain-rate, shock wave propagation, and resulting failure modes, ranging from efficient ductile hole growth to potentially hazardous plugging and spalling, requires the development of comprehensive experimental and computational models. Such models not only improve our understanding of the dynamic response of materials, but also guide the design of armour systems that can effectively mitigate the diverse threats encountered in modern combat scenarios.

The following chapter further investigates the weakest response of armour steels, namely the formation of adiabatic shear bands, their character, and related properties.

2.3. Adiabatic shear bands

2.3.1. Adiabatic shear band formation

An adiabatic shear band is a localised deformation phenomenon observed in high-strength materials deformed at high strain-rate. It arises as a consequence of a delicate interplay between strain hardening, strain-rate sensitivity, and thermal softening mechanisms. During rapid plastic deformation, the strain-induced generation of heat significantly exceeds the ability to conduct heat away from the deformation band, thus establishing adiabatic conditions. This localised heating promotes thermal softening and further localises deformation and heat generation. The exact mechanisms of shear band formation are complex and not fully understood. Marchand and Duffy (1988) [52] describe that plastic deformation evolves over three stages, as shown in Figure 2.11. Initially, the material deforms homogeneously, after which the deformation localises, inducing a shear gradient and leading to plastic instability and inhomogeneous deformation; as strain further increases, the deformation becomes localised and a shear band forms. The second stage ASBs are typically classified as deformed adiabatic shear bands (dASB), and highly localised third stage ASBs are classified as transformed adiabatic shear bands (tASB).

The two types of ASB are shown in Figure 2.12a. These ASB have formed in Armox 500T under compression and a strain-rate of 3900 s^{-1}. The tASB shows as a narrow white etched band, the dASB is wider, and traces of deformation remains around the tASB, the third micrograph shows that continued strain induces cracks [31, 53]. Figure 2.12b shows the corresponding Inverse Pole Figure (IPF) maps and the grain size distribution inside the tASB.

Figure 2.13a illustrates the ASB formation, evolution, and failure process as proposed by Karantza and Manolakos (2023) [53]. The Adiabatic strain conditions lead to shear strain localisation and formation of dASBs, this deformation increases the internal temperature, softening the material due to the increase

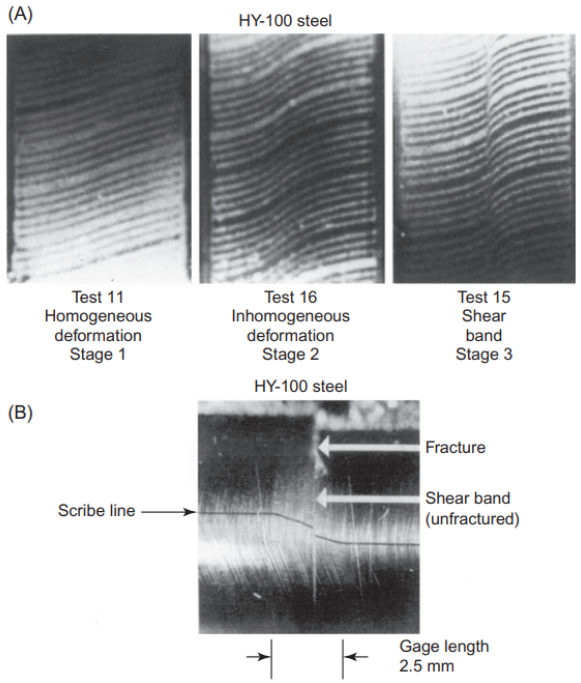


Figure 2.11: Shear band formation (A) Grid patterns shown in the three separate stages at a strain-rate of 1600 s^{-1} (B) A partial fracture shown at a local shear strain of 500% [25][52].

in temperature and reducing flowstress, initiating recrystallisation either through dynamic recrystallisation (DRX), or phase transformation. The newly transformed band experiences further strain and micro-voids form at hot spots, these voids coalescence, and a crack grows until failure. If the deformation does not result in failure, the material cools rapidly, leaving behind a highly deformed shear band. In cases involving phase transformation, the material may quench into a martensitic microstructure. The affected material has different local properties that result in an inhomogeneous microstructure [53, 54]. A more complete description of microstructural behaviour during dynamic recrystallisation is illustrated in Figure 2.13b by Xu et al. (2008) [47]. Initially, the microstructure is filled with a random distribution of dislocations, which move to shear stress driven elongated cell boundaries, further deformation induces grain boundary rotation. This leads to an increased misorientation of $30° - 45°$. The deformation continues leading to subgrain breakup resulting in an ultrafine equiaxed microstructure [47]. A clear example of transformed adiabatic shear band of an interstitial free steel is provided in Figure 2.14. This figure shows fine grains within the deformed base material, the exact grain size is unknown [47].

2.3.2. strain-rate effect

The deformation behaviour of metals is highly sensitive to strain-rate, with variations in strain-rate conditions significantly affecting material properties and triggering distinct failure modes. This inherent complexity necessitates a comprehensive understanding of the underlying mechanisms. In particular, the strain-rate strongly influences the thermal diffusion, strength, flow stress, and stress state conditions, leading to changes in fracture behaviour. Ultimately, the interaction of these strain-rate-dependent properties governs the formation of ASBs and determines key characteristics, including their length and width [25, 55].

Thermal diffusion

The statement that thermal energy is contained and thus ensures adiabatic conditions during deformation is supported by Rittel et al. (2024) [55]. The thermal diffusion distance as a function of strain-rate for copper, steel, and titanium is given in Figure 2.15. The distance converges to zero for strain-rate over $10^4\ s^{-1}$, which ensures adiabatic conditions at ASB formation. At lower strain-rate $10^0 - 10^2$, in the blast loading range, the heat generation is lower, and the heat dissipation rate becomes more significant, which means that full adiabatic behaviour can no longer be assumed [55].

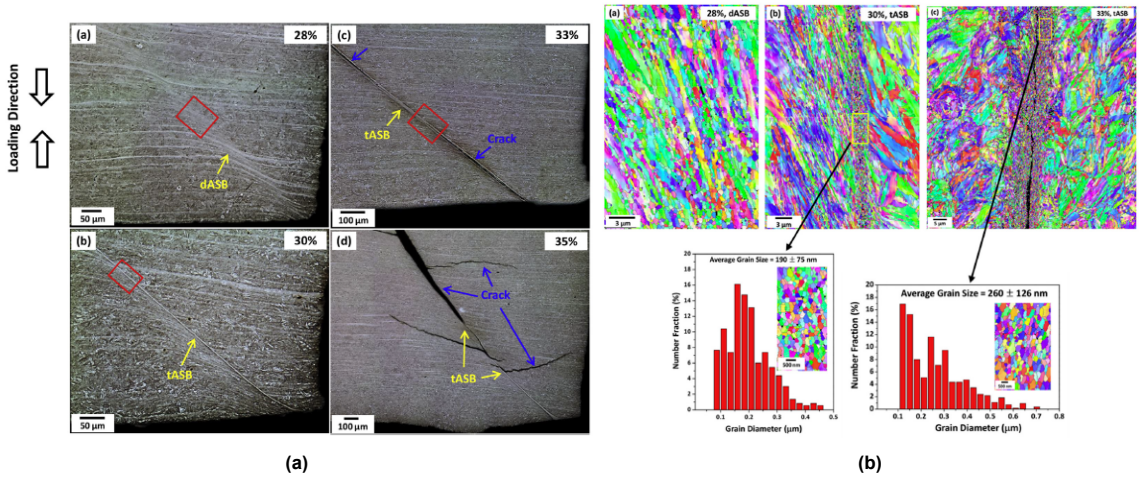


Figure 2.12: Different types of adiabatic shear bands and crack formation under compression in Armox 500T deformed at 3900 s^{-1}: (a) optical micrographs, (b) IPF and grain size distribution in tASB [31, 53].

2.3.3. Shear band temperature

The temperature increase of ASBs can be estimated by assuming that all heat generated from plastic deformation behaves adiabatically. Using the Taylor-Quinney coefficient $\beta = 0.9$, equation 2.3 relates mechanical work from shear $\tau d\gamma$, density ρ, and the specific heat capacity C_p, to the temperature rise ΔT [10, 56].

$$\Delta T = \frac{\beta\ \tau\gamma}{\rho C_p} \tag{2.3}$$

Materials with inherently low strain hardening, density, specific heat coefficient, and high degree of thermal softening are especially prone to localised shearing [10]. Early analyses by Zener and Hollomon in 1944 [57] anticipated these tendencies. Later work by Rogers in 1979 [58] demonstrated that iron and carbon steels with coarser microstructures are less susceptible to form tASB and are more likely to form dASBs, indicating that grain size plays a role. Moreover, as the deformation rate decreases, shear bands typically retain a deformed morphology with transformed regions extending outward until the local temperature falls below a critical transformation threshold [25, 30].

Taylor-Quinney coefficient

The research by Taylor, Quinney and Farren in 1937 [55, 59, 60] concluded that the heat generated by mechanical work is approximately 90%. This has been widely accepted as a constant Taylor-Quinney coefficient $\beta = 0.9$. However, studies by Rittel (2024), and Soares and Hokka (2021)[55, 61] indicate a more complex relation between microstructure, strain and strain-rate and thermal energy from deformation. Figure 2.16 shows the evolution of the Integral Taylor-Quinney coefficient with strain for different materials and strain-rates. The integral Taylor-Quinney coefficient approach relates the total plastic work and temperature change, as given by rewriting equation 2.3, with dW_p the incremental plastic work, to the following equation 2.4 [55].

$$\beta_{int} = \frac{\rho C_p \Delta T}{\int dW_p} \tag{2.4}$$

Cooling rate

Li et al. (2011) [56] state that assuming a ASB as a near zero thickness planar heat source the cooling rate can be estimated using the thin-film solution of the heat-diffusion equation 2.5 with H is thermal energy, density ρ, specific heat C, thermal diffusivity α, the distance from the band x and time t. They report an estimated cooling rate of $10^7\ Ks^{-1}$. At such cooling rate the material is almost instantly quenched, resulting in ultrafine, equiaxed martensite grains. Which also shows from the grain size distribution shown in Figure 2.12b.

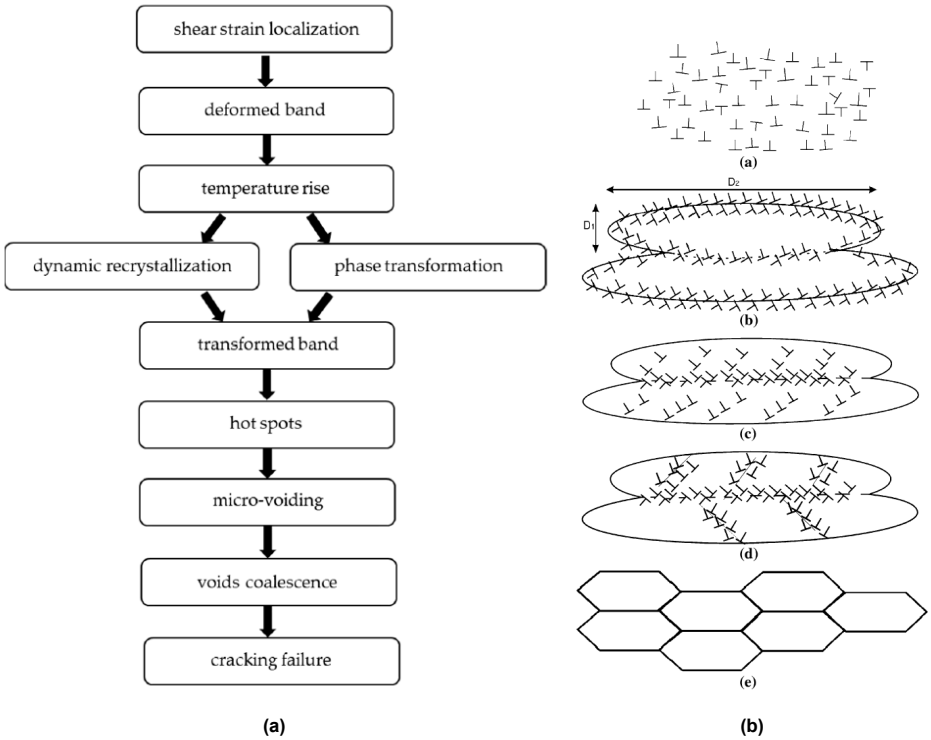


Figure 2.13: Evolution of adiabatic shear band, a) Progression scheme, b) (a-e) Schematic illustration dynamic recrystallisation; (a) dislocation distribution, (b) cell elongation, (c) subgrain dislocation accumulation, (d) subgrain breakup, (e) reorientation and boundary formation [47, 53].

$$\Delta T = (\frac{H}{2\rho C\sqrt{\pi\alpha}})\frac{1}{\sqrt{t}}e^{(\frac{-x^2}{4\alpha t})} \tag{2.5}$$

2.3.4. Flow stress and fracture strain

Collected work from Mc.Donald (2019) [13] presents the effect of strain-rate on the strength and ductility of several armour grade steels. Figure 2.17 shows a positive relation between strain-rate and general flow stress, as well as the corresponding fracture strain indicating a conservation of toughness. However, Armox 500T is an exception, as the fracture strain decreases with increasing strain-rate, indicating that increased strain-rate induces more brittle behaviour.

Critical strain and Shear band width

Xu et al. (1996, 2001) [46, 62] investigated low-carbon steels with different microstructures and found that the critical strain necessary for shear localisation depends strongly on the steel's strength at a given strain-rate. Their study noted that the critical strain values for formation of shear-band were approximately 0.3, 0.36, and 0.83 for quenched, quenched and tempered, and normalised steels, respectively. This indicates that steel with quenched martensite is most susceptible to shear deformation [63].

Xu et al. (2008) [47] report that narrow shear bands often result from higher temperatures and thermal softening, leading to increased hardness, brittleness and introduce higher stress concentrations than wider bands. The higher energy input at increased strain-rate thus further localises deformation. Wider bands form under less severe thermal conditions and distribute deformation more evenly [47]. Moreover, high-strength steels with limited work hardening ability developed pronounced shear bands with widths of 70-100 μm, compared to normalised steels, where the bands were considerably wider (350–400 μm) [44]. For tASB in αTi very fine tASB widths in the range of $6-12\ \mu m$ have been recorded by Dodd and Bai (1989), according to their relation for shear band width, and increase in temperature they found that tASBs form in 5.8 μs [64]. This finding is confirmed by Giovanola (1989) who found that ASB formation takes place in two stages, first strain-rate of $10^4\ s^{-1}$ was measured during localisation, and secondly the strain-rate jumps to $10^6\ s^{-1}$ in the second phase of formation [65]. This finding

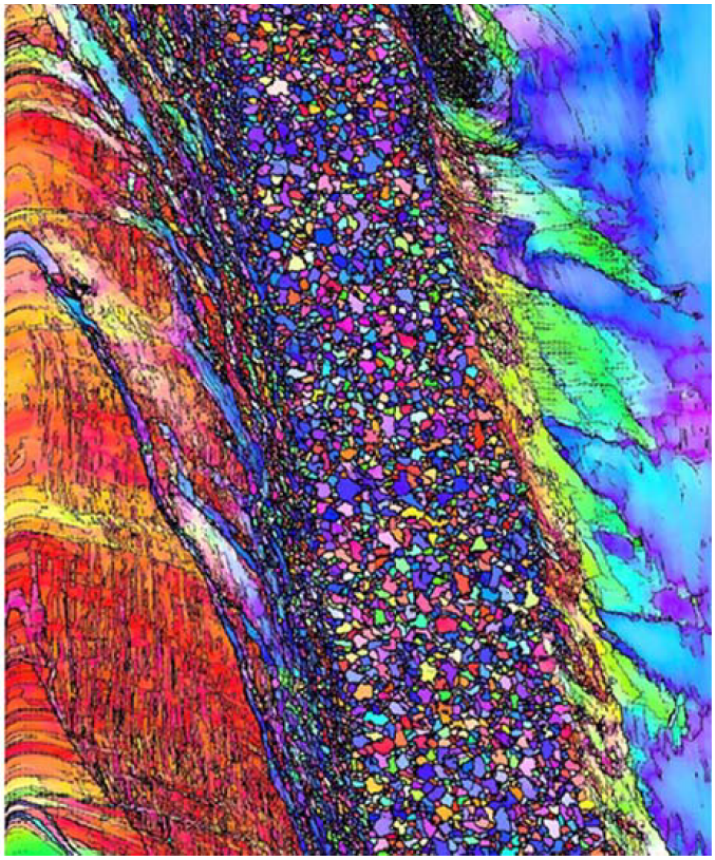


Figure 2.14: Inverse pole figure of transformed adiabatic shear band in an interstitial free steel [47].

indicates a severe reduction of flow stress in combination with thermal softening and other mechanical behaviour leading to superplastic flow. Murr et al. (2002) [66] confirm this and suggest that shear deformation inside an ASB is extremely large due to mechanisms such as DRX and superplastic flow by grain boundary sliding of transformed nanosized grains leading to strains as large as 10 [66].

Shear band spacing

Grady and Kipp (1987) [67] proposed that the rapid drop in flow stress during shear band formation induces unloading in the adjacent material. This unloading effect propagates outward, suppressing the development of nearby potential bands by reducing the local driving stress below the flow threshold. Their illustration of this process is provided in Figure 2.18. They applied a two-temperature model for the shear band and the surrounding material. They identified an optimal shear band width that maximises energy dissipation, accounting for both momentum and thermal diffusion. Based on this, they concluded that fully developed shear bands are spaced at least twice the unloading distance apart. [63, 67].

Full development can be distorted as in composite reinforced materials, the presence of small reinforcing particles promotes the formation of adiabatic shear bands, while larger particles tend to hinder well-developed localisation [30, 47]. This relationships underlines the significant role of thermal effects, deformation history, and microstructure in the evolution of shear band characteristics during dynamic deformation [44].

Shear band velocity

The ASB formation velocity has been measured and analysed by Zhou et al. (1996), Xue et al (2006), and a Mercier and Molinari (1998) [68–70]. They relate impact velocity C, and flow stress σ_f to the ASB formation velocity V, using factor g which is a function of the normalised process zone length $\frac{\lambda}{h}$ and the normalised shear band thickness $\frac{t}{h}$ as given by equation 2.6 [47].

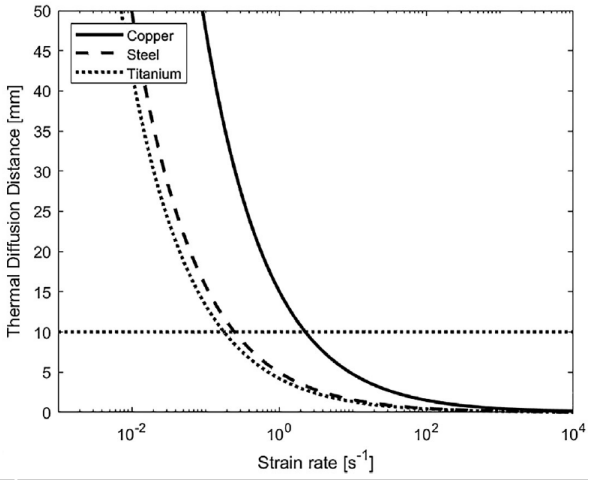


Figure 2.15: Thermal diffusion distance and strain-rate for copper, steel and titanium. The horizontal line indicates a typical sample size [55].

$$V = \frac{\sigma_f}{\rho C} g(\frac{\lambda}{h}\frac{t}{h}) \tag{2.6}$$

2.3.5. Strain hardening

During deformation, materials harden due to dislocation pile-up. Entangled dislocations create local stress barriers, which contribute to strengthening the material. This classical behaviour of strain hardening delocalises further deformation, making this an important material property in ASB formation. Figure 2.19 shows the instantaneous strain hardening parameter n_i at different strain-rate. The clear difference in materials and strain-rates highlights the importance combined mechanical testing and numerical models.

2.3.6. Plasticity models

Several thermomechanical models describe material behaviour under ballistic conditions [13, 71, 72]. The basis for these models incorporates material and empirical parameters including strain-rate, temperature, and hardening effects. Meyer et al (2006) [73] compares the a Thermal Activation Model (TAM) classical Johnson-Cook model over a wide range of strain-rate. They found that TAM better describes flow behaviour of AISI 1045 steel for higher strain-rate. [73]. The TAM model describes the thermal activated flow stress behaviour given by equation 2.7. Most of the model parameters are temperature related, with σ_G and σ_0^* the athermal and temperature dependent flow stress, ΔG_0 the activation energy, $\dot{\epsilon}$ is the strain-rate, $\dot{\epsilon}_0$ the reference strain rate, and n, and m are the hardening and softening effect [73]. The Johnson-Cook model from 1983, equation 2.8 uses more empirically determined parameters. The Johnson-Cook model parameters for Armox 440T are given in Table 2.3 with A, B and n, the initial yield strength, flow stress and strain hardening parameter, C and m, the strain-rate and thermal softening parameter. [74–76].

$$\sigma = \sigma_G + \sigma_0^*[1 - [\frac{kT}{\Delta G_0} ln(\frac{\dot{\epsilon}_0}{\dot{\epsilon}})]^n]^m \tag{2.7}$$

$$\sigma = (A + B \cdot \epsilon^n)(1 + C \cdot ln(\frac{\dot{\epsilon}}{\dot{\epsilon}_0}))[1 - (\frac{T - T_R}{T_s - T_R})] \tag{2.8}$$

2.3.7. Crack initiation and failure

Interrupted tests have shown that the abrupt drop in the stress–strain curve prior to fracture is primarily caused by the initiation and coalescence of microcracks along pre-existing shear bands, rather than

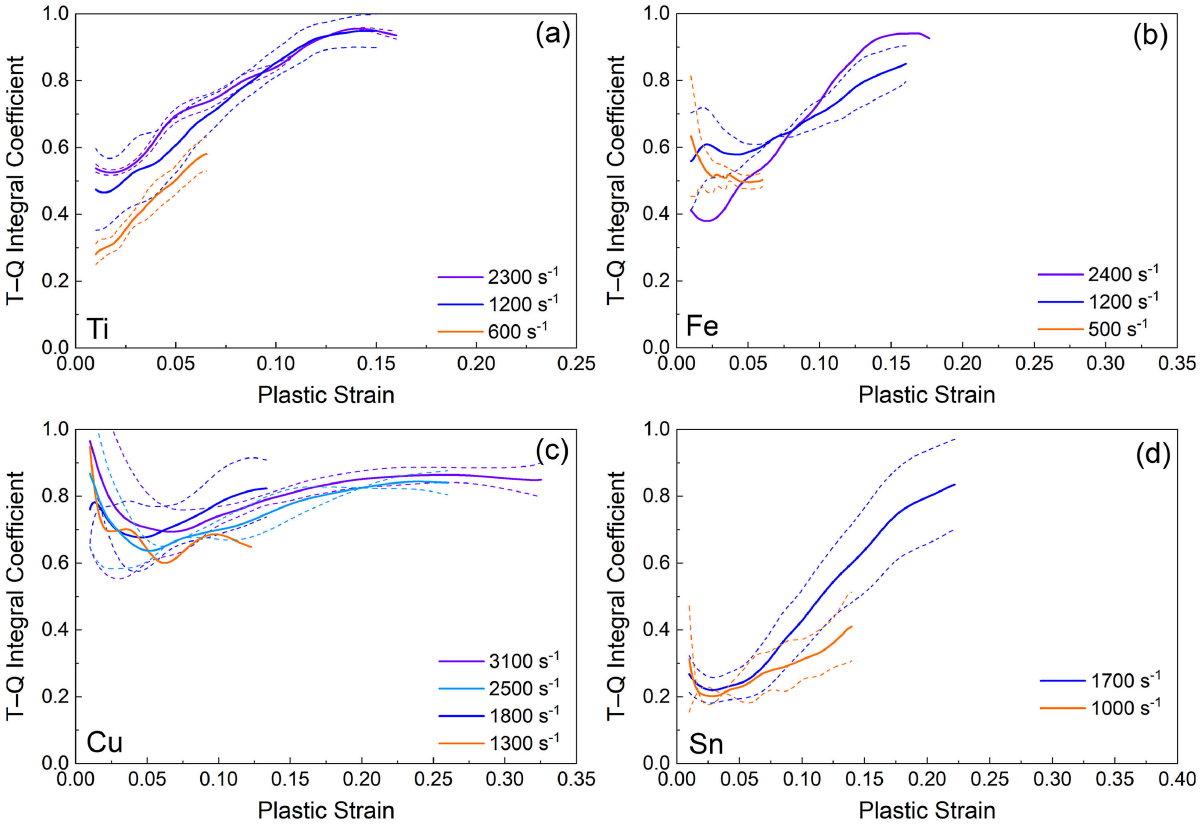


Figure 2.16: Evolution of the Integral Taylor-Quinney coefficient with strain for different materials, strain and strain-rates [61].

Table 2.3: Johnson-Cook material parameters for Armox 440T and a Mild steel [76].

Material	A [MPa]	B [MPa]	C	n	m
Armox 440T	1210	838	0.015	0.283	0.897
Mild Steel	325	275	0.076	0.36	1

by the formation of the bands themselves. Scanning Electron Microscopy (SEM) is commonly used to assess the degree of damage within these bands.

In 1979 Rogers [58] reported that ductile fracture typically occurs during the adiabatic deformation phase, when the shear band is hot and weakened. In contrast, brittle fracture tends to occur after the deformation has stopped, when the hot band is rapidly quenched by the surrounding matrix, resulting in a hard, brittle, transformed structure. Interestingly, detailed observations of fracture surfaces, whether along deformed-type bands in quenched martensite steels or along white shear bands, often reveal a ductile morphology characterised by shear dimples. This suggests that the material in the shear bands, having undergone significant strain at high strain-rate and a corresponding abrupt temperature rise, experiences an annealing or tempering effect. Consequently, the fracture morphology in quenched steels deformed at a high strain-rate can resemble that of annealed or tempered steels. Both the stress state and the increase in temperature within the shear band play a critical role in the eventual failure of the material [58].

Other microstructural factors, such as grain size, pre-existing twins, precipitates, and void content, further affect the evolution of ASB. For example, finer initial grain structures promote dynamic recrystallisation and can enhance the degree of softening within a shear band [54]. In ballistic impacts and high-speed deformation scenarios, loading conditions, including the magnitude of strain-rate, adiabatic temperature rise, and energy input, determine not only whether ASBs nucleate, but also how they evolve toward fracture.

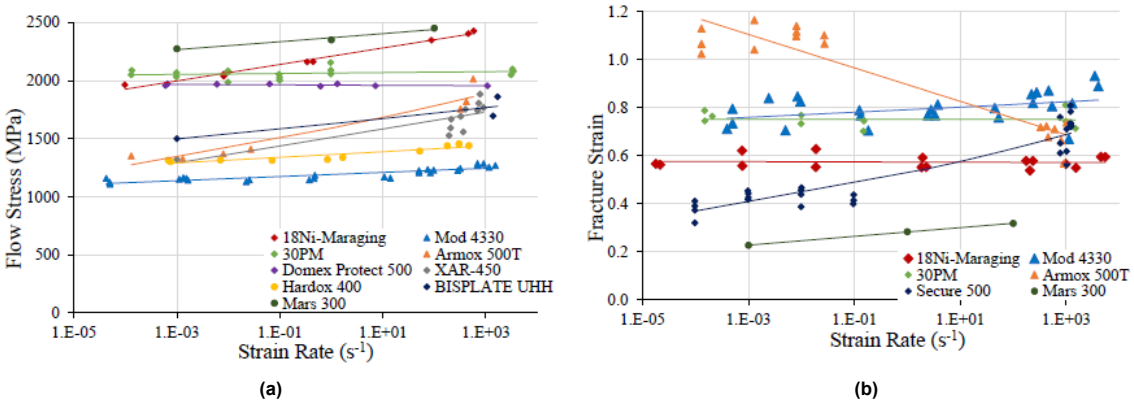


Figure 2.17: The effect of strain-rate of high strength armour grade steels on (a) strength and (b) ductility [13].

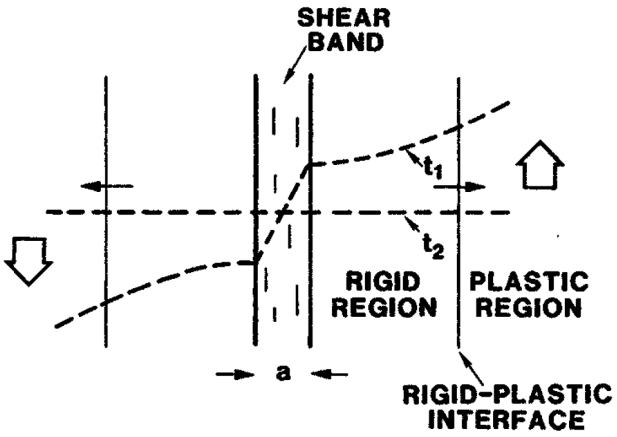


Figure 2.18: Flow stress unloading surrounding material, t1 and t2 represent the material stress lines at different moments in time [67].

Adiabatic shear bands often serve as precursors to both brittle and ductile fracture. As illustrated in Figure 2.20, planar micro-cracks form predominantly within these bands near the plugged region of a steel armour, while only a few appear at the periphery. These bands nucleate at multiple locations, gradually coalesce, and eventually develop well-defined steps that guide subsequent crack propagation [25].

In regions where local heating is most intense, the microstructure evolves rapidly, serving as a precursor to crack initiation and growth. Figure 2.8b from the previous section illustrates the resulting deformation zones and plugging failure, highlighting the crucial role of dynamic recrystallisation and phase transformation processes in the progression from a localised softening band to full fracture.

These band-mediated microcracks act as sharp initiated microcracks under subsequent blast-like loading. We therefore consider how post-perforation stress states elevate local driving forces for crack growth.

2.4. Blast impact loading

During blast impact loading the structural integrity of the armour plate is challenged by the impact of high energy pressure waves. These pressure waves lead to local stress concentrations, particularly around perforation sites and induce further crack initiation and crack propagation. The material response is influenced by dual factors of high strain-rate and geometric effect. Depending on the stand-of-distance the strain-rate ranges between $10^0 - 10^4\ s^{-1}$, and the dynamic transition from ductile void coalescence, to brittle fracture modes defined by the rupture threshold and the minimum size of microcracks neces-

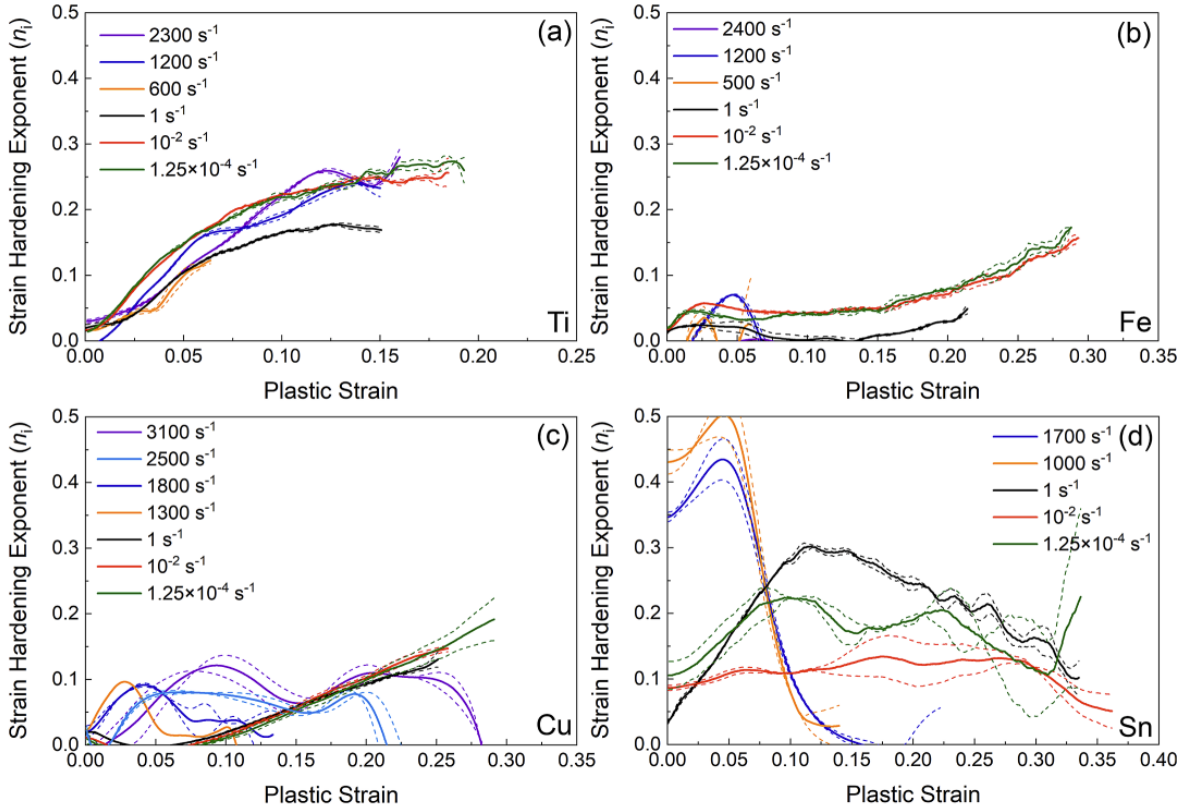


Figure 2.19: Instantaneous strain hardening exponent n for different materials [61].

sary for instability [13].

The blast pressure wave is generated by detonation which generates immense pressure waves. For example TNT, often used as the benchmark explosive, detonates at approximately 6860 m/s and expands by nearly 4000 times its original volume. This rapid expansion produces a near instant change in gas conditions. A blast flow field is predominantly shaped by the initial overpressure and its reflections off adjacent surfaces as the blast wave loses power over distance related to the radius of the blast wave upon impact. In case of a closed ship compartment this effect becomes more complex as the present air is not able to flow away. Therefore an important factor is the stand-off distance between the charge and the armour material. At close range, the behaviour is dictated by direct gas expansion effects, whereas in the far field, a Friedlander based model of static blast pressure as given by the Figure 2.21 applies [12, 77]. Under such dynamic conditions, with strain-rate ranging from $10^0 10^2\ s^{-1}$, the ability of armour plates to resist damage is closely tied to their dynamic fracture toughness, which is itself a function of material strength, ductility, thermal softening, and strain-hardening capacity [78, 79].

Fracture mechanics provides a critical framework for understanding these responses. The geometry of crack tips influences the initiation and growth of fractures, with elastoplastic conditions governed by the fracture toughness, critical facture energy $J_{IC}\ [kJ/m^2]$, and dynamic fracture phenomena addressed through linear elastic parameters, dynamic fracture toughness $K_{Id}\ [MPa/\sqrt{m}]$ and maximum stress intensity factor $K_{Im}\ [MPa/\sqrt{m}]$ [80]. In addition, the fracture path, whether transgranular, intergranular, or mixed, is highly dependent on the effective microstructure, including factors such as grain size, second phases, particles, precipitates, and the texture induced by mechanical mechanical work. This sensitivity extends to multiple fracture mechanisms, such as microvoid coalescence, cleavage in steels, fatigue crack growth, sustained load fracture, or even combinations of fatigue and sustained load regimes.

Experimental investigations reinforce these theoretical insights. Studies, such as those conducted by Kong et al. (2014) [19], examine the combined effects of blast and fragment loading on multilayer ship

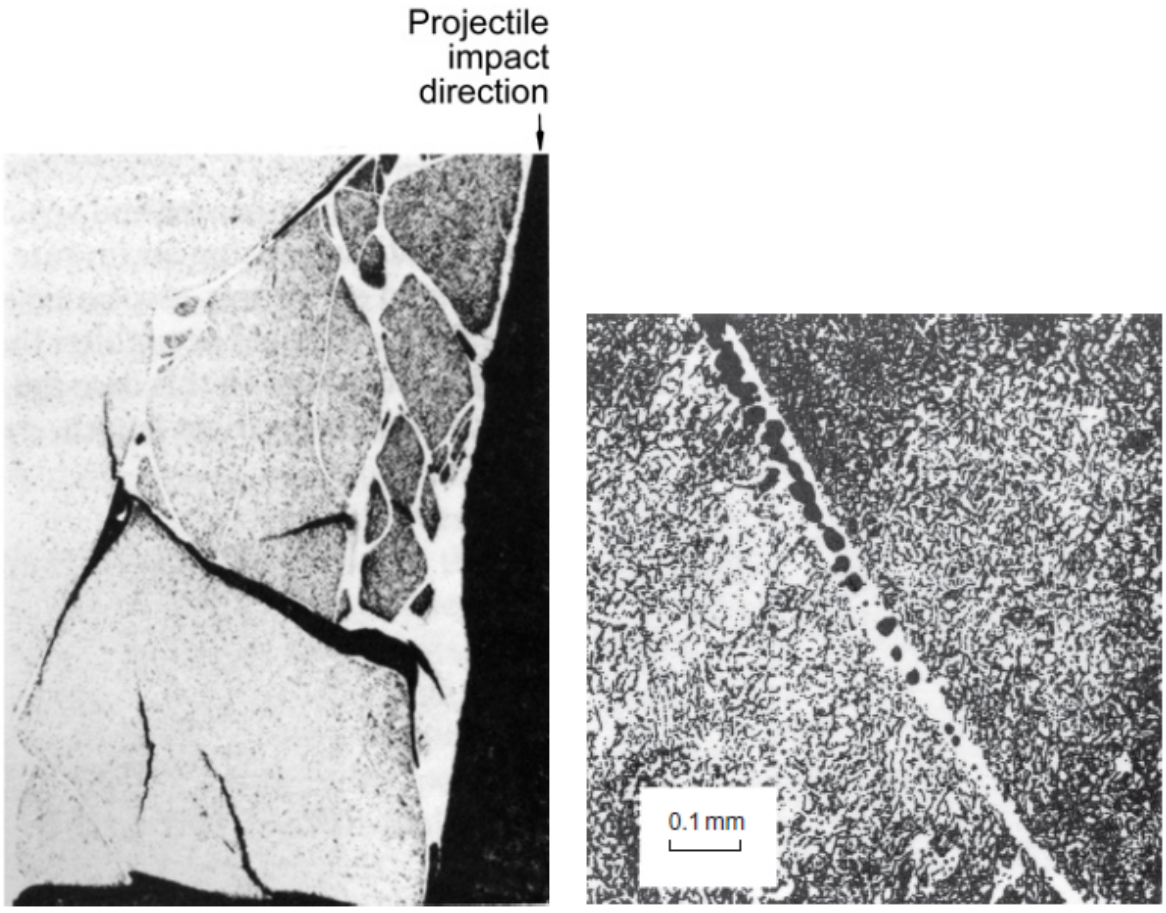


Figure 2.20: (a) Fracture found in plugged region in armour steel, (b) Ductile microvoid coalescence in tASB [25, 44].

structures. Their work demonstrates that fragment perforations not only initiate local stress concentrations but also promote crack initiation and hole coalescence, thereby diminishing the overall blast resistance of the structure. Figure 2.22 shows the results of their simulation of blast inside ship compartments featuring different aspects. The gradient of red to blue indicates high to low pressure zones, but exact values where not reported. The top side of the structure features an absent bulkhead plate, at the left side of the blast one bulkhead already features a hole and the behind the bulkhead below the blast initiation the compartment is filled with water to investigate how failure occurs in such case. Their study is interesting and illustrates the complexity of blast and material interaction well.

2.4.1. Stress state models

In classical fracture mechanics following the elastic stress field approach, the stress intensity K_I around a shot hole changes with relation to the initial hole size R and the crack formation. The blast wave hits loads the plate under complex biaxial loading which loads the plate near the crack tip according to equation 2.9 [80].

$$\begin{aligned} \sigma_x &= \frac{\sigma\sqrt{\pi a}}{\sqrt{2\pi r}} cos\frac{\theta}{2}(1 - sin\frac{\theta}{2}sin\frac{3\theta}{2}) \\ \sigma_y &= \frac{\sigma\sqrt{\pi a}}{\sqrt{2\pi r}} cos\frac{\theta}{2}(1 + sin\frac{\theta}{2}sin\frac{3\theta}{2}) \\ \tau_{xy} &= \frac{\sigma\sqrt{\pi a}}{\sqrt{2\pi r}} sin\frac{\theta}{2}cos\frac{\theta}{2}cos\frac{3\theta}{2} \end{aligned} \tag{2.9}$$

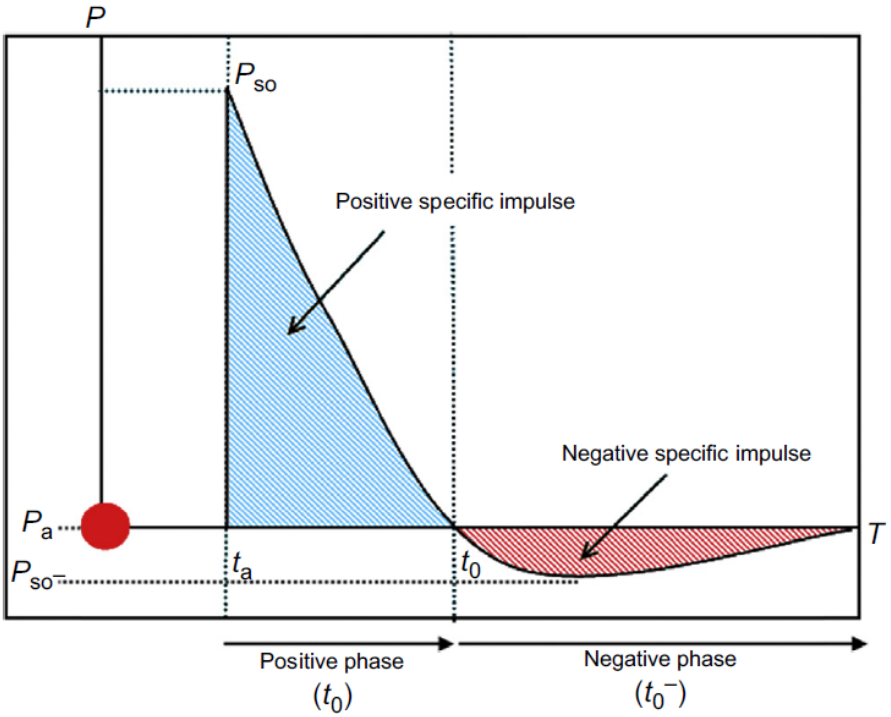


Figure 2.21: Static blast pressure parameters and terminology used for analyses of far-field blast [12].

This relation does describe the stress state around the crack tip, the stress in proximity of the crack tip induced by mode I may be written as a product of a stress intensity factor and a geometrical function which for the case of a loaded infinite plate is equal to $\sigma\sqrt{\pi a}$. Furthermore the plasticity around the crack tip introduces more complexity then this approach. For far field approaches and estimates the stress intensity factor is a valuable failure characteristic.

Equation 2.10 describes the stress intensity factor for centre cracked specimens in standard form where the value for C is changes with relation to different models. Irwin analytically obtained a relation for a row of collinear cracks with interspacing W [81] with 5% accuracy for $a/W \leq 0.25$. Ishida proposed a numerical solution with a geometric factor up to 36 term power series, but Brown found a 4 term approximation for C and Feddersen approximated Isida's term as find in equation 2.10. These relations all fall of for $a/W \geq 0.35$. For the case of a larger central hole such as given in Figure 2.23 equation 2.11, with F variable related to $a/(R+a)$ which is $F = 3.365$ at crack initiation and decreases to either 1 for double crack and $1/\sqrt{2}$ for a single crack growing. However, the complexity of the stress state and geometry requires more accurate models for accurate failure prediction, especially when adiabatic shear bands are involved.

$$K_I = C\,\sigma\sqrt{\pi a}$$

$$\begin{aligned} Irwin &: C = \sqrt{\frac{W}{\pi a} tan(\frac{\pi a}{W})} \\ Brown &: C = 1 + 0.256\frac{a}{W} - 1.152(\frac{a}{W})^2 + 12.200(\frac{a}{W})^3 \\ Federsen &: C = \sqrt{sec(\frac{\pi a}{W})} \end{aligned} \tag{2.10}$$

$$K_I = \sigma\sqrt{\pi a}\,F(\frac{a}{R+a}) \tag{2.11}$$

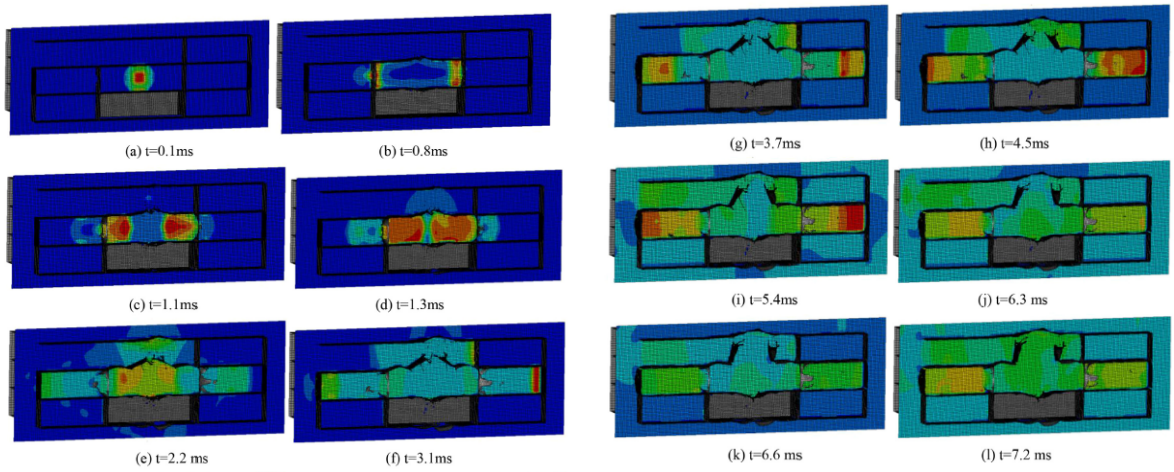


Figure 2.22: Propagation of blast wave and rupture of structure up to 7.2 ms, with red to blue indicating high to low low pressure distribution [19].

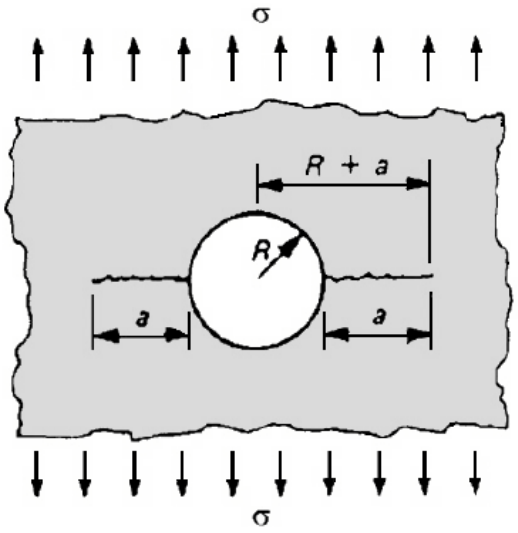


Figure 2.23: Through thickness crack loaded from both sides [80].

2.4.2. Stress concentration

The stress state in the vicinity of a crack tip not only governs the size and shape of the plastic zone but also directly influences the orientation of the maximum shear stress planes. Mohr's circle is widely used in the literature to visualise how the principal stresses determine the shear components in both plane stress and plane strain conditions such as illustrated in Figure 2.25 [80].

A plastic zone forms at the tip of a through-thickness crack and naturally tends to contract in the direction of the plate's thickness along the crack front. When the thickness of the plate is similar to or smaller than the plastic zone's size, this contraction proceeds without restriction, resulting in a predominance of plane stress. Conversely, if the plate is significantly thicker than the plastic zone, the surrounding elastic material hinders this contraction, minimizing strain in the thickness direction and thereby establishing a plane strain condition [80].

This difference in stress state at the crack tip has a pronounced effect on the material's plastic response. Under plane strain, substantial plastic deformation only occurs once the stresses greatly exceed the yield stress. The relation of plastic zone size for plane stress and plane strain is given by equation 2.12. Where σ_{ys} is the yield stess and C is typically estimated at about 1 for plane stress and 1.7 for plane strain. Consequently, the extent of the plastic zone in a plane strain condition is considerably smaller.

Stress concentration factors and plate dimensions influence these deformation states, determining the critical load conditions for crack propagation [80]. Figure 2.24 illustrates the stress state around a hole in case of horizontal tension [82].

$$r_y = \frac{1}{2\pi}(\frac{K}{C\sigma_{ys}})^2 \tag{2.12}$$

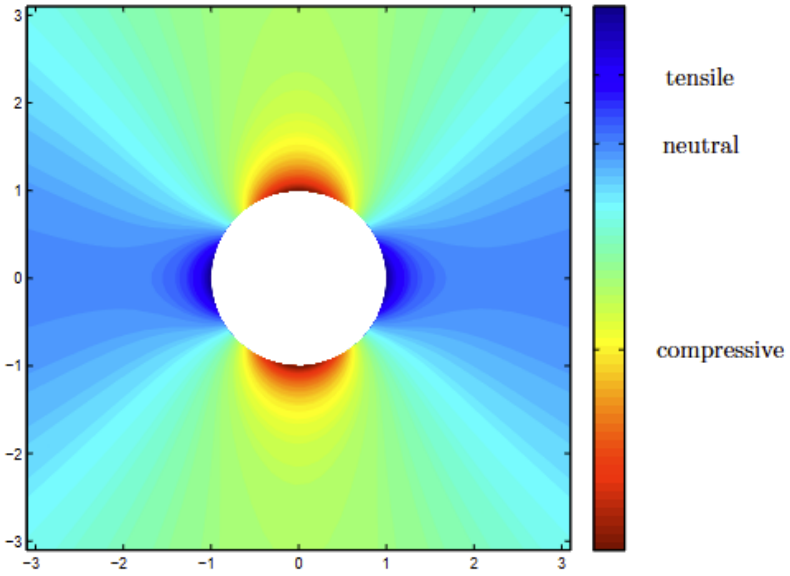


Figure 2.24: Stress concentration on a plate with a circular hole under horizontal tensile loading [82].

Plane stress

For a real crack with a finite tip radius, it is generally observed that at the crack mouth with $\theta = 0$ the stress σ_y exceeds σ_x. As a result, the maximum shear stress, τ_{max}, occurs on planes oriented at 45° relative to the x-axis. This is clearly depicted on the left side of Figure 2.26. The geometry of the plastic zone being relatively small, these orientations provide insight into localised deformation mechanisms in the near-tip region [80].

Plane strain

Under plane strain conditions, the situation becomes more complex due to the presence of a non-zero out-of-plane stress. Near a real crack tip, σ_y remains larger than σ_x. However, as one moves from the surface, where plane stress conditions hold, to the interior region under pure plane strain, the out-of-plane stress σ_z increases from 0 to nearly $\frac{1}{2}(\sigma_y + \sigma_x)$ to ensure volume preservation during plastic deformation. In such cases, since σ_z becomes larger than σ_x, the maximum shear stress reorients so that it acts on planes inclined at 45° relative to the z-axis as illustrated on the right in Figure 2.26.

This behaviour results in fracture behaviour as given by Figure 2.27.

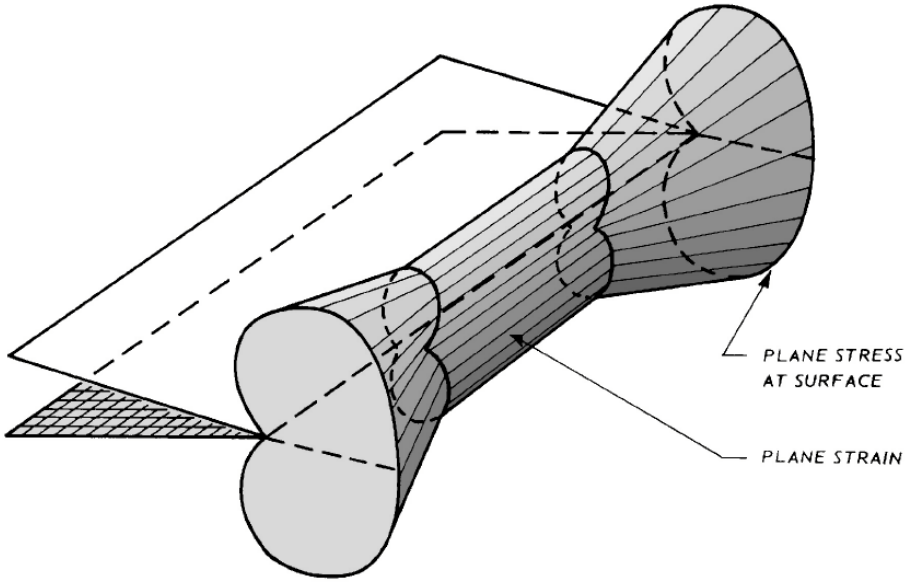


Figure 2.25: Through thickness plastic zone at the crack tip in a plate of intermediate thickness [80].

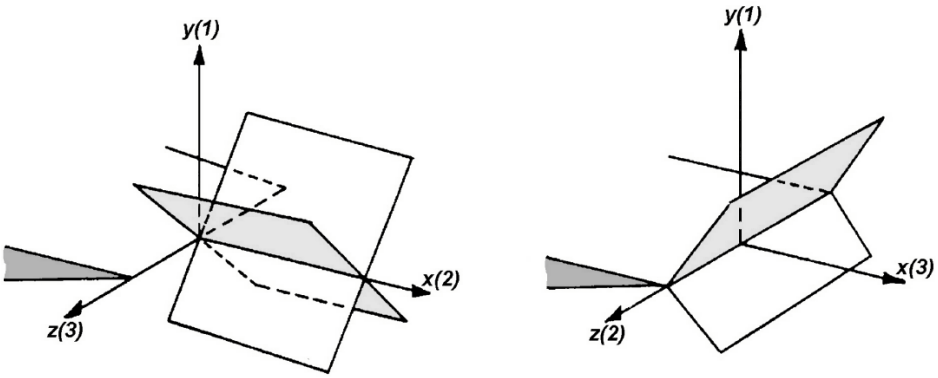


Figure 2.26: Planes of maximum shear stress at the crack tip for (a) plane stress and (b) plane strain [80].

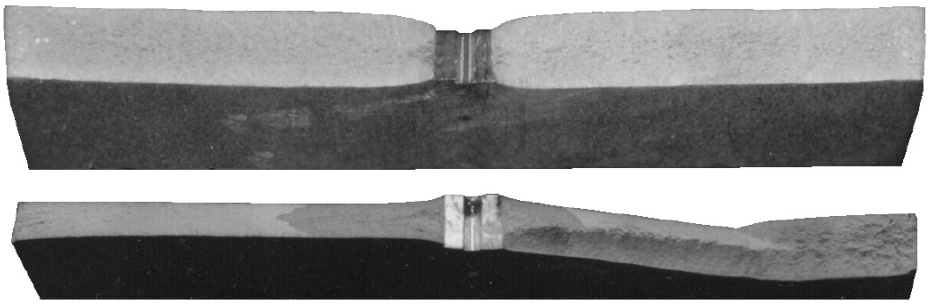


Figure 2.27: Single shear fracture and transition from double to single shear fracture during tensile tests on a centre cracked specimen [80].

3

Material & Methodology

3.1. Armox 440T

This thesis investigates the behaviour of Armox 440T in ballistic conditions related to a missile strike. This material is selected as a promising candidate in ballistic protection due to its high hardness and considerable toughness [15] as provided in Table 3.1 along with the yield strength and quasi-static strain limit expressed in A5-elongation with five times the thickness in length direction and A50-elongation with a 50 mm gauge length.

The chemical composition extracted from XRF measurements and LECO combustion analysis is given in Table **??**. The XRF and LECO results are provided in Appendix B. The LECO combustion analysis method is used to determine the carbon and sulphur content. Armox 440T is a low alloy steel strengthened with 2 wt.% nickel and less then 1 wt.% manganese, chromium and molybdenum. The concentration of trace elements such as sulphur, phosphorus, and copper is minimised. The carbon content is kept around 0.15 wt.% to prevent precipitation and maintain a cubic martensite microstructure [83]. This composition is selected to produce high purity tempered martensite microstructure. The main strengthening mechanism that distinguishes Armox 440T from other steel grades is the absence of impurites, precipitates or second phase particles, which could act as stress concentrator and crack initiators. The base material is shown in Figure 3.1 and clearly shows the lath martensite microstructure, the dark spots in are impurities left by the preparation procedure and not part of the actual microstructure. Armox 440T is a high purity martensite, no inclusions, precipitates or impurities are found.

Table 3.1: Mechanical properties of Armox 440T based on SSAB certificate.

Material	Yield Strength $Rp_{0.2}$ [MPa]	Rm [MPa]	Average Hardness [HV]	Elongation A5 [%]	Elongation A50 [%]	Impact toughness Charpy at -40 $^{\circ}C$ [J]
Armox 440T	$1329 - 1338$	$1419 - 1429$	$471 - 477$	$11 - 12$	$16 - 17$	$30 - 48$

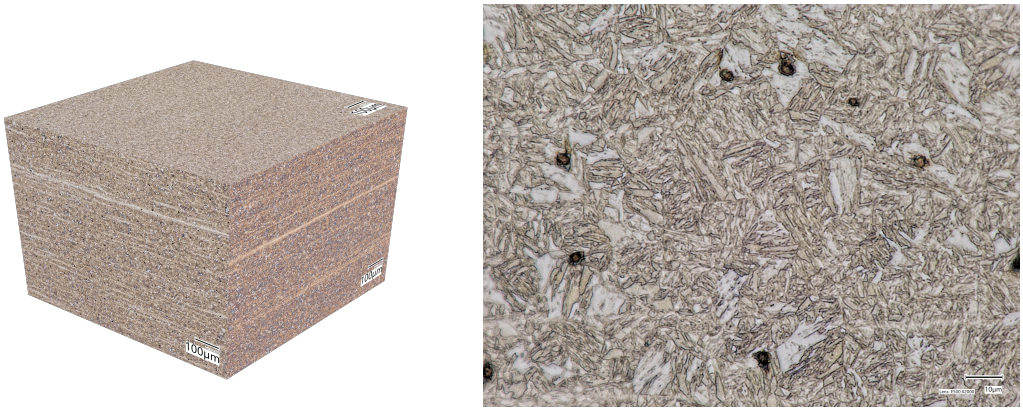
Table 3.2: Chemical composition of Armox 440T.

0ltab:Chemical composition

Composition [wt.%]	C	Ni	Mn	Mo	Cr	Si	Cu	P	S
Armox 440T	0.154	1.95	0.76	0.57	0.53	0.27	0.046	0.013	0.0007
Uncertainty ($\pm$)	0.001	0.05	0.03	0.02	0.02	0.02	0.006	0.003	0.0006

3.2. Ballistic testing methods

This section outlines the experimental procedures used to investigate the ballistic response of test samples under controlled impact conditions. Two separate tests where conducted, first the material test geometry is presented, followed by the method applied for FSP perforation and the Drop Weight



(a) (b)

Figure 3.1: Armox 440T martensite microstructure, (a) 3D presentation at 300X zoom and (b) magnification X2000, the black dots are impurities from the preparation process, no inclusions, precipitates or impurities are found.

Impact (DWI) testing.

3.2.1. Material and test geometry

Two batches of plate material were used to produce multiple samples. The samples are identified by a specific letter and number combination according to their purpose and test conditions.

- **B**: Base material, this material has not been tested and is used as reference as produced material.
- **H**: Samples solely perforated by FSPs, used to investigate the effect of fragment perforation.
- **A**: Samples subjected to both FSP perforation and subsequent DWI testing, used to investigate the effect of blast loading after perforation.
- **900 & 1600**: Indicates the FSP impact velocity in m/s

The DWI tensile test specimen dimensions provided by figure 3.2a have been produced in accordance with NEN-EN-ISO 6892-1:2019 standard. Material batch differences coincide with variations in rolling direction and plate length as illustrated by figure 3.2b. The tensile test samples were extracted after FSP perforation to ensure that the shot hole is in the sample centre.

The base material microstructure of both batches has been investigated and any differences between these batches with respect to microstructural evolution is considered unaffected by these and of no impact to the results [84].

A total of twelve samples were perforated using 20 mm FSPs at impact velocities 900 m/s and 1600 m/s. These velocities were chosen to represent the most abundant fragment velocity and close to the highest velocity fragments found in the study of Kong et al. (2013) [22]. Of these, nine were subsequently evaluated using DWI testing. The DWI test height is experimentally determined due to experience with this procedure. The goal of the test is to load till fracture, and to be on the safe side the first test height was set to 2.1 m. This turned out to exceed the required load strongly and further testing was done at 1 m. The increased hole diameter of samples shot at 1600 m/s require lower loading and therefore the hight was adjusted to 0.6 m for these samples. The test matrix is presented in Table 3.3, the related strain-rates are provided in Table 3.4.

Table 3.3: Sample FSP velocity and drop weight height

Sample ID	FSP Velocity [m/s]	Drop weight height [m]
H1-900	900	-
H2-900	900	-

H3-900	900	-
A1-900	900	1
A2-900	900	1
A3-900	900	1
A4-1600	1600	0.6
A5-1600	1600	0.6
A6-900	900	1
A7-900	900	1
A8-900	900	1
A9-1600	1600	2.1

Table 3.4: Ballistic testing induced strain-rate.

FSP velocity [m/s]	Fragment impact strain-rate [1/s]	Drop weight height [m]	Drop weight impact strain-rate [1/s]
900	$1.2 - 1.4 * 10^5$	0.6	$2.2 * 10^2$
1600	$2.3 - 2.5 * 10^5$	1	$1.7 - 3.2 * 10^2$

Icons or pictograms of loading cases

To enhance clarity in presenting the experimental conditions, icons and colour indication are used for the different loading conditions as shown in Figure 3.3. These schematics are used with the results to distinguish different samples and emphasise the applied loading. The blue and red icons indicate perforation at 900 m/s and 1600 m/s respectively. The FSP shaped icons indicate the perforation velocity and direction. The rectangular plates provide the main stress direction with respect to the DWT test.

3.2.2. FSP Perforation procedure

Ballistic perforation tests were performed at TNO using a static gun mount with a single-round barrel. The FSPs were fired head-on at a fixed target distance. The velocities 900 m/s and 1600 m/s were selected to examine velocity effects on residual structural integrity and subsequent DWI performance.

Three specimens were tested only in the ballistic at 900 m/s to assess material behaviour without DWI loading. These specimens were taken from cut-out material of the original tensile test samples.

The stress state induced by FSP impact is a function of projectile geometry, velocity, and impact angle. These factors, along with the dynamic response of the plate material, govern localised strain-rates and failure modes [50, 85].

3.2.3. Drop Weight Impact Testing

DWI experiments were conducted using the setup shown in Figure 3.4. Samples were positioned horizontally and impacted by a 9100 kg mass from prescribed heights. For Digital Image Correlation (DIC) analysis, one surface of each specimen was prepared with a irregular black-dot pattern, enabling full-field strain measurement. High-speed video capture was performed from the base of the DWI tower.

3.3. Microstructural characterisation

To goal of this thesis is to asses the failure micro-mechanisms related to fragment perforation and drop weight impact loading through microstructural analysis. To achieve a complete understanding of the microstructural evolution during these processes several techniques have been applied. Optical Microscopy (OM), Scanning Electron Microscopy (SEM), Energy Dispersive spectroscopy (EDS) and Electron Backscatter Diffraction (EBSD) have been applied to study the evolution of microstructure, morphology, grain size, local composition and grain orientation. Microhardness measurements are used to determine evolution of the harness profile of fragment perforation and ASB hardness. Most

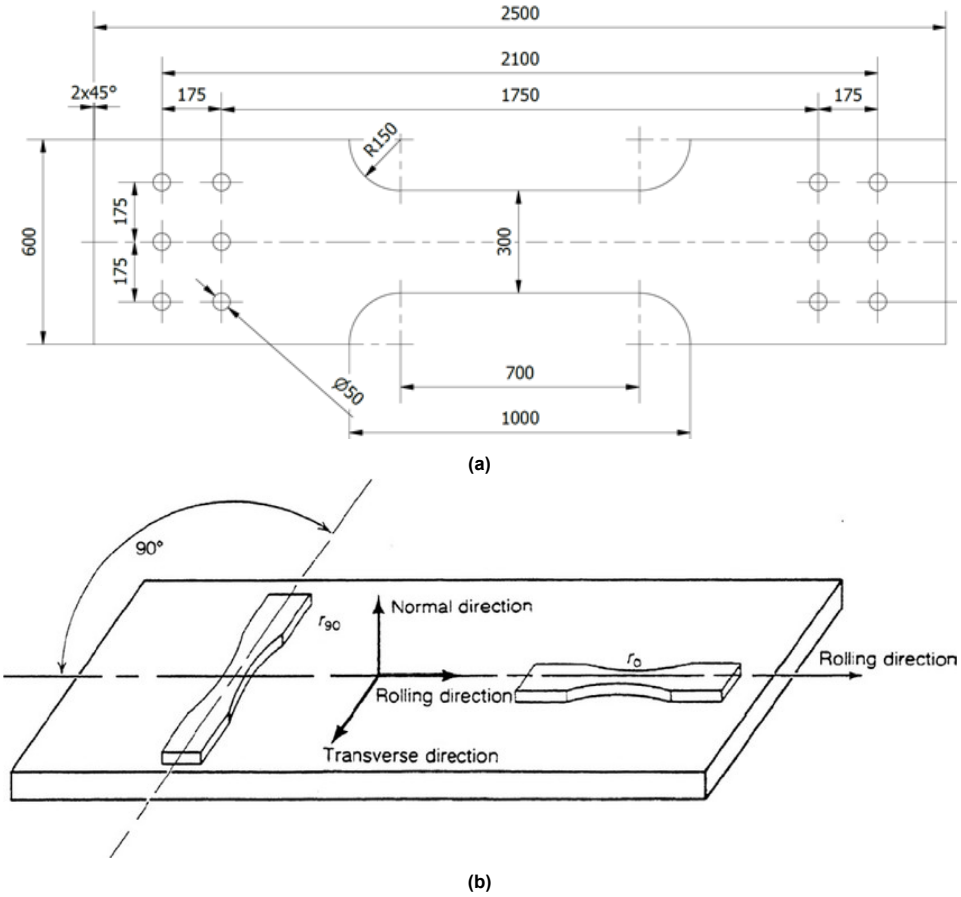


Figure 3.2: Tensile test samples, (a) technical drawing drop weight tower samples, plate thickness is 6.4 mm, (b) Orientation relation with respect to the rolling direction and sample length [84].

samples for microstructural analysis are taken as through thickness cross-sections from the shot hole. The fractured samples from DWI test have been studied using OM and SEM for fractography here also through thickness cross-sections have been investigated for ASB presence and crack growth parallel to the plate.

The initial step in sample preparation is to cut to manageable sizes using a large bandsaw and the Struers Discotom-6, after which the samples where embedded in conductive resin using the Struers CitoPress-5. The Struers Labopol-21 is used for manual grinding with P400, P600, P800, P1200 and P2500 SiC paper. The Struers LaboPol-5, or the Struers Tegramin-30 for manual or automatic polishing with 3 μm and 1 μm. The preparation for EBSD and microhardness requires final polishing with Oxide Polishing Suspension (OPS) as these can not be etched. After grinding, after each polishing step and after the final preparation the samples are cleaned in an isopropanol ultrasonic bath. The other samples are chemically etched in Nital 5% for $40 - 45$ seconds.

Optical microscopy

The Keyence VH7000N Digital Microscope has been used for microstructural characterisation around the shot hole and fractography on the fracture surface. This microscope offers 3D image stitching giving a clear image of fracture surfaces. The OM measurements are used to determine the presence of ASB and their role in failure by drop weight tower loading.

Scanning electron microscopy

The JEOL JSM-IT 100 SEM was used to obtain high magnification imaging of fracture surfaces, Adiabatic Shear Bands and microstructure characterisation around the shot hole using secondary electron imaging at 20.0 kV acceleration voltage in high vacuum. Electron Diffraction Spectroscopy has been used to investigate segregation bands in the base material.

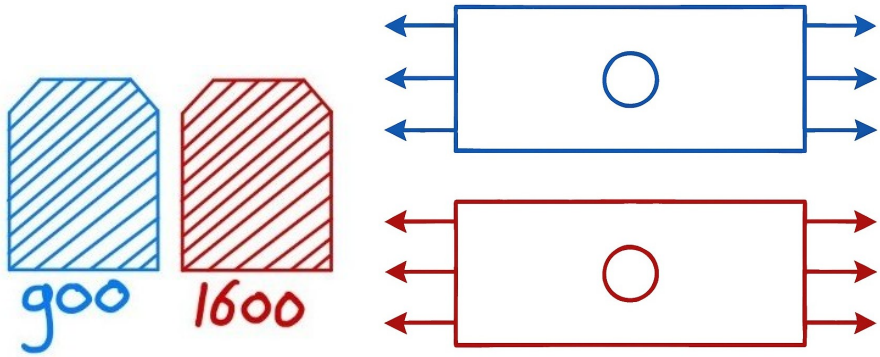


Figure 3.3: Loading condition icons with colour coding related to the the perforation velocity in m/s as indicated.

Vickers Microhardness

The Vickers hardness measurements where done using the Struers EMCOTest DuraScan G5 machine at the TU Delft microscopy lab. Hardness profiles of base material and through thickness cross-sections near the shot hole have measured to assess strain hardening from perforation. These profiles where done using 1 kgf (1 HV) indentation force. Due to the inconsistent shape near the hole the location of hardness measurements have been chosen similarly and aim to achieve a complete hardness profile within a reasonable amount of time. Measurements of ASBs where done using 0.01 HV (0.01 kgf) as with higher force the indenter would also measure outside the ASBs because of their width.

Electron Backscatter Diffraction

The grain size, orientation, and prior austenite grain size have been determined using EBSD data acquired from the FEI Helios G4 CX microscope with a Field Emission Gun with a 6.4 nA and 20.0 kV acceleration voltage. Post-processing of the data was done using EDAX-OIM Analysis 8 software. The base material has been measured on in all three orientations to determine the grain size and investigate orientation relation from the manufacturing process. Three different locations of perforated sample cross-section has been measured, far away from the hole, close to the hole centred around an ASB and at an ASB further from the hole at the entrance side of the plate.

X-ray Diffraction

X-ray Diffraction (XRD) was employed to confirm the presence of martensite within ASBs identified in OM/SEM and to quantify associated phase fractions. Measurements were performed on polished cross-sections using a Bragg–Brentano geometry diffractometer with CuKα radiation (λ = 1.5406 $\mathring{A}$), operating at 40 kV and 40 mA. Scans were collected over a 2θ range of $40°$–$100°$ with a step size of $0.02°$ and a counting time of 2s per step. Martensite identification was based on characteristic α'-Fe bcc peak positions and broadening relative to base material ferrite, following reported differentiation approaches for deformation- or transformation-induced martensite in steels. Full Width at Half Maximum analysis was performed to assess lattice distortion, which showed a strong correlation with the locally elevated hardness values obtained for ASBs, consistent with the high dislocation density and tetragonality of carbon-supersaturated martensite. Retained austenite peaks were not detected above the noise level, indicating a near-complete transformation within the ASB regions. This phase analysis supports the conclusion that localised severe plastic deformation during impact induces austenite-to-martensite transformation, contributing to the high hardness and brittleness measured in the shear bands.

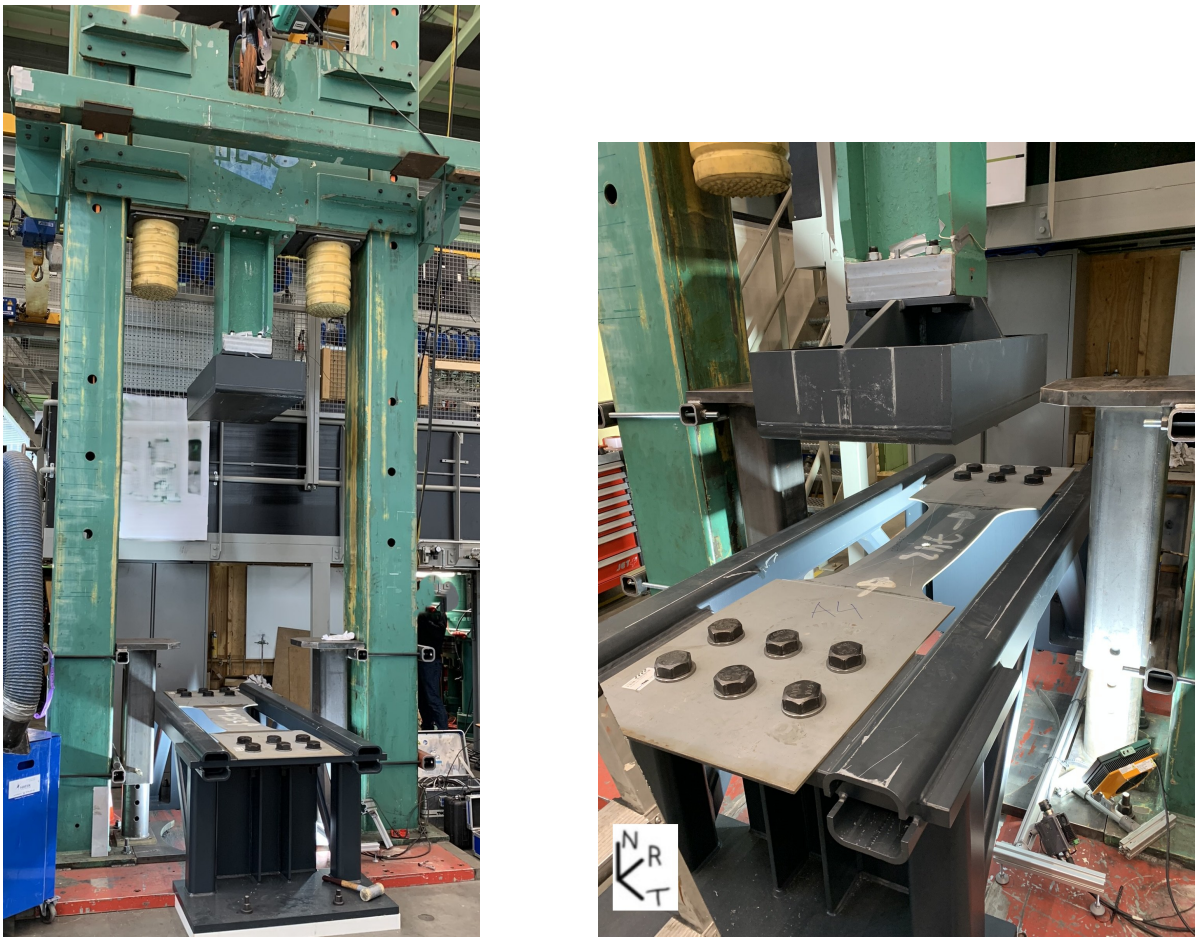


Figure 3.4: Drop weight impact tower setup at TNO Structural Dynamics lab.

4

Results and discussion

This chapter contains results from microstructural analyses and discussion on research questions through visualisation by optical microscopy, hardness profiles, electron backscatter diffraction (EBSD), and scanning electron microscopy (SEM). First, the dominant failure mechanisms during fragment perforation are discussed by comparing microscopy results and hardness profiles of the shot hole cross-sections. The material response to high-velocity fragment impact is discussed from analyses at two different velocities and substantiated by hardness profiles that describe global deformation and strain hardening. The microstructural characteristics shown by microscopy initiate discussion of the microstructural changes, formation, and characteristics of the adiabatic shear bands. The different properties of the adiabatic shear bands are highlighted through local microhardness measurements and microstructural analyses. A more in-depth description of the adiabatic shear band microstructure is provided using EBSD measurements that highlight the complexity and material property gradient, especially with respect to grain size. The discussion on micro-mechanisms governing failure under consequent blast impact loading is guided by microscopy results and microcrack analyses around the shot hole. The effect of microstructural changes induced by fragment perforation on the residual impact resistance of Armox 440T is examined in detail. The fracture mechanisms during full fracture are discussed using fracture surface analysis and cross-sectional microscopy, showing necking and ductile fracture.

In this work the results will be provided according to the sample names and loading cases as provided in Section 3.2. Figure 4.1 shows a DIC frame during Drop weight impact (DWI) testing and a post-test photograph of full fractured plate A7-900. The crack initiates at the hole surface either in shear direction at approximately 45° or initially perpendicular to the length of the plate and changes direction under a similar shear angle. The average values of crack dimensions hole diameter from perforation is presented in Table 4.1, the full fracture data is presented in Appendix A.

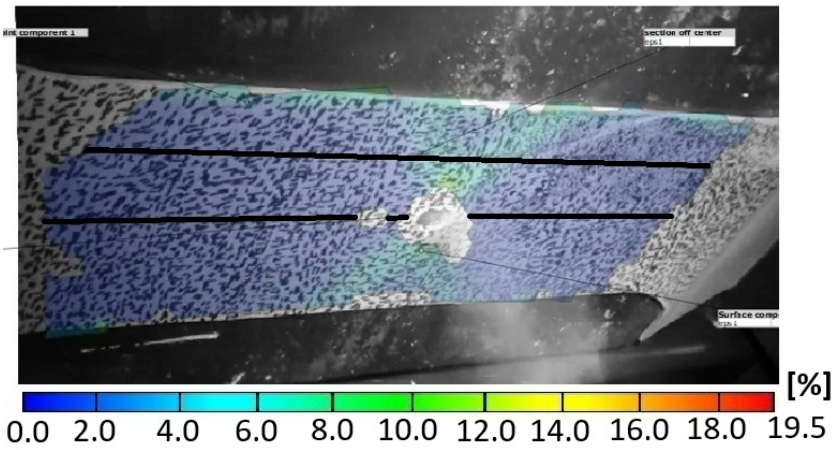
The DIC results revealed that the average far-field strain at crack initiation is close to 1 %, of which only 0.1-0.6 % plastic strain. These are concerning results with regard to blast resistance and require further microstructural characterisation. Specifically, regarding the crack initiation at the holes. The complete analysis of the DIC results can be found in Appendix B.

Table 4.1: Perforation diameter and crack length of full fracture with comparison of perpendicular and diagonal crack growth.

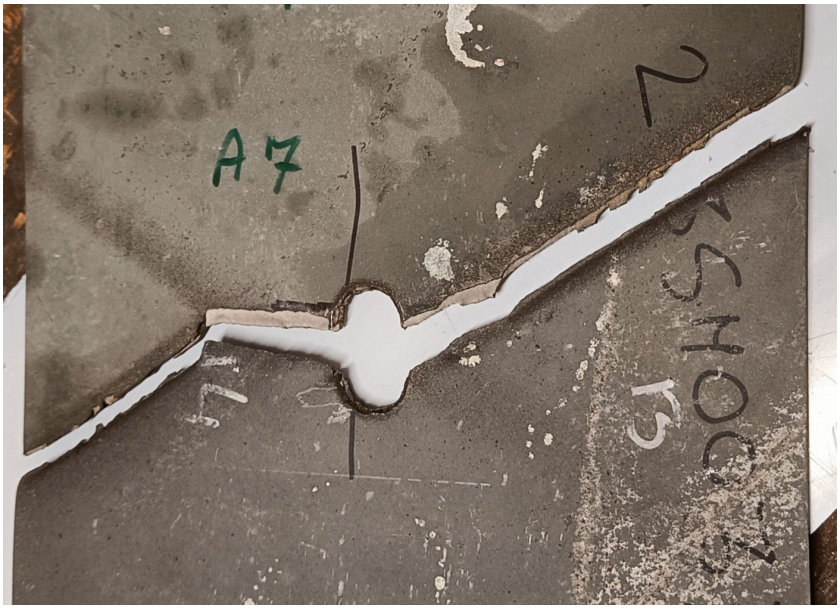
Sample ID ()	Hole diameter [mm]	Perpendicular crack length [mm]	Diagonal crack length [mm]
Average (6) - 900 m/s	23.8 ± 0.68	75 ± 30	236 ± 32
Average (3)- 1600 m/s	30.3 ± 0.44	90 ± 19	209 ± 22

4.1. Fragment perforated hole

First the hole geometry and entrance/exit morphology of the perforated plate is discussed with relation to the perforation velocity. Figure 4.2 shows multiple 2 photographs (a,b) of holes shot at 900 m/s,



(a)



(b)

Figure 4.1: Drop weight impact test (a) DIC result of strain at crack initiation and, (b) top view of plate after perforation and drop weight tower test.

3 micrographs of perforated and DWI loaded hole halves, of which 2 at 900 m/s and 1 at 1600 m/s. As shown visual traces of deformation around the hole quickly decrease with distance. Figure 4.2a shows the entrance effect as the FSP has left a crater-like ring of shear deformation where material has been pushed out at the hole edge. At the exit side, material has sheared outward as shown in Figure 4.2b. These features are also visible in Figure 4.2(c-e). Fracture lines in normal direction can be seen at the hole surface which indicate clean plugging behaviour [23]. The horizontal crack in Figure 4.2c and Figure 4.2e show that perforation can induce internal cracking that can weaken the material against blast impact loading. Of the 9 plates perforated at 900 m/s, only the one in figure 4.2c showed a horizontal central crack. Whereas all three plates perforated at 1600 m/s show a several horizontal cracks distributed from entrance to exit side, the presence of horizontal cracks at higher perforation velocity suggests reduced impact resistance for higher velocity as these cracks act as stress concentrators and crack growth sites.

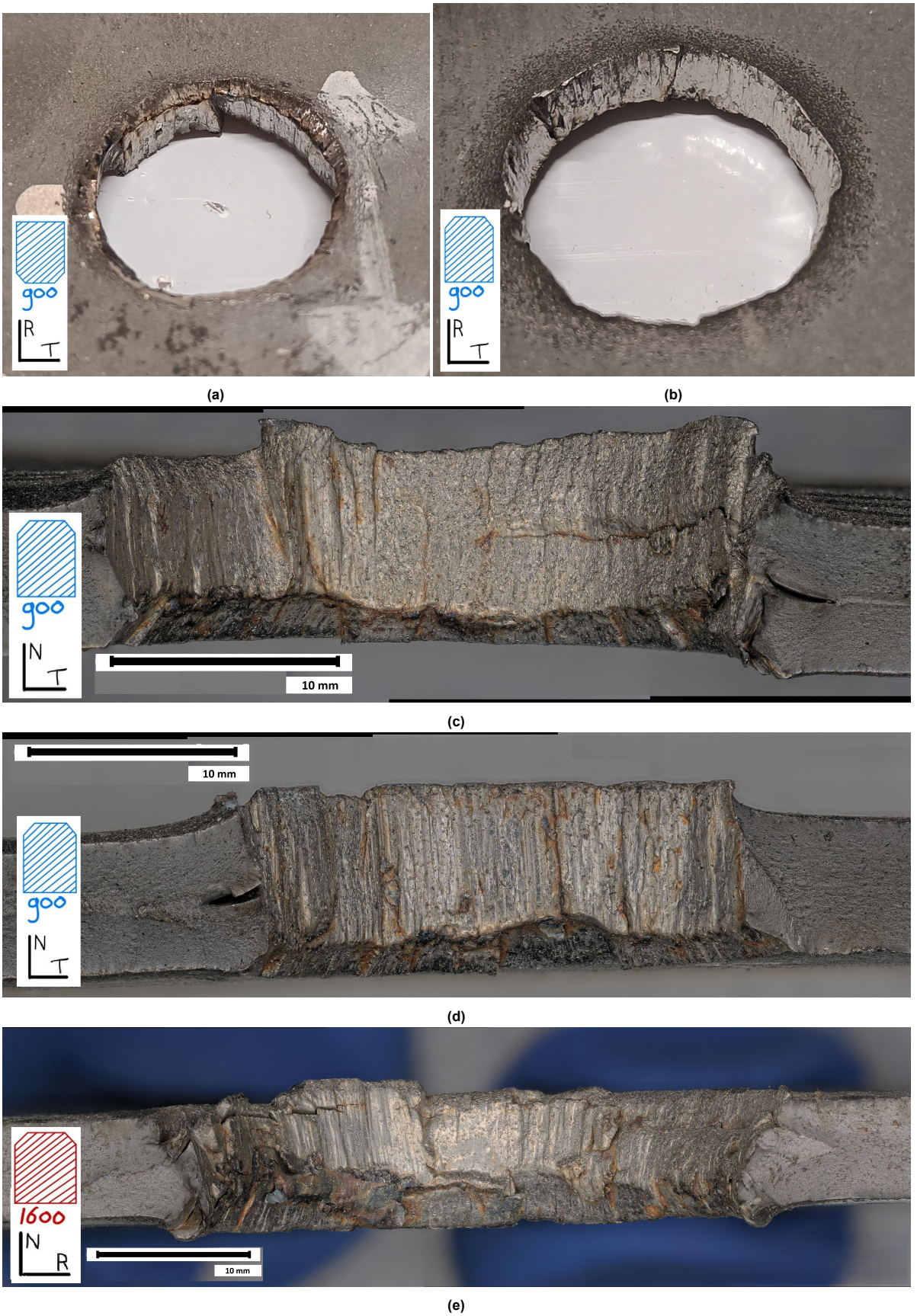


Figure 4.2: Perforated plates and fractured halves after DWI loading, (a-b) Photograph of perforated plates at 900 m/s entrance and exit side, optical microscopy of fractured halves of (c-d) two plates shot at 900 m/s and (e) at 1600 m/s,all scale bars are 2000 μm.

4.1.1. Material deformation

Cross-sections of the different loading conditions are used to investigate the material response, deformation behaviour, and failure micro-mechanisms in the vicinity of the perforation. Figure 4.4a indicates the location of the cross-section shown in 4.4c and similar. The segregation bands present in the base material enable a clear identification of the global deformation behaviour, indicated by the blue lines. Figure 4.4b shows typical deformation behaviour for lower velocity perforation, the red arrows indicate shear deformation lines along which more localised deformation occurs. This localisation comes in the form of shear banding, deformed adiabatic shear banding (dASB) and transformed adiabatic shear banding (tASB) depending on the local loading conditions, which is why the amount of dASB and tASB is significantly higher for perforation at 1600 m/s. Figure 4.4c shows the cross-section of a 900 m/s perforated and DWI tested plate with internal fracture, and Figure 4.4d the cross-section of a 1600 m/s perforated and DWI tested plate. The blue lines that indicate material show that at 900 m/s perforation the material responds by global deformation along the loading direction. Perforation at 1600 m/s induces material flow opposite to the loading direction at the entrance side, and gradually changes to general deformation in the loading direction. The opposite direction shear behaviour is indicated by the red arrows in between which deformed and transformed adiabatic shear bands are present.

The amount of deformation of the affected area varies for the two velocities, the average shear deformation expressed in von Mises equivalent strain following Equation 4.1. The affected area is divided into three sections as illustrated Figure 4.3. The different angles and affected area are measured at multiple positions to find the average deformation, results are shown in Table 4.2.

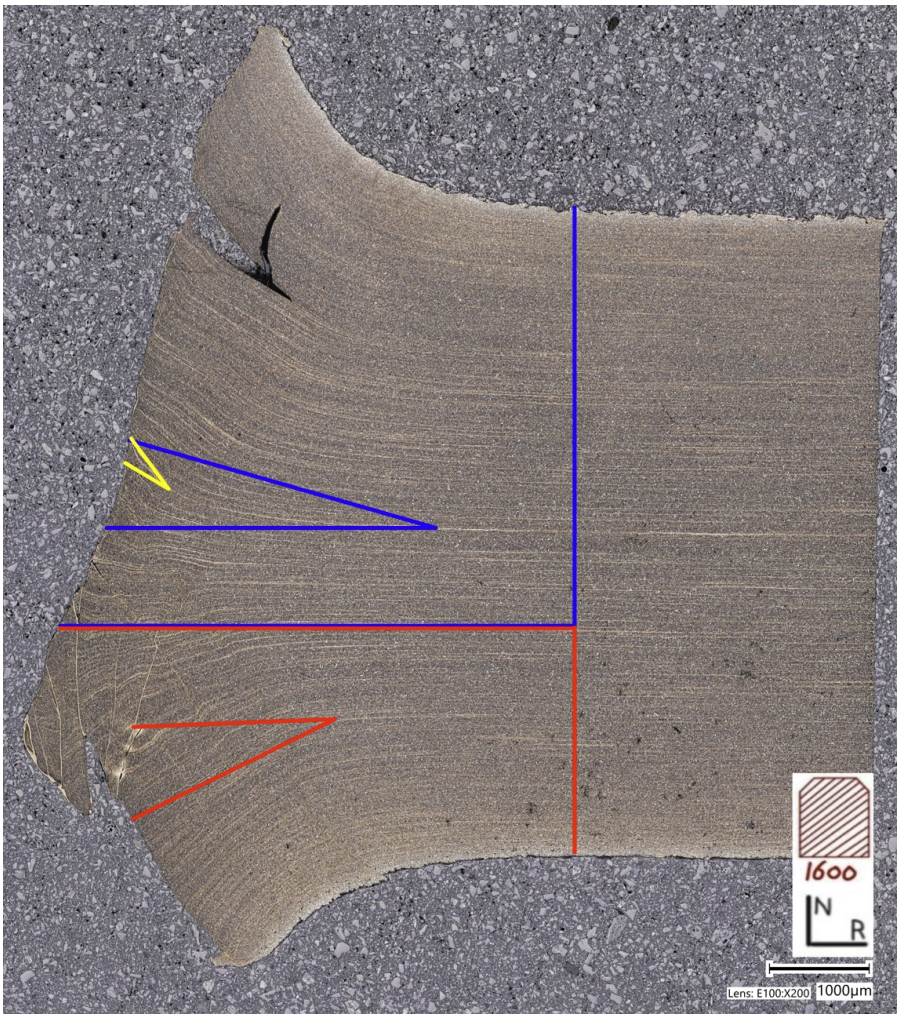


Figure 4.3: Shear angle strain measurements of global deformation on A4-1600 sample divided into three sections, entranceside, exitside and near hole shear angle.

The table shows that increasing velocity also increases the average strain which implies that Armox resistance to perforation is maintained under high strain-rate. The average strain over the affected area is generally low for both strain-rates. However in some cases the localised strain reaches up to 15% near tASBs for 900 m/s and even up to 23% for 1600 m/s, this increase in strain accommodation can be due to the higher energy impact which delocalised deformation, as for 900 m/s most of the deformation is supposedly removed with the plug. The highest deformation is found near the bulge, the transition point between the entrance effect and plugging failure. This region is also more challenging to characterise in the case of 1600 m/s as the complex interaction between tASBs and dASBs in abundance.

$$\epsilon_{VM} = \frac{\theta}{\sqrt{3}} \tag{4.1}$$

Table 4.2: The average shear deformation expressed in von Mises equivalent strain for perforation at 900 m/s and 1600 m/s.

FSP velocity	Effected area strain [%]	Near crack surface strain [-]	Strain at ASBs [-]
900 m/s	3.8 ± 1.8	11.1 ± 1.0	12.3 ± 2.3
1600 m/s	8.2 ± 1.2	13.4 ± 0.6	17.2 ± 4.2

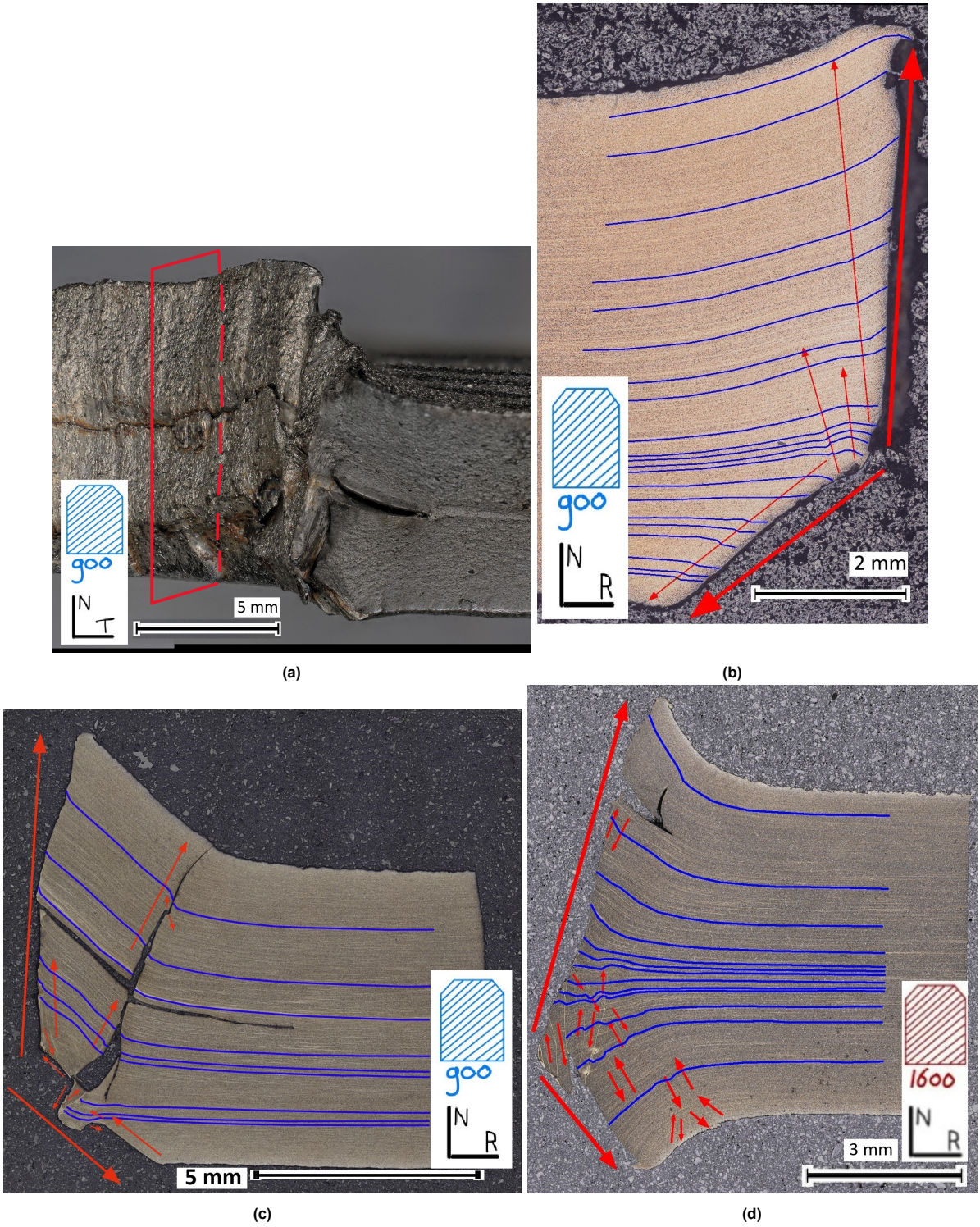


Figure 4.4: Material flow on similar cross-sections of holes as indicated in (a), Material flow behaviour where the red arrows indicate shear deformation lines and the blue lines follow global deformation behaviour, (b) Shot at 900 m/s, (c) shot at 900 m/s and drop weight tested, (d) shot at 1600 m/s and drop weight tested, scale bar of b-d is 1000 μm.

Higher magnification micrographs, as provided in Figure 4.5 clearly show the presence of transformed adiabatic shear bands along the hole surface. During perforation the material in front of the FSP seems to form adiabatic shear bands along which cracks grow until full failure. The tASBs along which failure occurs tend to stay attached at the hole surface; however, as the plug detaches, passes through the plate, and is followed by the deformed FSP the ASBs can be damaged and detached. Remnant pieces

of tASB are left behind, as shown in Figure 4.4 b-c. These characteristics and similar behaviour are found for all plates, which support the idea of plugging failure and emphasise the role of adiabatic shear failure as dominant as failure mechanisms during perforation.

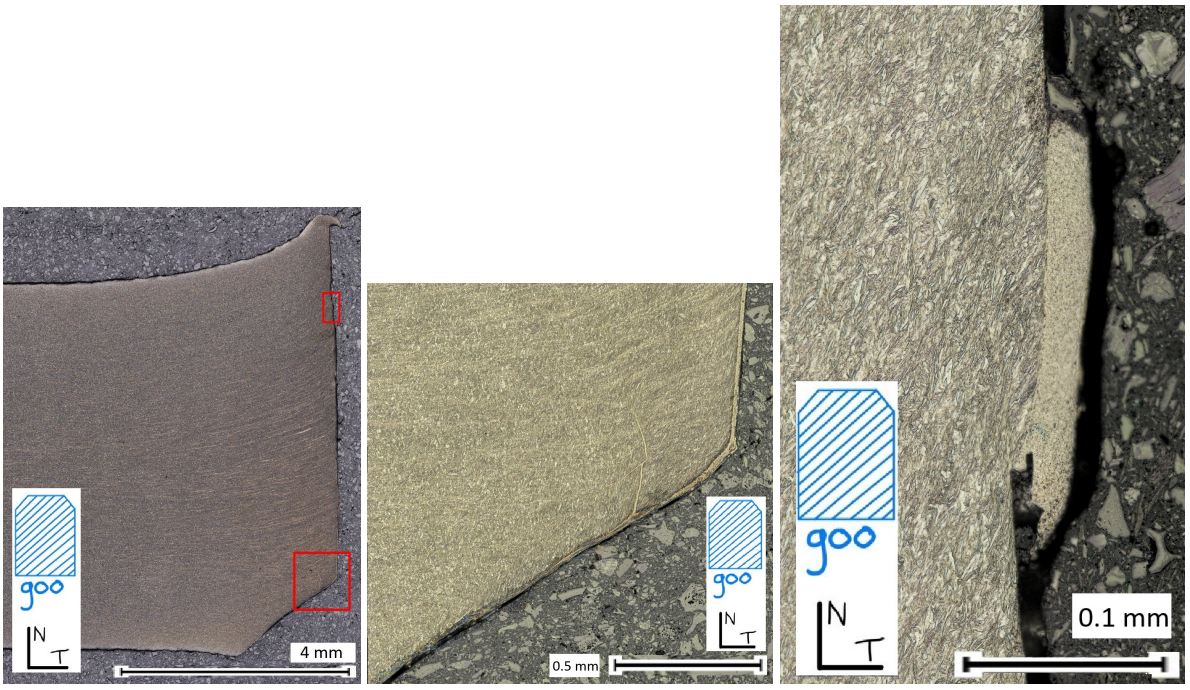


Figure 4.5: Perforated at 900 m/s, (a) micrograph of cross-section with section indication for the similar samples (b-c), scalebar is 1000 μm, (b) micrograph of lower area at end of entrance effect, scale bar is 100 μm, (c) micrograph of upper area with remnant piece of tASB scale bar is 20 μm

Hardness profiles

The material properties in the vicinity change during perforation. Micro-indentation hardness measurements provided cross-section hardness profiles, as shown in Figure 4.6. The scale bars are not equal to emphasise the colour pattern of these figures that highlights regions of more deformation and strain hardening. Most of the strain hardening effect is seen at the entrance side, especially for the highest velocity. In general, the hardness at the hole surface shows increase in hardness, and in Figure 4.6 (e-f) increase in hardness observed around the crack. The local increase of hardness is an indication of the plastic zone size in front of the crack tip. The highest hardness values are found in and around adiabatic shear bands, which contributes to the high hardness found near the entrance and the hole surface.

The hardness in adiabatic shear bands is challenging to measure due to the shear band width and edge effects near the hole surface. The box plot of the average hardness values of the base material, cross-section profiles, and adiabatic shear bands in Figure 4.7 shows an increase in hardness for higher strain-rate. Hardness values around 650 HV0.01 have been found in tASBs, in general the tASB regions near the hole surface show higher hardness then internal tASBs. However, the variation in hardness for adiabatic shear bands complicates property prediction. Figure 4.8 shows a hardness profile in the deformed region with a high density of ASBs. The yellow central region with higher hardness follows along a tASB. These local differences in material properties play an important role in crack initiation and crack growth during blast, and drop weight impact loading. The increase in hardness on a the scale of the whole cross section clearly shows the material deformation from the strian hardening effect of deformation. However the increased hardness in tASBs is the combination of recrystallisation and grain refinement and remaining strain hardening effect.

The perforation morphologies show a shear-governed failure. The next section resolves how ASB density, transformation, and branching determines crack nucleation and growth.

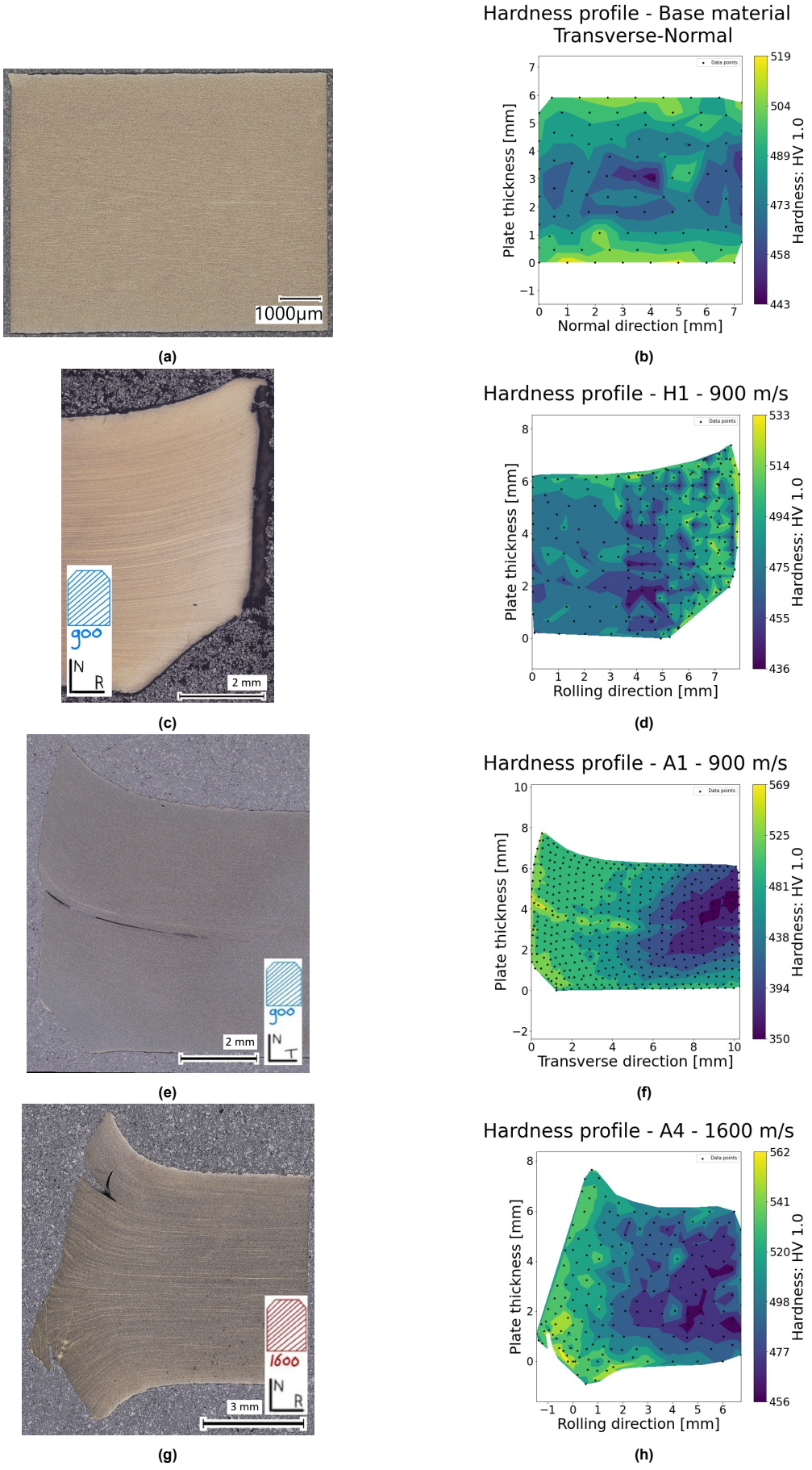


Figure 4.6: Microscopy of sample cross-sections with (a-c), Optical microscopy of H1, A1, A4; (d-f) According hardness profiles H1, A1, A4.

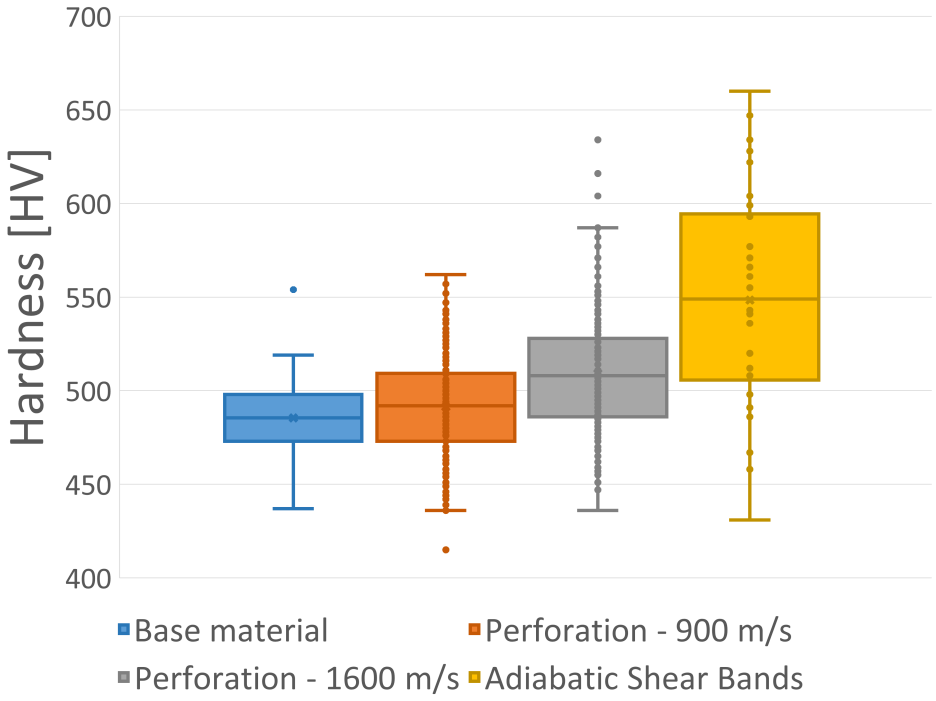


Figure 4.7: Average hardness from hardness profiles of base material, cross-sections near holes shot at 900 m/s and 1600 m/s and micro hardness measurements of transformed adiabatic shear bands

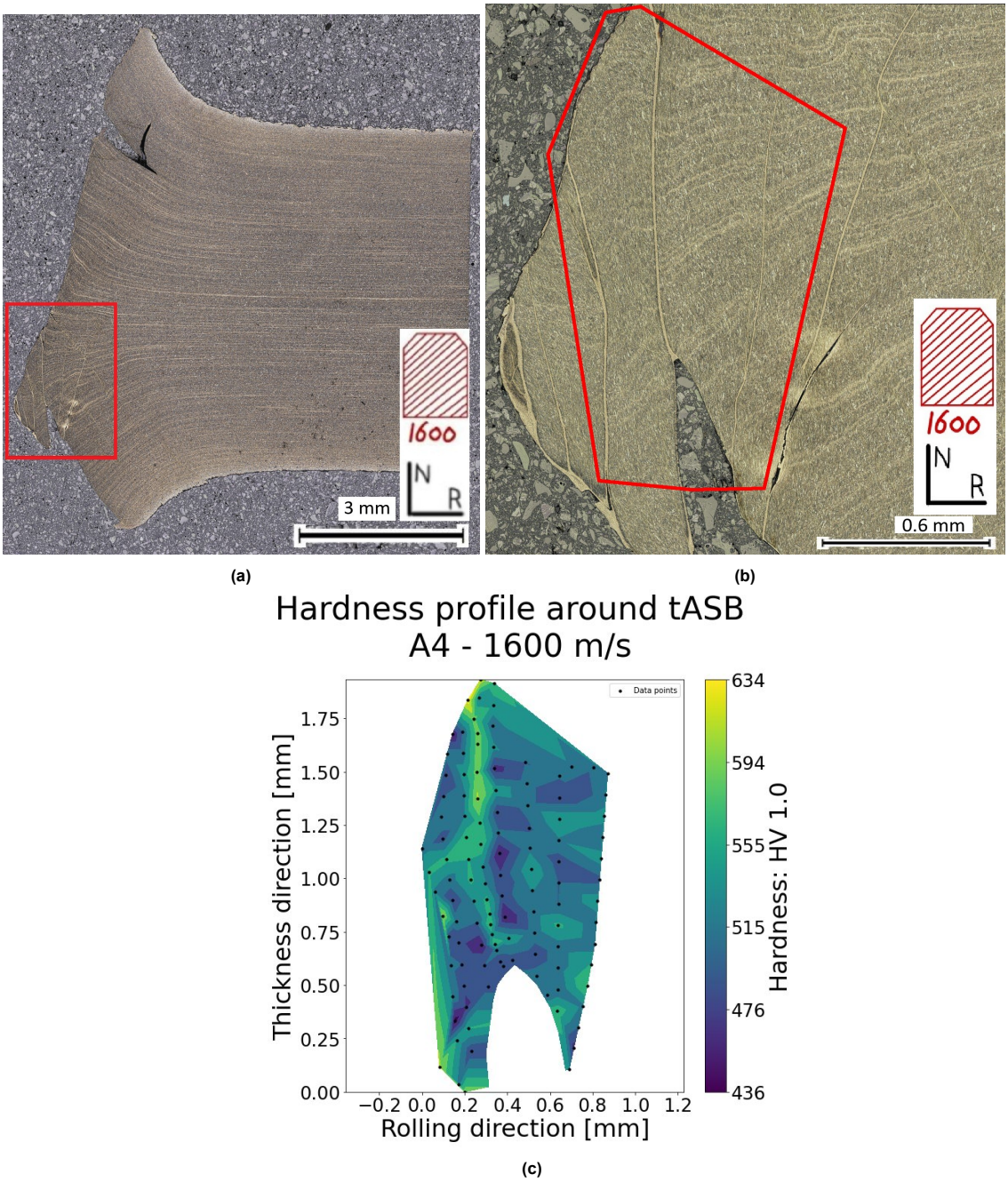


Figure 4.8: Hardness profile of high hole surface region 1600 m/s shot plate with (a) Optical micrograph with section indication, (b) 1000x magnification showcasing several ASBs and profile indication, (c) hardness profile of deformed area near ASB

4.2. Adiabatic shear band characterisation

Further investigation in the failure mechanisms related adiabatic shear bands has been done using OM and SEM. Figure 4.9 shows micrographs of a typical plate shot at 900 m/s, there are a few transformed adiabatic shear bands, that transition into deformed adiabatic shear bands when the shear band does not reach a critical strain threshold to induce microvoids and crack growth through void coalescence before the perforation is completed. A tASB formed near the rim of the entrance effect and a crack initiated inside the tASB as shown in Figure 4.9b. Most internal ASBs form in the transition region between the entrance and exit, in this region ASBs that are formed as a result of shear strain towards the entrance side intersect with ASBs that form to the exit side during plugging as shown in Figure 4.9c.

As shown, adiabatic shear bands form along the hole surface and internally. When the stress state locally exceeds a certain limit, the material can no longer accommodate strain by widening of the ASB and voids are formed inside the tASB. Figure 4.10 shows the distribution of ASBs in a cross-section of 900 m/s-A1 and indicates the presence of microcracks initiated at surface ASB. The SEM results show how the crack initiation in tASB and post-DWI loading crack tip. Figure 4.10d shows that the crack tip has just grown out of its tASB.

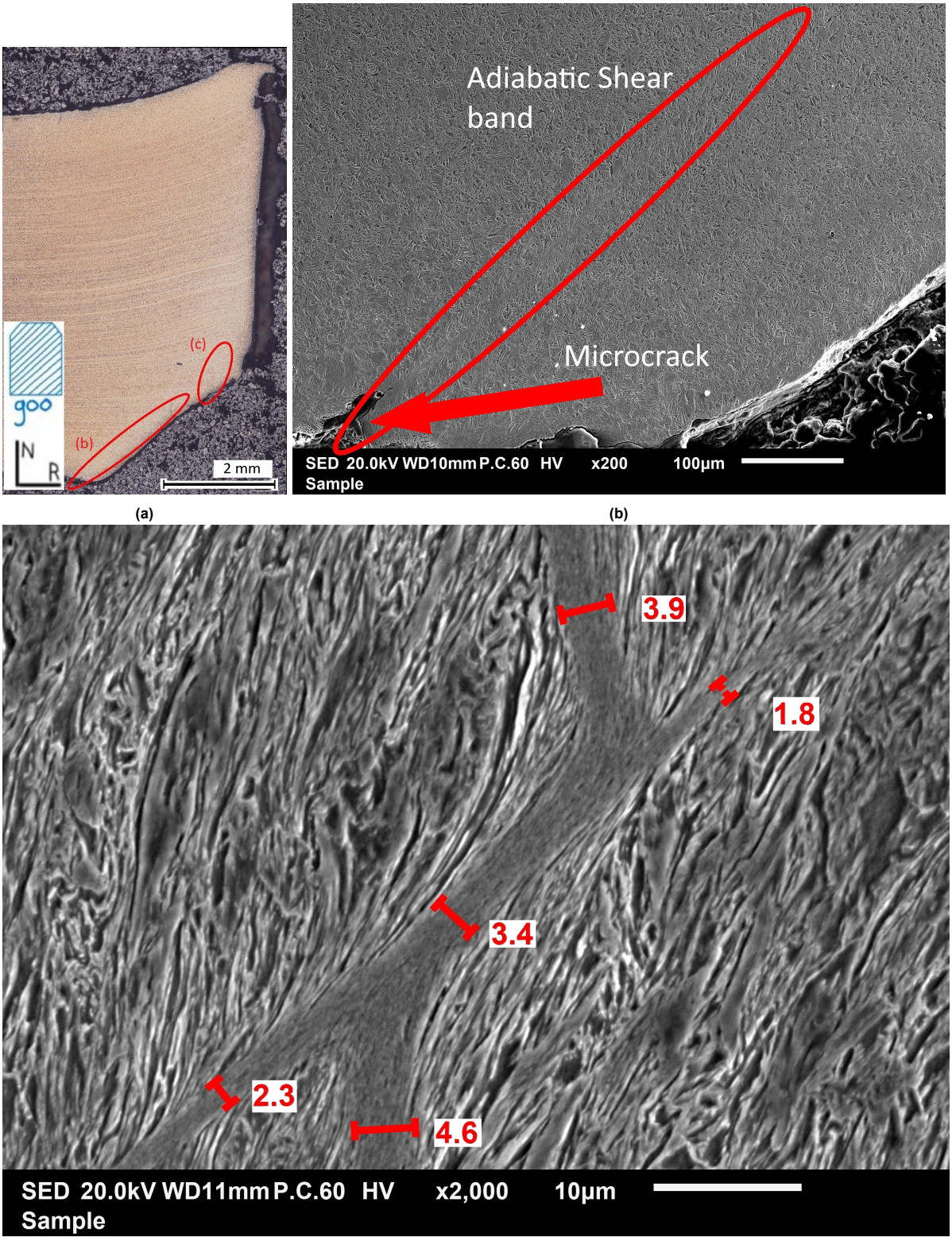


Figure 4.9: High magnification SEM of crack initiation and ASB interactions in the entrance region of 900 m/s-H1, (a) micrograph with highlighted sections, (b) SEM of crack initiation in tASB at the surface plate front, (c) SEM of ASB interaction in the transition region.

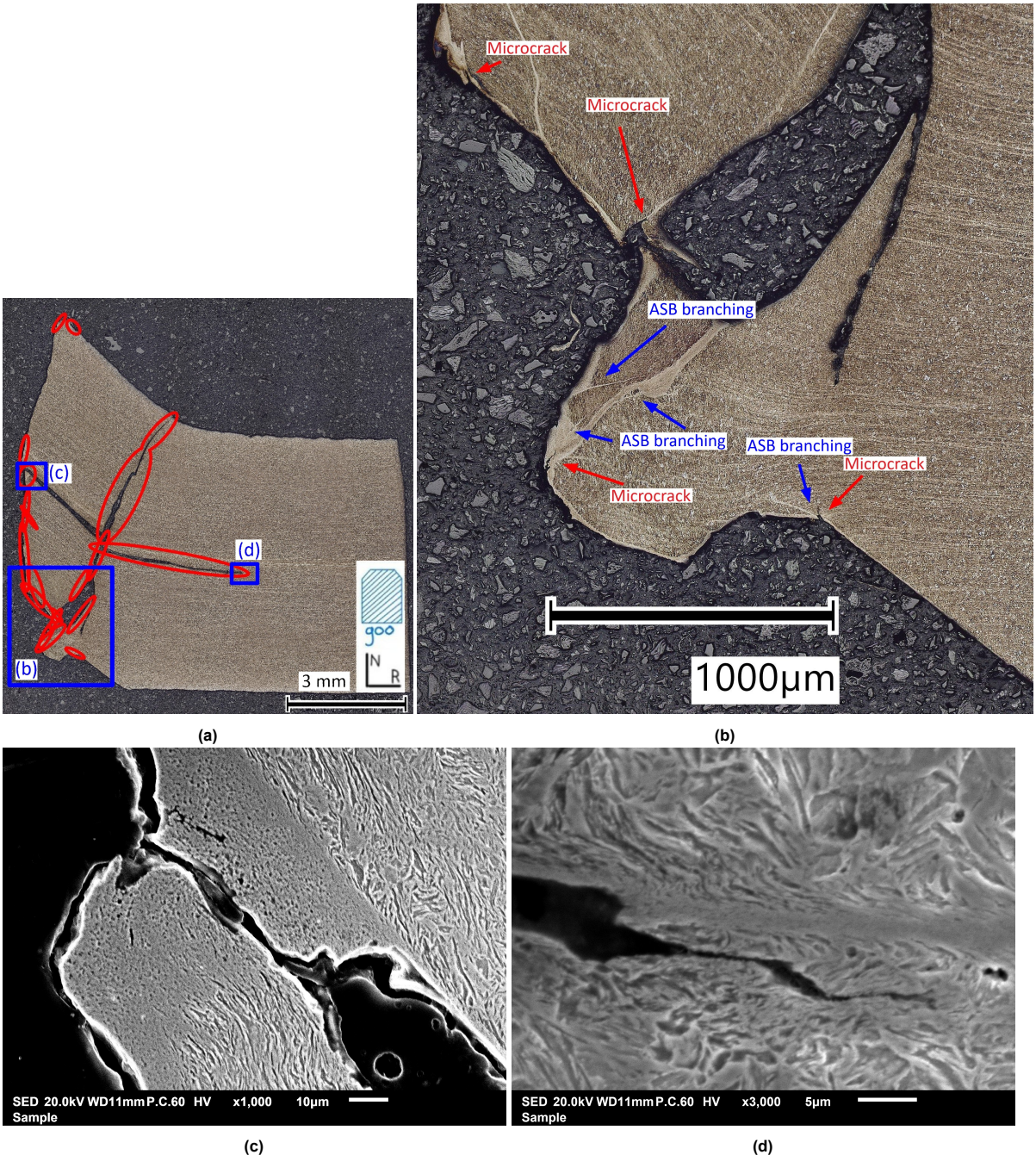


Figure 4.10: Adiabatic shear bands in 900 m/s-A1 plate, (a) OM showcasing presence of adiabatic shear bands and section indication, (b) higher magnification at entrance side, red arrows indicate cracks, blue arrows indicate ASB branching, (c) SEM of crack initiation and growth in tASB at hole surface, (d) SEM of crack tip of central crack growing out of ASB.

The hardness profile measurements have shown that at FSP velocity of 1600 m/s the material accommodates more strain and more strain hardening takes place, this the material also forms a significant amount of tASBs during perforation, especially with respect to internally grown ASBs as shown in Figure 4.11. The increase in number of adiabatic shear bands can be related measured shear per ASB, which is found to be a strain of 15%.

The entrance side of the plate shows considerable amount of tASBs and dASBs, some microcracks at the hole surface and some internal microcracks. The SEM results show the variety of ASB interaction, thickness and failure. Figure 4.11d clearly shows crack growth behaviour through void coalescence. When and how these ASB cracks initiate is unclear as there are no results from plates shot at 1600

m/s without DWI test, however the ductile nature of crack growth shown suggests that these cracks are formed during perforation, similarly to the cracks that lead to plugging.

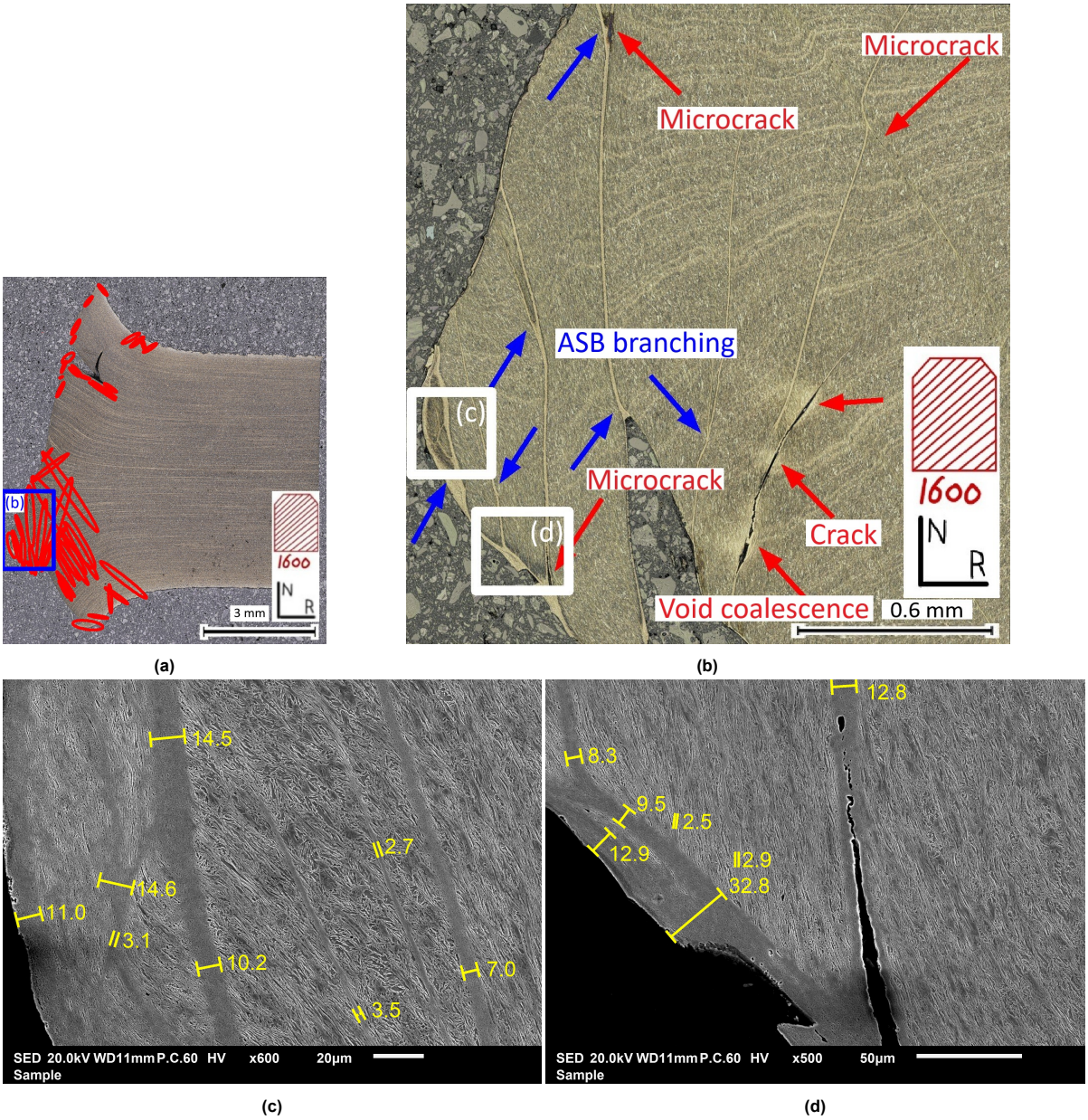


Figure 4.11: Presence of adiabatic shear bands in 1600 m/s-A4, (a) showcases the location and abundance of ASBs, (b) section near hole surface, red arrows indicate cracks, blue arrows indicate ASB branching, and highlighted sections for SEM micrographs (c-d) of high density ASB region with thickness measurements, (d) Shows clear void coalescence crack growth behaviour.

The material properties and response is related to strain-rate and thermal effects, which play an important role in the formation and growth of adiabatic shear bands. At higher perforation velocity the material responds by forming a larger number of ASBs covering a larger spread in size, direction, and position relative to the projectile. These results show that failure under high-velocity perforation initiated by microvoid nucleation and crack growth by void coalescence inside ASBs. dASBs propagate upward from the impact face at 900 m/s they are arrested close to the bulge height, whereas at 1600 m/s they traverse beyond half the plate thickness, producing a characteristic ”step” in deformation. Upon reaching the bulge, dASBs curve inward and upward and produce transverse ASB branches that emerge near the perforation surface in vertical, sub-surface, and angled orientations, often coinciding

with the onset of dASBs. Fracture typically initiates at the tASB-tASB intersections, and residual ASB fragments remain on the hole walls. Table 4.3 provides the ASB analyses of the OM and SEM results related to 900 m/s and 1600 m/s perforation. These results contain the average penetration depth of ASBs, which indicates the depth of reduced toughness due higher hardness ASBs, the average tASB width, and the average microcrack size. The average microcracks after 900 m/s perforation have all been found to have initiated at the hole surface, whereas microcracks found related to 1600 m/s are also found inside the bulk further from the hole surface.

At the exit side tASBs found for 1600 m/s further complicate the deformation field through interaction of the dASB/tASB networks, either developing simultaneously or in iterative stages, as noted by Karantza et al. [53], leading to cracks at junctions averaging around 17.5 μm. Finer sub-bands are observed within larger tASBs, though detailed shear band characterisation is limited by over-etching, complex band interaction and minimum hardness measurement size. Downward-oriented shear effects extend well beyond the bulge, suggesting a failure sequence of ASB formation, shear localisation, dASB development, tASB transformation, band growth, fracture as shown in Section 2.3.1. At 1600 m/s, ASB thicknesses range from 10.8 μm tapering of to 2–3 μm, highlighting the increased complexity of real-world impact. The white etched horizontal bands visible in Figure 4.11b further reveal flow patterns and pronounced ASB activity. The complexity and direction distortion of these horizontal white etched bands underscores the multifaceted nature of perforation driven failure.

Table 4.3: Adiabatic shear band analysis comparing 900 m/s and 1600 m/s.

Perforation velocity [m/s]	ASB penetration depth [μm]	average tASB width [μm]	Average microcrack size [μm]	ASB complexity near surface
900	419 $\pm$ 190	7.3 $\pm$ 3.1	45 $\pm$ 31	Low
1600	2080 $\pm$ 719	4.4 $\pm$ 2.6	17.5 $\pm$ 5.6	High

In the following section the crack initiation and crack growth facilitated by tASBs is discussed. The fracture surfaces are analysed and the effect of ASB formation with relation to full crack growth further discussed.

Microstructure of transformed adiabatic shear bands

To further investigate the microstructural changes in and around tASB, Electron Backscatter Diffraction (EBSD) is done on the base material and the fully tested material. EBSD maps from the Base material are provided in Figure 4.12. Prior austenite grainsize is determined using the Nishiyama-Wassermann relation for a grain boundary angle of 17°-62.8°. The EBSD maps from 1600 m/s-A4 Figure 4.13(a,c,e) about 1 mm from the hole and Figure 4.13(b,d,f) about 2 mm from the hole surface and at the projectile entrance side surface. These measurements are used to determine the martensite packet size, and prior austenite grainsize of the base and the deformed material, as well as the grain size and orientation relation of the transformed adiabatic shear bands. The ultra-fine grains inside tASBs are challenging to measure confidently, as the extreme grain size is low and the number of grain boundaries is high. In the bulk material surrounding the tASB the high deformation and strain hardening induces great distortion of the EBSD results leading to low confidence index results. The grain size averages of these samples are presented in table 4.4. The table shows clear differences between the microstructure of base material and loaded material. The average grain size decreases from 1.6 μm to 0.69 μm after loading taken from an area without ASBs. When an tASB is involved the contribution from the sub-micrometer size grains within tASBs further reduces the average grain size to 0.26 - 0.32 μm. The main difference between the deformed area with tASB and low deformed region with tASB is due to to distance from the hole surface. Close to the hole the material has experience more shear deformation and grains align with the tASB direction, the tASB width is also higher at 13.8 μm. Further away from this high shear deformation the matrix material experiences little deformation, leading to thinner ASBs at 8.7 μm.

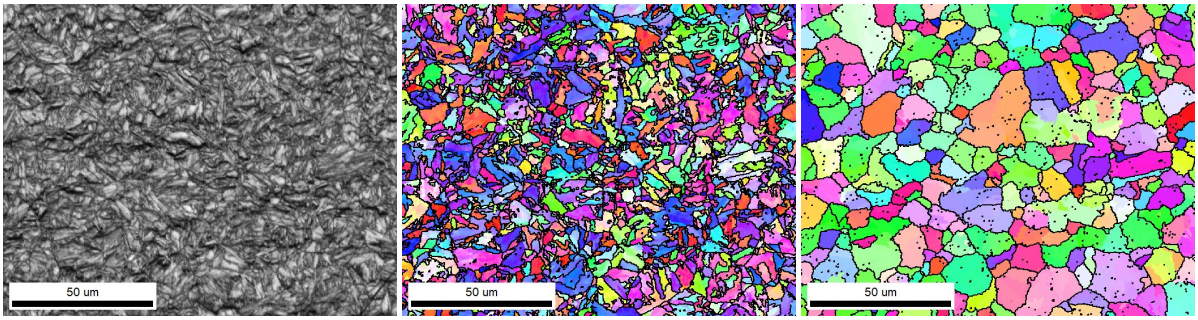
Electron backscatter diffraction (EBSD), combined with Kernel Average Misorientation (KAM) mapping, reveals that adiabatic shear bands (ASBs) consist of nanoscale equiaxed grains with markedly low dislocation density, which is indicative of intense dynamic recrystallisation and pronounced material flow. Xu et al. (2008) [47] showed that under high strain-rate loading, thermal softening elevates

local temperatures, producing narrow shear bands characterised by increased hardness, brittleness, and stress concentrations; by contrast, less severe thermal conditions give rise to wider bands that distribute deformation more evenly. Building on this, Jo et al. (2020) [86] found that austempering ultra-high-strength armour steel raises the critical strain for ASB initiation and yields shorter, finer bands, an outcome attributed to the steel's enhanced strain-hardening capacity.

These observations motivate the hypothesis that tASB networks lower the local fracture resistance along specific paths, a hypothesis tested under DWI in the next section.

Table 4.4: Material grain size at different positions with respect to the perforation at 1600 m/s.

Material	Average grain size [μm]	Standard deviation [μm]
Base material	1.6	1.0
Deformed area no ASB	0.69	0.75
Deformed area with tASB	0.32	0.49
Low deformed region with tASB	0.26	0.19



(a) (b) (c)

Figure 4.12: EBSD of Base material in Rolling - Normal direction with a) Image Quality map, b) Inverse Pole figure map and c) Prior Austenite from Nishiyama-Wassermann relation

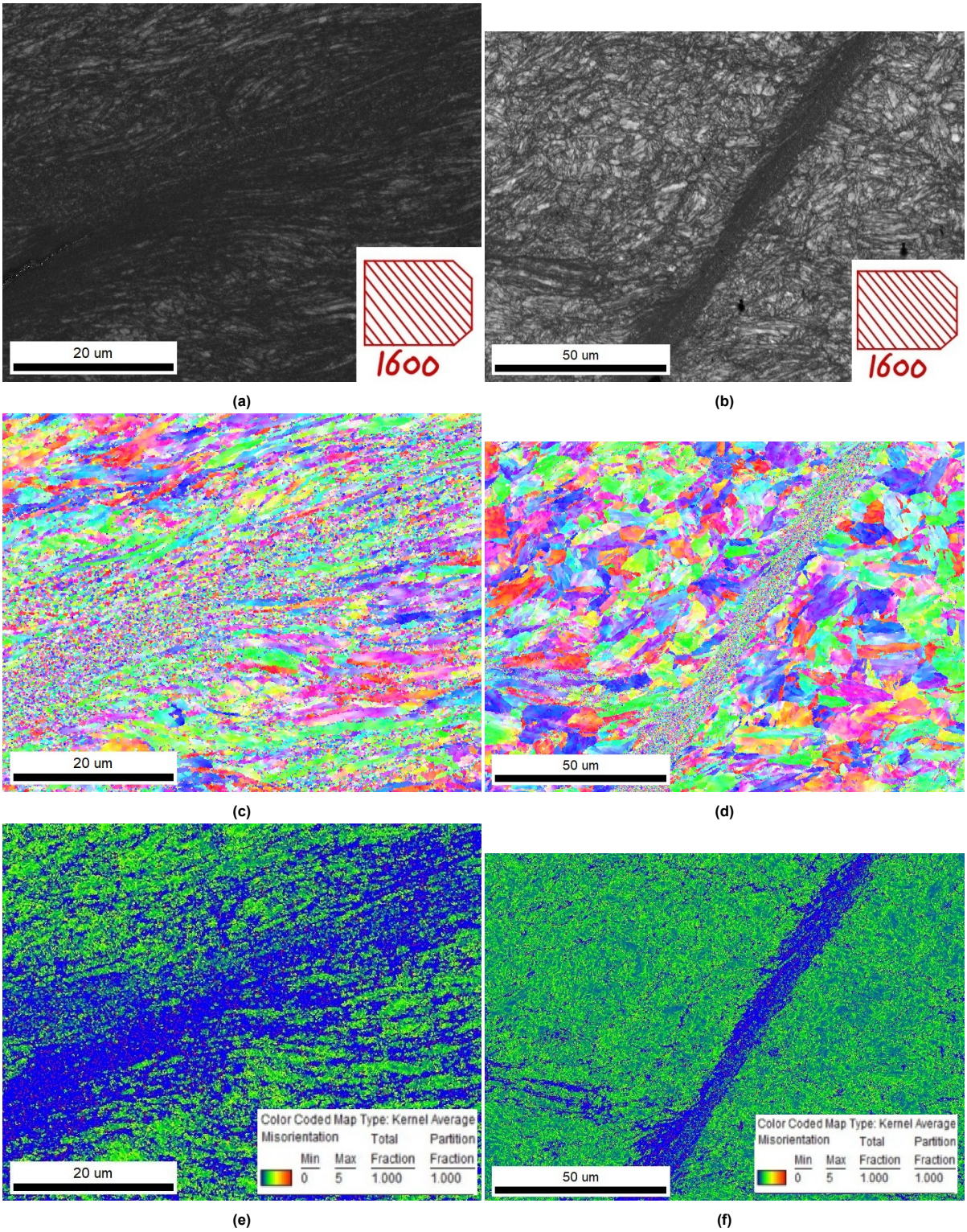


Figure 4.13: EBSD of a drop weight loaded 1600 m/s sample of a centrally located tASB at 1 mm from hole surface a) Image Quality map, c) Inverse Pole figure map, e) Kernel average misorientation map and an tASB at the entrance side surface at 2 mm from the hole surface b) Image Quality map, d) Inverse Pole figure and f) Kernel Misorientation map

4.3. Blast impact failure

High-speed video analysis during drop weight testing reveals an initial wobble of the plate as the drop weight first engages the target, followed by a pronounced flat stretching phase prior to crack nucleation. This flat stretching corresponds to uniform membrane deformation before strain localisation sets in. Once localisation begins, cracks perpendicular to plate length emanate from the hole edge, with measured fracture lengths ranging from millimetres to centimetres depending on impact energy and specimen thickness.

The Digital image correlation (DIC) shown in figure 4.1a of the deformed plates shows a heterogeneous plastic strain field. Peak strains concentrate at the hole rim perpendicular to the loading direction and along the emerging shear bands, while the bulk material exhibits only elastic deformation. After complete perforation, the plate undergoes rapid post-failure relaxation. The strain energy stored in the plate walls is partially released as out-of-plane bending and plate recoil, leading to characteristic petal-like fragment shapes and corrugations on the exit face. The magnitude of this relaxation and the residual deformation are sensitive to both the initial pre-strain state and the dynamic loading rate, although the drop-height varies between 900 m/s and 1600 m/s the drop weight impact produce similar final fracture, which indicates that above a threshold energy level the material response is governed by the presence of adiabatic shear bands, their microcracks and ductile failure processes rather than purely by impact velocity.

4.3.1. Fractography

Fracture surface analysis and cross-sectional microscopy reveal the transition from single face ductile shear failure to V-shaped shear failure with necking. Methods for quantifying dimple parameters, as reviewed by Maruschak (2023) [87], enable detailed characterisation of void-coalescence dimples, while Noell et al. (2018) [88] provide a mechanistic framework for ductile rupture evolution. Table 4.5 shows the fracture type (V-shaped or /-shaped) from different sections of the full fractured surface as illustrated in figure 4.14a. The amount of necking is determined from cross section microscopy as shown in Figure 4.15. The increased necking of the second part shows increased toughness, because a higher volume is deformed, which means that more energy is required for this deformation. This necking deformation is expected to occur into two directions prior to full fracture. The darkened lines shown in Figure 4.1 indicate strain deformation and onset of necking, measurements of this strain have not been recorded yet.

Table 4.5: Necking behaviour of full fracture at different crack directions, perpendicular to plate length (horizontal) and in shear direction (diagonal).

Sample ID & fracture section	Fracture type / V or / - shear shaped	Necking ratio (width min/max)
A1-900 - Horizontal	/	0.93
A4-1600 - Horizontal	V	0.89
A1-900 - Diagonal	V	0.61
A1-900 - Diagonal	/	0.61
A4-1600 - Diagonal	V	0.60
A4-1600 - Diagonal	/	0.69

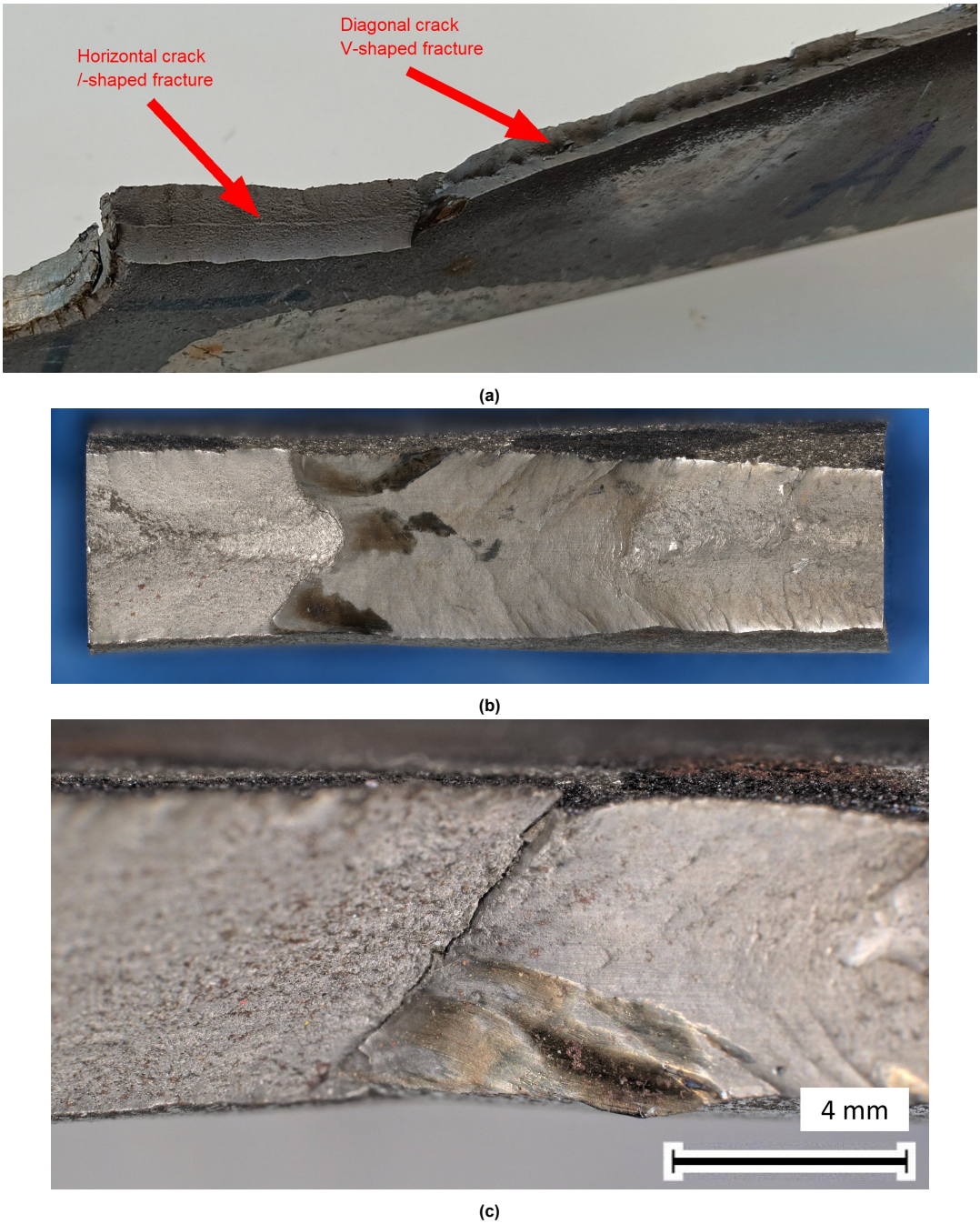


Figure 4.14: Photograph (a) of fracture surface, (b-c) surface sectioned at the fracture direction transition of two fracture surfaces of 1600 m/s samples; left horizontal crack, right diagonal crack direction. Both show increased necking behaviour in diagonal crack direction (right side).

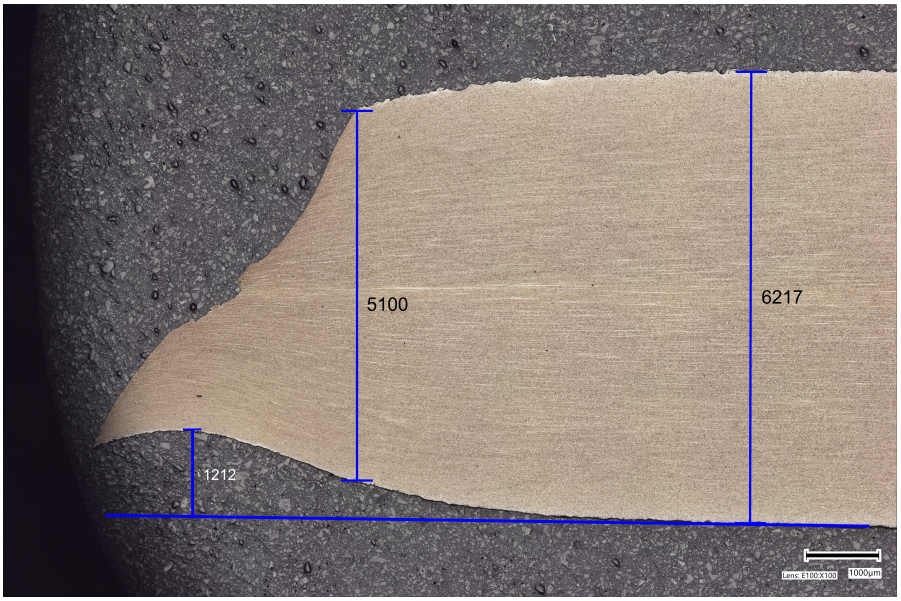


Figure 4.15: Cross section of shear direction fractured surface of a sample shot at 900 m/s used for quantification of necking.

.

The fracture mode depends strongly on the local stress state, during fracture the crack remains in the plane stress state. In plane stress the plastic zone is larger, leading to pronounced necking, out-of-plane shear-lip formation, and a characteristic / and V-shaped fracture profile as seen in Figure 4.14a. However, necking is limited during the initial crack growth perpendicular to the length of the plate. On average after 75 mm the crack direction shifts 45° and follows the direction of the highest shear stress while necking occurs as shown in Figure 4.14. Split fracture often develop where these shear lips pull outward on the central ligament, producing a V-shaped crack. Along the centre of the crack, plastic tearing occurs and localised plasticity. All samples exhibit ductile failure which suggests that above a critical energy input, crack growth remains ductile and does not seem to require initiation from pre-existing microcracks. The differences in hole size and ASB severity do not seem to influence the material response and failure during drop weight impact loading.

4.3.2. Strain energy absorption

Microscopy of the fracture surfaces show uniformly distributed equiaxed dimples. Figure 4.16a shows the centre of the fracture surface. The surface shows ductile shear dimples with a diameter ranging from 0.5 to 20 μm. The absence of foreign inclusions or second-phase particles indicates that these dimples form through grain boundaries decohesion under triaxial load. Figure 4.16b shows the cracked surface near the edge showing directionality in the torn ductile dimples, which indicates shear failure and necking. Table 4.6 shows the average dimple size of different sections along the full fracture. It is clear that the crack behaves similarly at the edges, where necking occurs. But the dimple size in the centre of the crack varies depending on the crack direction as well as the dominant mechanism, the dimple size decreases and becomes more shallow, which indicates lower crack growth resistance once the crack has grown to considerable size. However, the increase in necking with the reduction of shear void coalescence area implies overall increase in toughness.

The strain energy absorbed during crack propagation is intricately linked to the size and morphology of dimples formed by the microvoid coalescence separation mechanism. The average dimple length and dimple area decrease with increasing yield strength (σ_y) and show a direct relationship with plastic strain energy and total elongation [89]. This correlation arises because smaller dimples signify a higher density of microvoid nucleation sites, which requires more energy to drive plastic deformation and surface separation, effectively increasing the work of fracture. The partitioning of the total fracture energy into plasticity and free surface creation further underscore that materials with higher σ_y exhibit reduced plastic zones but greater stored elastic energy, resulting in finer dimple distributions upon failure [90]. Continuum-based microvoid coalescence models, such as the Rice–Tracey model following an expo-

Table 4.6: Fracture surface dimple size comparison

Section	Average dimple size μm	Dominant mechanism
Center - Horizontal	1.98 $\pm$ 2.6	Deep voids - tensile tearing
Edge - Horizontal	1.49 $\pm$ 0.85	Deep voids - shear voidcoalescence
Center - Diagonal	0.95 $\pm$ 0.5	Shallow voids - tensile voidcoalescence
Edge - Diagonal	1.58 $\pm$ 0.9	Deep voids - shear voidcoalescence

nential relation between void dilation and stress triaxiallity [91, 92], express the volumetric growth rate of voids as an exponential function of stress triaxiallity $\eta = \sigma_m/\sigma_y$, with σ_m the Von Mises equivalent stress, and confirm that higher σ_y leads to reduced void size and hence smaller dimples for a given applied load. Together, these findings highlight that yield strength not only determines the onset of plastic flow but also governs the energy absorption capacity by controlling dimple size, providing a microstructural fingerprint of strain energy dissipation on fracture surfaces. Dimple size directly correlates with local strain energy absorption as larger dimples form in regions of higher plastic work, suggesting a robust relationship between dimple morphology and toughness under dynamic loading conditions.

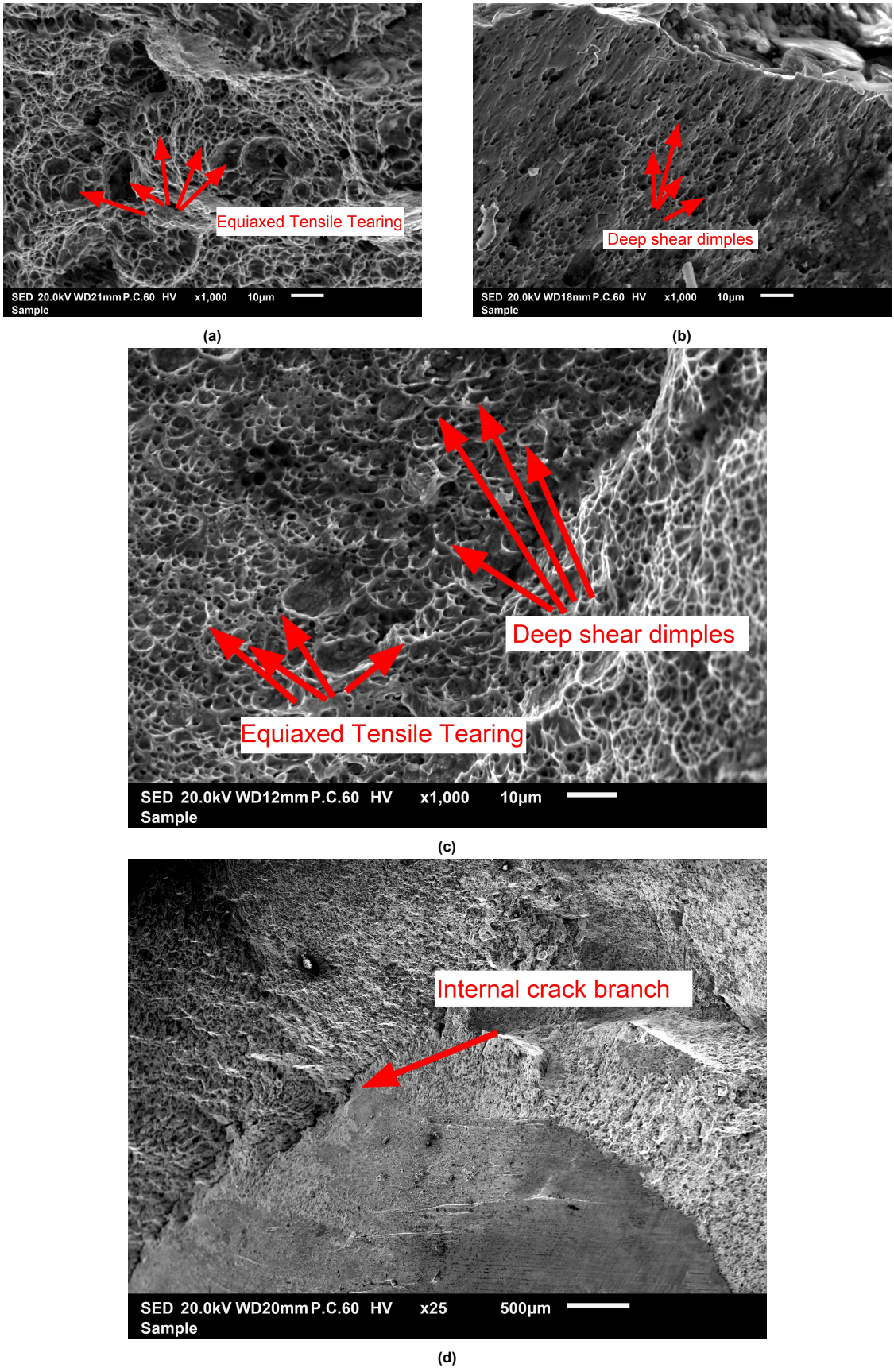


Figure 4.16: SEM of fractured surfaces (a) Center of initially grown crack(b) at the edge of perpendicular crack, (c) fractured surface at change in direction, (d) higher magnification around crack deflection region.

5

Conclusions

This thesis investigated microstructural changes and failure mechanisms in Armox 440T steel subjected to fragment perforation and subsequent drop weight impact loading. The study addressed four key research questions, leading to the following conclusions:

Microstructural Changes and Impact Resistance

Fragment perforation at velocities of 900 m/s and 1600 m/s induces adiabatic shear bands that extend several tens of micrometres into the material. These bands accommodate the highest amount of strain up to 15% for 900 m/s perforation and up to 18 % strain in dASBs found for perforation at 1600 m/s. At lower velocities, ASBs act as preferential sites for crack initiation. At higher velocities, they evolve into interconnected networks with microcracks, significantly reducing the material's resistance to subsequent blast loading by providing initial sharp cracks.

Dominant Failure Mechanisms During Perforation

The transformed ASBs govern a plugging-type failure mode in all tested plates. Both the plug size and the total ASB volume increase with projectile velocity with a $\approx$15% local shear strain at the ASBs. Detailed cross-sectional microscopy revealed transformed shear bands lining the hole walls, confirming adiabatic shear and ductile void coalescence as primary perforation mechanisms.

Crack Propagation Under Drop Weight Loading

Crack growth proceeds via microvoid coalescence localised within ASBs continuing from crack tips at ASBs at the shot hole surfaace or within ASB intersections. These sharp crack tips significantly reduce effective fracture toughness upon blast loading and accelerate unstable crack propagation. However, after the initial phase of crack formation into growth the fracture mechanisms seem unrelated to the origin of crack initiation and far-field strain under subsequent impact loading seems unaffected. This aligns with observed reductions in load-bearing capacity which limits far field plastic strain before failure.

Post-Perforation Material Response

Severe plastic strain during perforation fosters dense networks of shear bands that constrain residual ductility. Consequently, the material locally exhibits diminished load-bearing capacity. For both projectile velocities, plugging failure and strain hardening through the formation of ASBs dominate. Perforation at 900 m/s contains ASBs close to the plugged hole, whereas perforation at 1600 m/s shows increased strain hardening and microstructural heterogeneity by increased number of dASB and tASBs, ASB branching and junctions containing sharp microcracks.

6

Recommendations

Future research is required to deepen the understanding and improve the predictive capability for Armox 440T under high-velocity impact.

Improvements in the methods applied in this thesis.

- To statistically substantiate and verify the results and discussion, more samples need to be analysed for the selected parameters.
- The fracture surface analysis would benefit from comparison with the 1600 m/s samples as well eventhough no significant difference is expected. The completeness of this research would benefit.
- An unfortunate gap in this research is the missing sample shot at 1600 m/s without drop weight testing; including such samples is needed to determine the initiation mechanism of microcracks in ASB junctions at this velocity.

To better understand the behaviour of the material during ASB formation, the following research is highly recommended.

- To **determine the threshold conditions for ASB formation and plug type failure**, and thereby improve the predictions of residual blast resistance, a series of FSP tests can be performed at different subcritical velocities.
- To **determine fragment impact toughness** quantify absorbed energy and determine the deformation mechanisms in both the projectile and Armox plug by integrating high-speed videography and ballistic gel to measure masses and velocities before and after perforation and analyse the recovered fragments.
- To **refine statistical frameworks for shear-band evolution and microcrack formation** under dynamic loading, perform extensive SEM mapping of ASB crossing and branching, as well as surface crack nucleation sites.
- Conduct microhardness and nanoindentation mapping across dASB/tASB regions to profile local property gradients to **enhance constitutive models of post-perforation blast resistance**.

Broadening the research and broaden the scope towards large-scale applications and modelling should consider the following.

Extending the research with the goal of enhancing the performance of Armox 440T by prevention of the formation of adiabatic shear bands must be explored. The concept of adding top layers of different light weight material to reduce the initial stress concentrations provides a promising direction. These top layers can reduce the formation of adiabatic shear bands leading to the full utilisation of the high strength and ductility in fragment resistance.

The high-speed DIC results provided by Appendix B show dissimilar plastic deformation results related to the rolling direction of the plate. However, this difference does not seem to effect the failure

behaviour. Further research on the effect of rolling direction and high strain-rate elongation should provide concluding results with regard to blast energy absorption.

Large scale tests should be conducted with relation to the scenario in which multiple fragments perforate the plate prior to blast loading. This case should be modelled and further tested in combination with structural steel to determine the increased blast resistance by addition of add-on Armox 440T. An other aspect of multiple fragment perforation there might even be a strengthening effect when more initial cracks are present and the energy can be absorbed as multiple cracks grow.

A comparison between welds and shot holes would be very interesting for use case purposes. Shot holes weaken the structure, but if welds remain the weakest section, failure would not be dominated by perforation.

The presence of holes has a detrimental effect on the blast resistance of the plate, however it is not certain that this is the weakest spot, as in most structures welds tend to act as crack initiation sites and are the root of failure. Large scale modelling of armour plates should include weld connections and need to be validated by large scale testing.

Lastly, the crack growth direction generally changes during failure. However, in some cases the crack already initiate under 45° to the loading direction, this discrepancy requires further research combining microstructural analysis at crack initiation and at the crack direction transition region.

The following recommended research topic provide a better fundamental understanding of ASB formation under ballistic conditions.

- Incorporate high-resolution high-speed infrared thermography during Split Hopkinson Pressure Bar testing to **capture the dynamic transient temperature profile and heat generation during ASB formation.**
- **Determine the strain-rate dependency of the Taylor-Quinney coefficient** to improve thermal models.
- **Determine the temperature relation of the yield strength up to high temperatures** to better predict material flow and toughness and improve constitutive models such as the enhanced Johnson-Cook Model.
- Produce a full through thickness 3D mapping around the shot hole to reconstruct the deformation behaviour and contribution of ASBs, their size, shape and orientation. This can be achieved by precise microscopic mapping over controlled iterative grinding distances.
- Use high-resolution transmission electron microscopy (HRTEM) to probe the atomic-scale structures within tASBs and adjacent matrix to further **analyse the nano sized grains and their highly deformed crystal structure.**
- The effect of temperature on the formation of ASBs. In modelling the Taylor-Quinney coefficient is implemented as a constant value. However this coefficient is strain and strain-rate dependent. Taylor-Quinney coefficient determination on Armox and armour steels improve ASB formation modelling.

Implementing these recommendations will improve both fundamental insight into adiabatic shear banding and void-coalescence failure mechanisms at high strain-rate and the engineering reliability of armour steels under extreme loading.

References

[1] I.G. Crouch et al. “Armour steels”. In: *The Science of Armour Materials* (Jan. 2017), pp. 55–115. DOI: 10.1016/B978-0-08-100704-4.00002-5.

[2] L Albert. *Netherlands Details Goalkeeper CIWS Replacement Plans*. Jan. 2021. URL: https://www.overtdefense.com/2021/01/19/netherlands-details-goalkeeper-ciws-replacement-plans/.

[3] Ruben Brekelmans and Gijs Tuinman. *2024 Defence White Paper*. Tech. rep. 2024.

[4] *http://www.defensie.nl/actueel/nieuws/2008/11/09/46118559/de_zeven_provincien_lanceert_harpoons_video*.

[5] *https://www.navylookout.com/royal-navy-participates-in-sinkex-destroying-a-decommissioned-us-frigate-in-the-north-atlantic/*.

[6] R. L. Woodward and M.E. de Morten. “The penetration of metal targets by conical projectiles”. In: *International Journal of Mechanical Sciences* 20.6 (1978), pp. 129–140. ISSN: 00207403. DOI: 10.1016/0020-7403(78)90038-3.

[7] A. Gargano and A. P. Mouritz. “Comparative study of the explosive blast resistance of metal and composite materials used in defence platforms”. In: *Composites Part C: Open Access* 10 (Mar. 2023), p. 100345. ISSN: 2666-6820. DOI: 10.1016/J.JCOMC.2023.100345.

[8] J. E. Field et al. “Review of experimental techniques for high rate deformation and shock studies”. In: *International Journal of Impact Engineering*. Vol. 30. 7. 2004. DOI: 10.1016/j.ijimpeng.2004.03.005.

[9] N. Mehreganian et al. “Response of armour steel plates to localised air blast load - A dimensional analysis”. In: *International Journal of Multiphysics* 11.4 (2017). ISSN: 17509548. DOI: 10.21152/1750-9548.11.4.387.

[10] Hervé Couque. “Adiabatic Shear Bands in Penetrators and Targets”. In: *Adiabatic Shear Localization* (Jan. 2012), pp. 247–266. DOI: 10.1016/B978-0-08-097781-2.00006-X. URL: https://www.sciencedirect.com/science/article/pii/B978008097781200006X?via%3Dihub.

[11] L. W. Meyer, E. Staskewitsch, and A. Burblies. “Adiabatic shear failure under biaxial dynamic compression/ shear loading”. In: *Mechanics of Materials* 17.2-3 (1994). ISSN: 01676636. DOI: 10.1016/0167-6636(94)90060-4.

[12] I.G. Crouch. “Introduction to armour materials”. In: *The Science of Armour Materials*. 2017. DOI: 10.1016/b978-0-08-100704-4.00001-3.

[13] Brodie Marcus Mc. Donald. *Characterising Material Effects in Blast Protection*. Tech. rep. 2019.

[14] SSAB. *Armox 370T Class 1 General Product Description Impact Properties*. Tech. rep. URL: https://www.ssab.com/en/brands-and-products/armox/product-offer/armox-370t-class-1.

[15] SSAB. *Armox 440T General Product Description*. Tech. rep. Feb. 2024. URL: https://www.ssab.com/api/sitecore/Datasheet/Get?key=182f1dad71ab4b7e9b915021bcb26a86_en.

[16] D. D. Showalter et al. “Ballistic testing of ssab ultra-high hardness steel for armor applications”. In: *Proceedings - 24th International Symposium on Ballistics, BALLISTICS 2008*. Vol. 1. 2008.

[17] A. Doig. “Comparative anisotropy of quenched and tempered alloy steel plates made by high quality air melting, ESR, VIM &VAR, and VIM &ESR processes.” In: *Paper Presented at the Sixth International Vacuum Metallurgy Conference on Special Melting, San Diego, CA.* (1979).

[18] D.J. Eyres and G.J. Bruce. *Ship construction 7th edition*. 2012.

[19] Xiang Shao Kong et al. “Experimental and numerical investigation on a multi-layer protective structure under the synergistic effect of blast and fragment loadings”. In: *International Journal of Impact Engineering* 65 (2014). ISSN: 0734743X. DOI: 10.1016/j.ijimpeng.2013.11.009.

[20] S J Cimpoeru. *The Mechanical Metallurgy of Armour Steels*. Tech. rep.

[21] William Gooch et al. “Ballistic Testing of Swedish Steel ARMOX Plate for US Armor Applications”. In: *21st International Symposium on Ballistics* April 2004 (2004).

[22] Xiangshao Kong et al. “A numerical investigation on explosive fragmentation of metal casing using Smoothed Particle Hydrodynamic method”. In: *Materials and Design* 51 (Oct. 2013), pp. 729–741. ISSN: 18734197. DOI: 10.1016/j.matdes.2013.04.041.

[23] Frederik Coghe and Bradley Dodd. “Damage caused to metals by kinetic and chemical energy projectiles”. In: (2015). DOI: 10.13140/RG.2.1.1667.0881. URL: https://www.researchgate.net/publication/278409150.

[24] G. Silsby. *Penetration Mechanics of Anti-Armor Kinetic Energy Penetrators*. Tech. rep. 1984.

[25] Bradley Dodd and Yilong Bai. “Introduction”. In: *Adiabatic Shear Localization* (Jan. 2012), pp. 1–20. DOI: 10.1016/B978-0-08-097781-2.00001-0.

[26] K. C. Dao and D. A. Shockey. “A method for measuring shear-band temperatures”. In: *Journal of Applied Physics* 50.12 (1979). ISSN: 00218979. DOI: 10.1063/1.325926.

[27] R.F. Recht. “Catastrophic Thermo-Plastic Shear”. In: *Appl. Mech.* 31 (1964), pp. 189–193.

[28] Frank Bagusat et al. “High pressure and shock loading experiments”. In: *Dynamic Behavior of Materials: Fundamentals, Material Models, and Microstructure Effects*. 2023. DOI: 10.1016/B978-0-323-99153-7.00006-2.

[29] J. Mescall. *Materials issues in computer simulations of penetration performances*. Ed. by J Chandra and Flaherty J. E. 1983, pp. 47–62.

[30] Na Yan et al. *Shear localization in metallic materials at high strain rates*. 2021. DOI: 10.1016/j.pmatsci.2020.100755.

[31] Min Cheol Jo et al. “Understanding of adiabatic shear band evolution during high-strain-rate deformation in high-strength armor steel”. In: *Journal of Alloys and Compounds* 845 (2020). ISSN: 09258388. DOI: 10.1016/j.jallcom.2020.155540.

[32] D. Ruan, M.A. Kariem, and I.G. Crouch. “High strain rate and specialised testing”. In: *The Science of Armour Materials* (Jan. 2017), pp. 581–637. DOI: 10.1016/B978-0-08-100704-4.00010-4.

[33] *U.S. Army Materials and Mechanics Research Center. Public Affairs Office, & Watertown Arsenal (Mass.). (1963). Plugging type armor penetration by fragment-simulating projectile [Photograph]. Retrieved from https://ark.digitalcommonwealth.org/ark:/50959/vh53z028b*.

[34] M. A. Iqbal et al. “Influence of projectile shape and incidence angle on the ballistic limit and failure mechanism of thick steel plates”. In: *Theoretical and Applied Fracture Mechanics* 62.1 (2012). ISSN: 01678442. DOI: 10.1016/j.tafmec.2013.01.005.

[35] T. Hiroe et al. “Deformation and fragmentation behaviour of exploded metal cylinders and the effects of wall materials, configuration, explosive energy and initiated locations”. In: *International Journal of Impact Engineering* 35.12 (Dec. 2008), pp. 1578–1586. ISSN: 0734-743X. DOI: 10.1016/J.IJIMPENG.2008.07.002.

[36] Lorenzo Iannucci et al. “Project report: Ballistic performance of Armox 370T and Armox 440T steels subjected to 20mm FSPs impact”. In: (2015). DOI: 10.13140/RG.2.1.4110.8643. URL: https://www.researchgate.net/publication/279061555.

[37] John Breeze and Debra J. Carr. “Energised Fragments, Bullets and Fragment Simulating Projectiles”. In: *Blast Injury Science and Engineering*. 2016. DOI: 10.1007/978-3-319-21867-0{_}18.

[38] F Barbillon et al. “Review of fragment simulating projectiles definition and associated quality controls needed”. In: (Oct. 2021), pp. 469–487. DOI: 10.52202/078352-0050. URL: https://doi.org/10.52202/078352-0050.

[39] *MIL-DTL-46593B - Amendment 1*. Tech. rep. Sept. 2008. URL: http://everyspec.com/MIL-SPECS/MIL-SPECS-MIL-DTL/MIL-DTL-46593B_AMENDMENT-1_9195/.

[40] R. F. Recht and T. W. Ipson. “Ballistic perforation dynamics”. In: *Journal of Applied Mechanics, Transactions ASME* 30.3 (1960). ISSN: 15289036. DOI: 10.1115/1.3636566.

[41] I.G. Crouch and B. Eu. “Ballistic testing methodologies”. In: *The Science of Armour Materials* (Jan. 2017), pp. 639–673. DOI: 10.1016/B978-0-08-100704-4.00011-6.

[42] T. Borvik et al. “Perforation of 12mm thick steel plates by 20mm diameter projectiles with flat, hemispherical and conical noses - Part I: Experimental study”. In: *International Journal of Impact Engineering* 27.1 (2001). ISSN: 0734743X. DOI: 10.1016/S0734-743X(01)00034-3.

[43] K. Nowacki and W. Kasprzyk. “The sound velocity in an alloy steel at high-temperature conditions”. In: *International Journal of Thermophysics* 31.1 (2010). ISSN: 0195928X. DOI: 10.1007/s10765-009-0683-2.

[44] Bradley Dodd and Yilong Bai. *Adiabatic Shear Localization*. 2012. DOI: 10.1016/C2011-0-06979-X.

[45] I. Rohr, H. Nahme, and K. Thoma. “Material characterization and constitutive modelling of ductile high strength steel for a wide range of strain rates”. In: *International Journal of Impact Engineering* 31.4 (Apr. 2005), pp. 401–433. ISSN: 0734-743X. DOI: 10.1016/J.IJIMPENG.2004.02.005. URL: https://www.sciencedirect.com/science/article/pii/S0734743X0400034X.

[46] Y. B. Xu et al. “Shear localization and recrystallization in dynamic deformation of 8090 Al-Li alloy”. In: *Materials Science and Engineering A* 299.1-2 (2001). ISSN: 09215093. DOI: 10.1016/S0921-5093(00)01412-X.

[47] Yongbo Xu et al. “Shear localization in dynamic deformation: Microstructural evolution”. In: *Metallurgical and Materials Transactions A: Physical Metallurgy and Materials Science* 39 A.4 (2008). ISSN: 10735623. DOI: 10.1007/s11661-007-9431-z.

[48] Predrag Elek, Slobodan Jaramaz, and Dejan Micković. “Modeling of perforation of plates and multi-layered metallic targets”. In: *International Journal of Solids and Structures* 42.3-4 (Feb. 2005), pp. 1209–1224. ISSN: 0020-7683. DOI: 10.1016/J.IJSOLSTR.2004.06.053. URL: https://www.sciencedirect.com/science/article/pii/S0020768304003762.

[49] Filipe Teixeira-Dias, Nicholas Smith, and Elias Galiounas. “Analytical and Energy-Based Methods for Penetration Mechanics”. In: *Encyclopedia of Continuum Mechanics*. 2020. DOI: 10.1007/978-3-662-55771-6{_}207.

[50] Marvin E. Backman and Werner Goldsmith. “The mechanics of penetration of projectiles into targets”. In: *International Journal of Engineering Science* 16.1 (1978), pp. 1–99. ISSN: 00207225. DOI: 10.1016/0020-7225(78)90002-2.

[51] J. Awerbuch and S. R. Bodner. “Experimental investigation of normal perforation of projectiles in metallic plates”. In: *International Journal of Solids and Structures* 10.6 (1974). ISSN: 00207683. DOI: 10.1016/0020-7683(74)90051-1.

[52] A. Marchand and J. Duffy. “An experimental study of the formation process of adiabatic shear bands in a structural steel”. In: *Journal of the Mechanics and Physics of Solids* 36.3 (1988). ISSN: 00225096. DOI: 10.1016/0022-5096(88)90012-9.

[53] Konstantina D. Karantza and Dimitrios E. Manolakos. *A Review on the Adiabatic Shear Banding Mechanism in Metals and Alloys Considering Microstructural Characteristics, Morphology and Fracture*. 2023. DOI: 10.3390/met13121988.

[54] F. Pursche and L. W. Meyer. “Correlation between dynamic material behavior and adiabatic shear phenomenon for quenched and tempered steels”. In: *Engineering Transactions* 59.2 (2011).

[55] Daniel Rittel, Juan Carlos Nieto-Fuentes, and Mikko Hokka. “Dynamic shear failure: The underlying physics”. In: *Dynamic Behavior of Materials: Fundamentals, Material Models, and Microstructure Effects* (Jan. 2024), pp. 117–132. DOI: 10.1016/B978-0-323-99153-7.00003-7. URL: https://www.sciencedirect.com/science/article/pii/B9780323991537000037?via%3Dihub.

[56] N. Li et al. “Localized amorphism after high-strain-rate deformation in TWIP steel”. In: *Acta Materialia* 59.16 (2011). ISSN: 13596454. DOI: 10.1016/j.actamat.2011.06.048.

[57] C. Zener and J. H. Hollomon. “Effect of strain rate upon plastic flow of steel”. In: *Journal of Applied Physics* 15.1 (1944). ISSN: 00218979. DOI: 10.1063/1.1707363.

[58] H C Rogers. “Adiabatic Plastic Deformation”. In: *Annual Review of Materials Science* 9.1 (1979). ISSN: 0084-6600. DOI: 10.1146/annurev.ms.09.080179.001435.

[59] “The emission of the latent energy due to previous cold working when a metal is heated”. In: *Proceedings of the Royal Society of London. Series A - Mathematical and Physical Sciences* 163.913 (1937). ISSN: 0080-4630. DOI: 10.1098/rspa.1937.0217.

[60] “The heat developed during plastic extension of metals”. In: *Proceedings of the Royal Society of London. Series A, Containing Papers of a Mathematical and Physical Character* 107.743 (1925). ISSN: 0950-1207. DOI: 10.1098/rspa.1925.0034.

[61] G. C. Soares and M. Hokka. “The Taylor–Quinney coefficients and strain hardening of commercially pure titanium, iron, copper, and tin in high rate compression”. In: *International Journal of Impact Engineering* 156 (2021). ISSN: 0734743X. DOI: 10.1016/j.ijimpeng.2021.103940.

[62] Y. B. Xu et al. “Formation, microstructure and development of the localized shear deformation in low-carbon steels”. In: *Acta Materialia* 44.5 (1996). ISSN: 13596454. DOI: 10.1016/1359-6454(95)00306-1.

[63] Thomas W. Wright. “Theory of Adiabatic Shear Bands”. In: *Adiabatic Shear Localization* (Jan. 2012), pp. 215–246. DOI: 10.1016/B978-0-08-097781-2.00005-8. URL: https://www.sciencedirect.com/science/article/pii/B9780080977812000058?via%3Dihub.

[64] B. Dodd and Y.L. Bai. “.Mater. Sci. Eng.” In: 5 (1989), p. 557.

[65] Jacques H. Giovanola. “Adiabatic shear banding under pure shear loading Part I: direct observation of strain localization and energy dissipation measurements”. In: *Mechanics of Materials* 7.1 (Sept. 1988), pp. 59–71. ISSN: 0167-6636. DOI: 10.1016/0167-6636(88)90006-3. URL: https://www.sciencedirect.com/science/article/abs/pii/0167663688900063.

[66] L. E. Murr et al. “Adiabatic shear bands and examples of their role in severe plastic deformation”. In: *Journal of Materials Science* 37.16 (2002), p. 3337. ISSN: 00222461. DOI: 10.1023/A:1016541023502.

[67] D. E. Grady and M. E. Kipp. “The growth of unstable thermoplastic shear with application to steady-wave shock compression in solids*”. In: *Journal of the Mechanics and Physics of Solids* 35.1 (Jan. 1987), pp. 95–119. ISSN: 0022-5096. DOI: 10.1016/0022-5096(87)90030-5. URL: https://www.sciencedirect.com/science/article/pii/0022509687900305?via%3Dihub.

[68] M. Zhou, A. J. Rosakis, and G. Ravichandran. “Dynamically propagating shear bands in impact-loaded prenotched plates—I. Experimental investigations of temperature signatures and propagation speed”. In: *Journal of the Mechanics and Physics of Solids* 44.6 (June 1996), pp. 981–1006. ISSN: 0022-5096. DOI: 10.1016/0022-5096(96)00003-8. URL: https://www.sciencedirect.com/science/article/pii/0022509696000038?via%3Dihub.

[69] Q. Xue and III T. Gray. “Development of adiabatic shear bands in annealed 316L stainless steel: Part II. TEM studies of the evolution of microstructure during deformation localization”. In: *Metallurgical and Materials Transactions A: Physical Metallurgy and Materials Science* 37.8 (2006). ISSN: 10735623. DOI: 10.1007/BF02586218.

[70] S. Mercier and A. Molinari. “Steady-State shear band propagation under dynamic conditions”. In: *Journal of the Mechanics and Physics of Solids* 46.8 (Aug. 1998), pp. 1463–1495. ISSN: 0022-5096. DOI: 10.1016/S0022-5096(97)00069-0. URL: https://www.sciencedirect.com/science/article/pii/S0022509697000690.

[71] A. Banerjee et al. “Determination of Johnson cook material and failure model constants and numerical modelling of Charpy impact test of armour steel”. In: *Materials Science and Engineering: A* 640 (2015). ISSN: 09215093. DOI: 10.1016/j.msea.2015.05.073.

[72] T Deniz. “Ballistic penetration of hardened steel plates”. In: *27th International Symposium on Ballistics* 22 (2010).

[73] L. W. Meyer et al. “Experimental investigations and modelling of strain rate and temperature effects on the flow behaviour of 1045 steel”. In: *Journal De Physique. IV : JP*. Vol. 134. 2006. DOI: 10.1051/jp4:2006134013.

[74] G. R. Johnson et al. “Response of various metals to large torsional strains over a large range of strain rates-part 2: Less ductile metals”. In: *Journal of Engineering Materials and Technology, Transactions of the ASME* 105.1 (1983). ISSN: 15288889. DOI: 10.1115/1.3225618.

[75] Gordon R Johnson and William H Cook. “A Computational Constitutive Model and Data for Metals Subjected to Large Strain, High Strain Rates and High Pressures”. In: *Proceedings 7th International Symposium on Ballistics* (1983).

[76] N. Mehreganian et al. “The response of mild steel and armour steel plates to localised air-blast loading-comparison of numerical modelling techniques”. In: *International Journal of Impact Engineering* 115 (2018). ISSN: 0734743X. DOI: 10.1016/j.ijimpeng.2018.01.010.

[77] T. Ngo et al. “Blast loading and blast effects on structures - An overview”. In: *Electronic Journal of Structural Engineering* 7 (2007). ISSN: 14439255. DOI: 10.56748/ejse.671.

[78] Kartikeya, Sanjay Prasad, and Naresh Bhatnagar. “Finite element simulation of armor steel used for blast protection”. In: *Procedia Structural Integrity*. Vol. 14. 2019. DOI: 10.1016/j.prostr.2019.05.066.

[79] G. S. Langdon, W. C. Lee, and L. A. Louca. “The influence of material type on the response of plates to air-blast loading”. In: *International Journal of Impact Engineering* 78 (2015). ISSN: 0734743X. DOI: 10.1016/j.ijimpeng.2014.12.008.

[80] M. Janssen, J. Zuidema, and R.J.H. Wanhill. *Fracture Mechanics: An Engineering Primer*. 2024. DOI: 10.59490/tb.86.

[81] G. R. Irwin. “Analysis of Stresses and Strains Near the End of a Crack Traversing a Plate”. In: *Journal of Applied Mechanics* 24.3 (1957). ISSN: 0021-8936. DOI: 10.1115/1.4011547.

[82] Xiang Liu. “On some eigenvalue problems for elastic instabilities in tension ”. In: *10.13140/RG.2.1.4519.4004.* (2013).

[83] G. R. Speich and W. C. Leslie. “Tempering of Steel”. In: *Metall Trans* 3.5 (1972). ISSN: 0026-086X. DOI: 10.1007/BF02642436.

[84] H. B. Motra, J. Hildebrand, and A. Dimmig-Osburg. “Assessment of strain measurement techniques to characterise mechanical properties of structural steel”. In: *Engineering Science and Technology, an International Journal* 17.4 (2014). ISSN: 22150986. DOI: 10.1016/j.jestch.2014.07.006.

[85] B. Landkof and W. Goldsmith. “Petalling of thin, metallic plates during penetration by cylindro-conical projectiles”. In: *International Journal of Solids and Structures* 21.3 (1985), pp. 245–266. ISSN: 00207683. DOI: 10.1016/0020-7683(85)90021-6.

[86] Min Cheol Jo et al. “Effect of tempering conditions on adiabatic shear banding during dynamic compression and ballistic impact tests of ultra-high-strength armor steel”. In: *Materials Science and Engineering: A* 792 (Aug. 2020), p. 139818. ISSN: 0921-5093. DOI: 10.1016/J.MSEA.2020.139818. URL: https://www.sciencedirect.com/science/article/pii/S0921509320308911.

[87] Pavlo Maruschak, Ihor Konovalenko, and Andrii Sorochak. “Methods for evaluating fracture patterns of polycrystalline materials based on the parameter analysis of ductile separation dimples: A review”. In: *Engineering Failure Analysis* 153 (Nov. 2023), p. 107587. ISSN: 1350-6307. DOI: 10.1016/J.ENGFAILANAL.2023.107587. URL: https://www.sciencedirect.com/science/article/pii/S1350630723005411.

[88] Philip J. Noell, Jay D. Carroll, and Brad L. Boyce. “The mechanisms of ductile rupture”. In: *Acta Materialia* 161 (2018). ISSN: 13596454. DOI: 10.1016/j.actamat.2018.09.006.

[89] Arpan Das. “Correlation of fractographic dimple geometry with microstructural and mechanical properties of an ultrahigh-strength steel”. In: *MRS Communications* (June 2025). ISSN: 21596867. DOI: 10.1557/s43579-025-00725-w.

[90] I. Tarhouni et al. “Modelling of ductile fracture considering the effect of stress triaxiality and the energy partition theory in thin high-strength steel sheets”. In: *International Journal of Fracture* 250.1 (Mar. 2025). ISSN: 15732673. DOI: 10.1007/s10704-025-00844-4.

[91] Ravi Kiran and Kapil Khandelwal. “Computational Models for Ductile Fracture Prediction in Structural Engineering Applications”. In: *Procedia Materials Science* 3 (Jan. 2014), pp. 1947–1955. ISSN: 2211-8128. DOI: 10.1016/J.MSPRO.2014.06.314. URL: https://www.sciencedirect.com/science/article/pii/S2211812814003150.

[92] J. R. Rice and D. M. Tracey. “On the ductile enlargement of voids in triaxial stress fields*”. In: *Journal of the Mechanics and Physics of Solids* 17.3 (1969). ISSN: 00225096. DOI: 10.1016/0022-5096(69)90033-7.

A

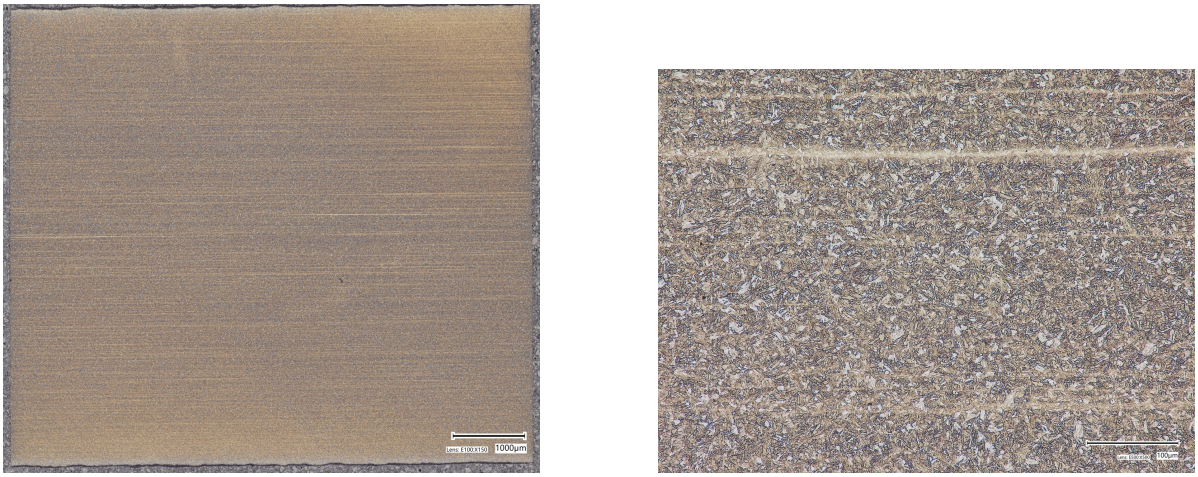
Appendix A: Base material and sample characterisation

A.1. Optical microscopy of base material



(a) (b)

Figure A.1: Base material cross-section with horizontally the transverse and vertically the normal direction, (a) Full thickness, (b) 500X magnification



(a) (b)

Figure A.2: Base material cross-section with horizontally the rolling and vertically the normal direction, (a) Full thickness, (b) 500X magnification



(a) (b)

Figure A.3: Base material surface with horizontally the rolling and vertically the transverse direction, (a) Polished top surface of plate, (b) 500X magnification

A.2. Sample characterisation

Table A.1: Sample characteristics and hole diameter.

Sample ID	FSP Velocity [m/s]	Inner diameter shot hole [mm]	Outer diameter shot hole [mm]
A1	900	24.1	28.1
A2	900	23.7	28.2
A3	900	23.1	27.3
A6	900	22.9	29.0
A7	900	23.4	28.3
A8	900	25.5	28.9
A4	1600	29.6	34.9
A5	1600	30.7	35.9
A9	1600	30.5	34.6
Average dimensions	900	23.8 ± 0.68	28.3 ± 0.43
Average dimensions	1600	30.3 ± 0.44	35.1 ± 0.51

Table A.2: Sample full fracture analysis, total length of surface of the sections perpendicular and diagonal to the loading direction.

Sample ID	FSP Velocity [m/s]	Perpendicular fracture length [mm]	Diagonal fracture length [mm]	Fracture surface total [mm]
A1	900	67	251	384
A2	900	32	278	343
A3	900	36	274	347
A6	900	108	209	425
A7	900	91	219	401
A8	900	117	182	416
A4	1600	76	230	382
A5	1600	75	222	371
A9	1600	118	176	412
Average dimensions	900	75 ± 30	236 ± 32	386 ± 28
Average dimensions	1600	90 ± 19	209 ± 22	388 ± 16

A.3. Fractured surface cross section analysis

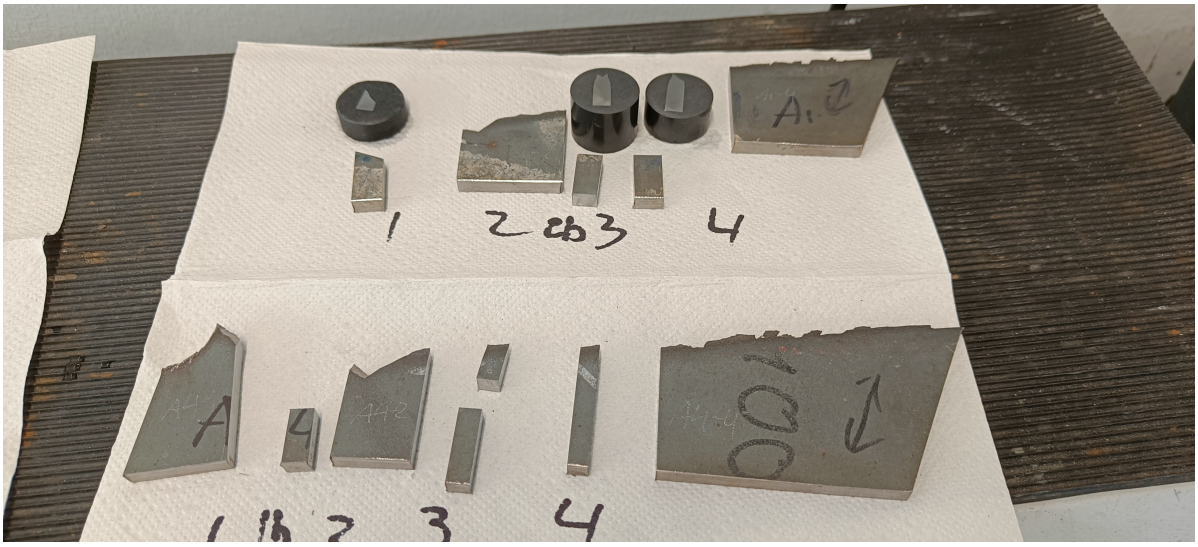


Figure A.4: Overview of fracture surface samples as taken from A1-900 and A4-1600

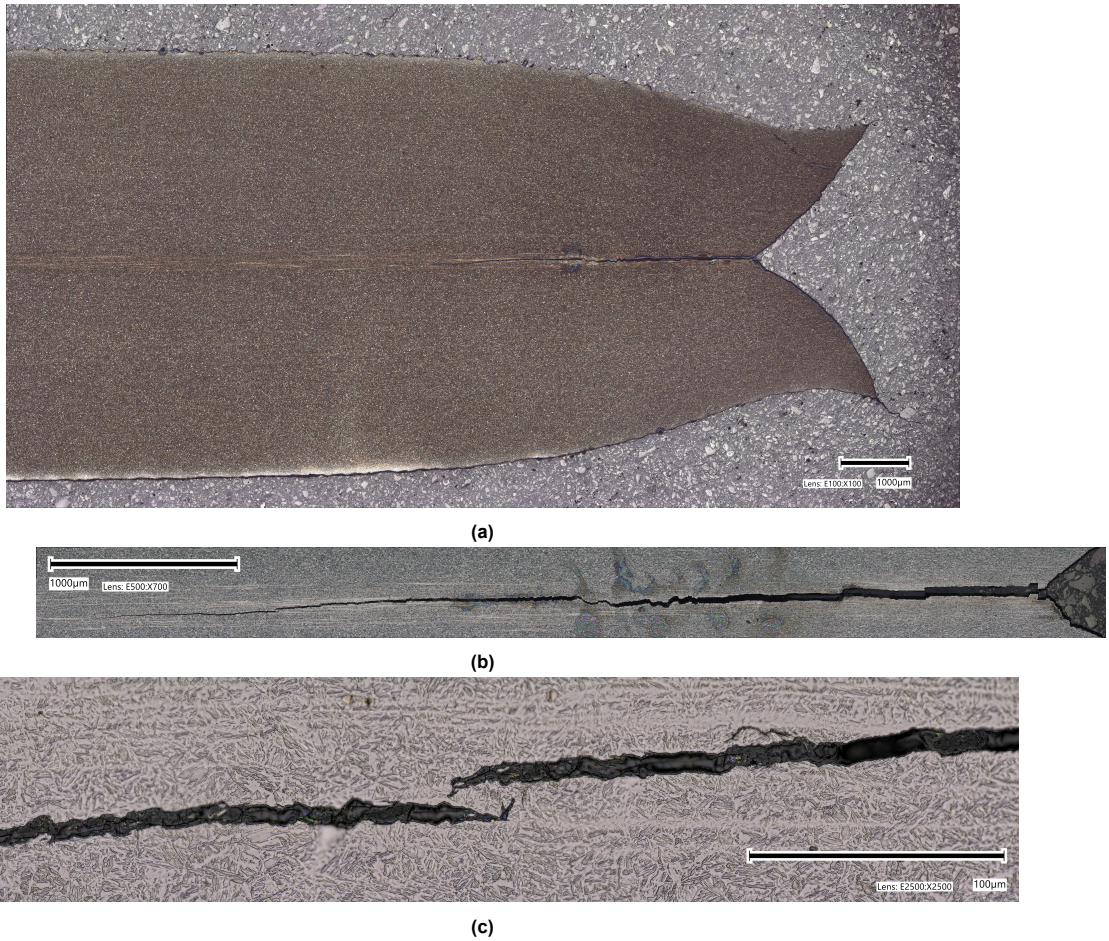


Figure A.5: Cross section of fractured surface of plate A1-900 m/s, cross section 2b in shear direction of the full fracture, (a) Full cross section, (b) Zoomed in on central crack, (c) higher magnification of local crack interruption.

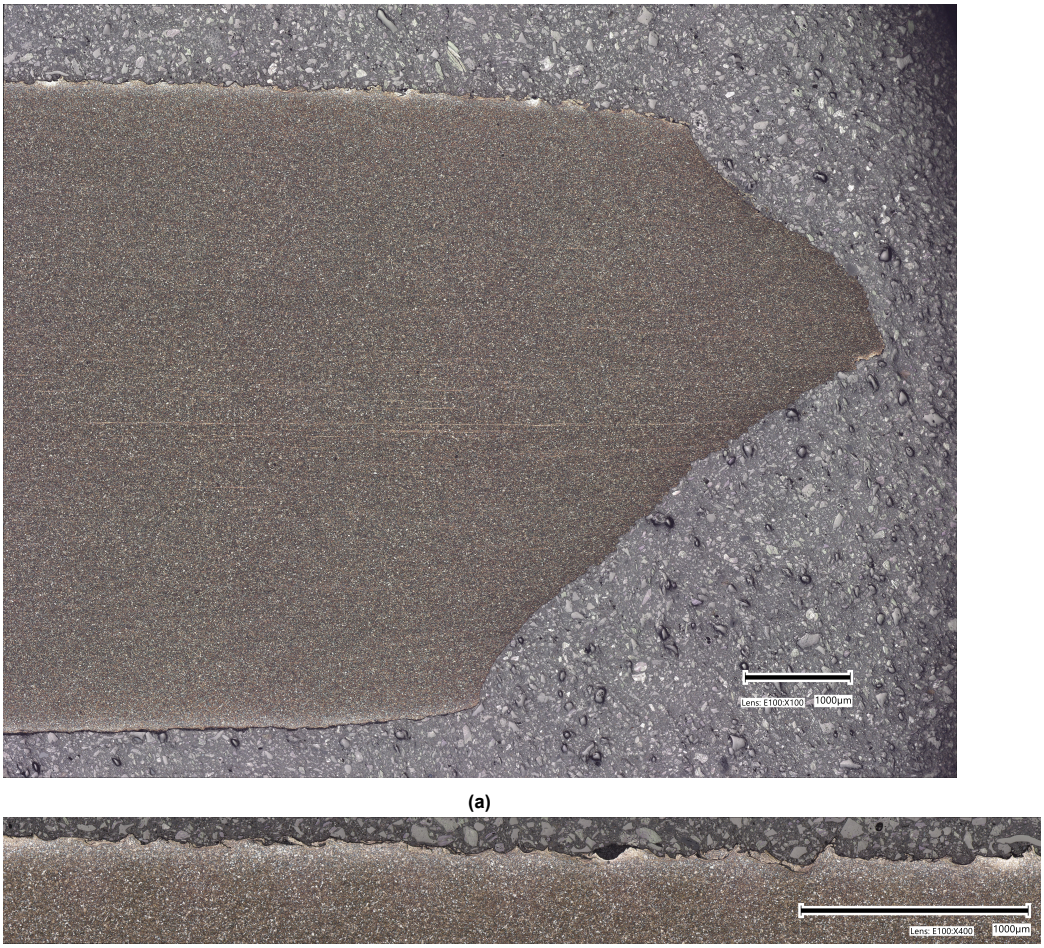


Figure A.6: Cross section of fractured surface of plate A4-1600 m/s, cross section 1b in initial section of the full fracture, (a) Full cross section, (b) Zoomed in on the backside of the plate showing adiabatic shear band formation from DWI test.

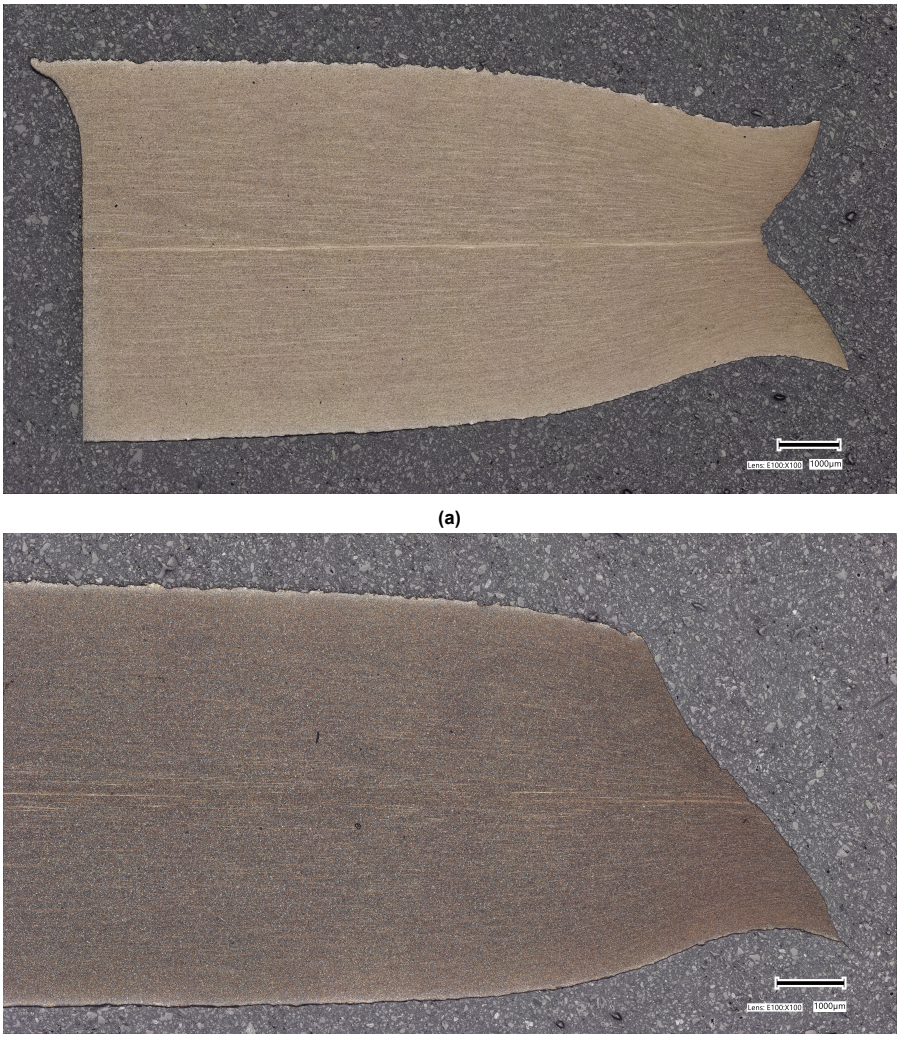


Figure A.7: Cross section of fractured surface of plate A4-1600 m/s in shear direction of the full fracture showing clear necking behaviour, (a) cross section 3 showing V crack shape, (b) cross section 4 showing single shear direction crack shape.

A.4. Adiabatic shear bands along hole surface



Figure A.8: Leftover transformed adiabatic shear band pieces along shot hole surface at 900 m/s

A.5. EDS results of Adiabatic shear band

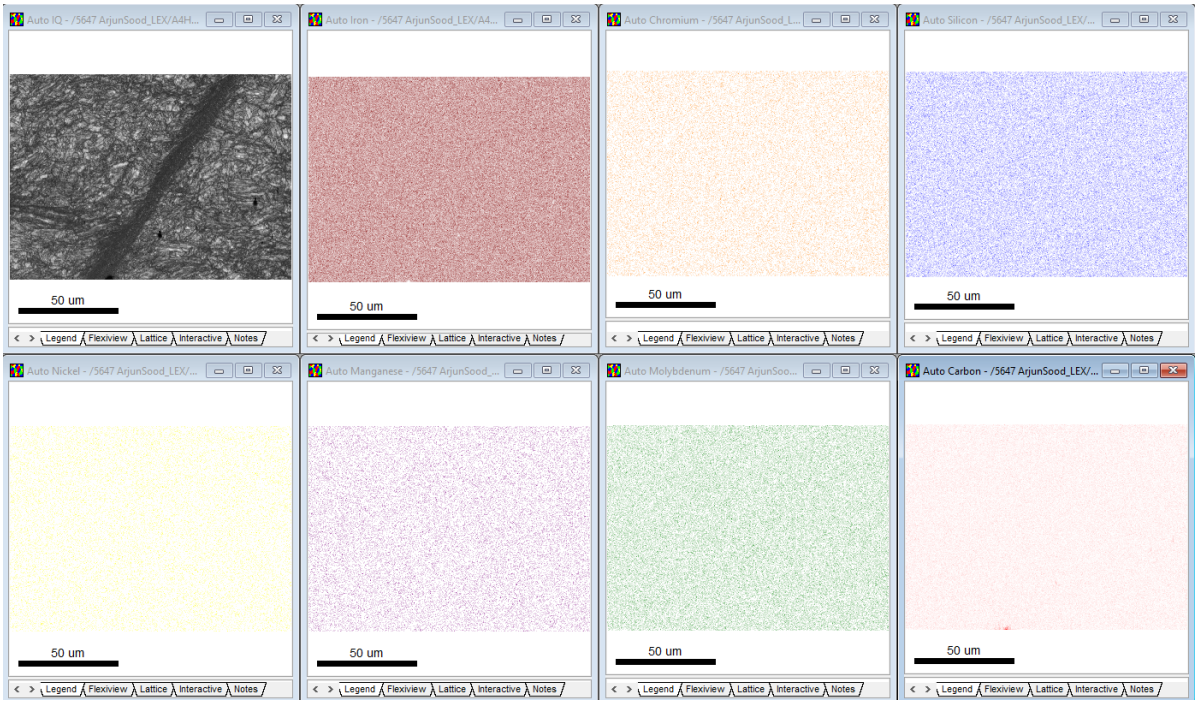


Figure A.9: EDS results on transformed adiabatic shear band from sample A4-1600 m/s, showing no elemental segregation.

B

Appendix B: External result files

In this appendix the external XRF and XRD results are presented as well as an extend Drop Weight Impact test analyses from the DIC results

B.1. XRF results on Armox 440T

Materials Science and Engineering
TUDelft, Faculty of 3mE
Mekelweg 2
2628 CD Delft, The Netherlands
Tel:015-2789459
Email: R.W.A.Hendrikx@tudelft.nl

X- ray diffraction facilities

Experimental conditions:

For XRF analysis the measurements were performed with a Panalytical Axios Max WD-XRF spectrometer and data evaluation was done with SuperQ5.0i/Omnian software. 18/12/2015 09:37:03

10/11/2024 3:33:02 PM

PANalytical

Quantification of sample Lex van der Wekken, sample "Armox", 11oct24

Sum before normalization: 102.5 wt%

Normalised to: 100.0 wt%

Sample type: Solid

Correction applied for medium: No

Correction applied for film: No

Results database: omnian 4kw 27mm

Results database in: c:\panalytical\superq\userdata

	Compound Name	Conc. (wt%)	Absolute Error (wt%)
1	Fe	95.746	0.1
2	Ni	1.956	0.04
3	Mn	0.764	0.03
4	Mo	0.573	0.02
5	Cr	0.53	0.02
6	Si	0.265	0.02
7	Al	0.05	0.007
8	Cu	0.046	0.006
9	V	0.04	0.006
10	Nb	0.018	0.004
11	P	0.013	0.003

Use of our XRD or XRF analysis:
In a publication: 'PersonX at the Department of Materials Science and Engineering of the Delft University of Technology is acknowledged for the X-ray analysis. If it is an important part of the publication: a co-authorship is preferred. It is useful to involve us in the preparation of any presentation!

B.2. XRD results on Armox 440T focussed on tASB and undeformed material

X-RAY FACILITIES GROUP

Dr. Amarante Böttger

Dhr. Ruud Hendrikx
Drs. Richard Huizenga

Delft University of Technology, Faculty of 3mE
Department of Materials Science and Engineering
Mekelweg 2, NL-2628 CD Delft, the Netherlands, phone +31(0)1527·82255 / 82480

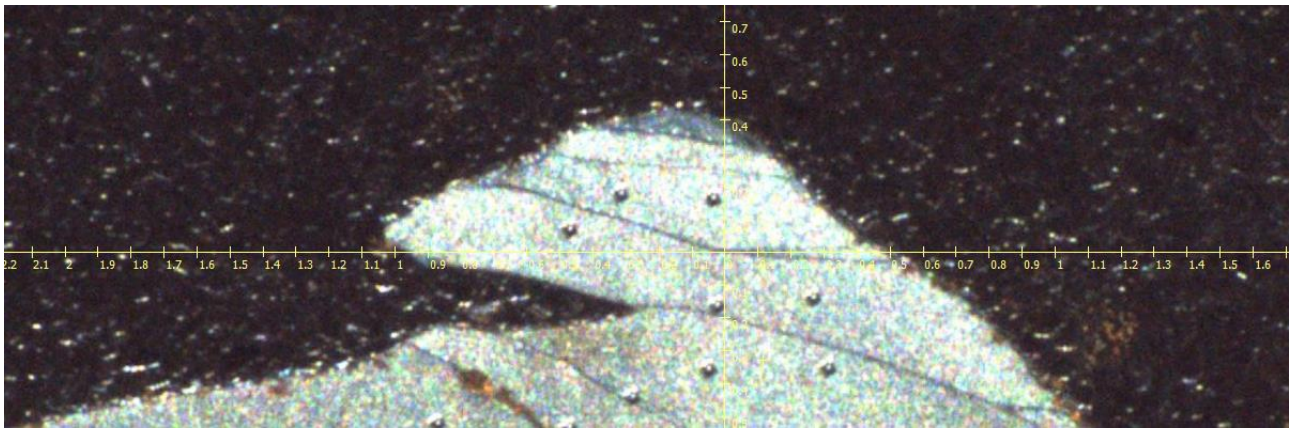
Analysis of shear bands

Author	:	Richard Huizenga
Client	:	Lex van der Wekken, MSE
Research question	:	Phase identification

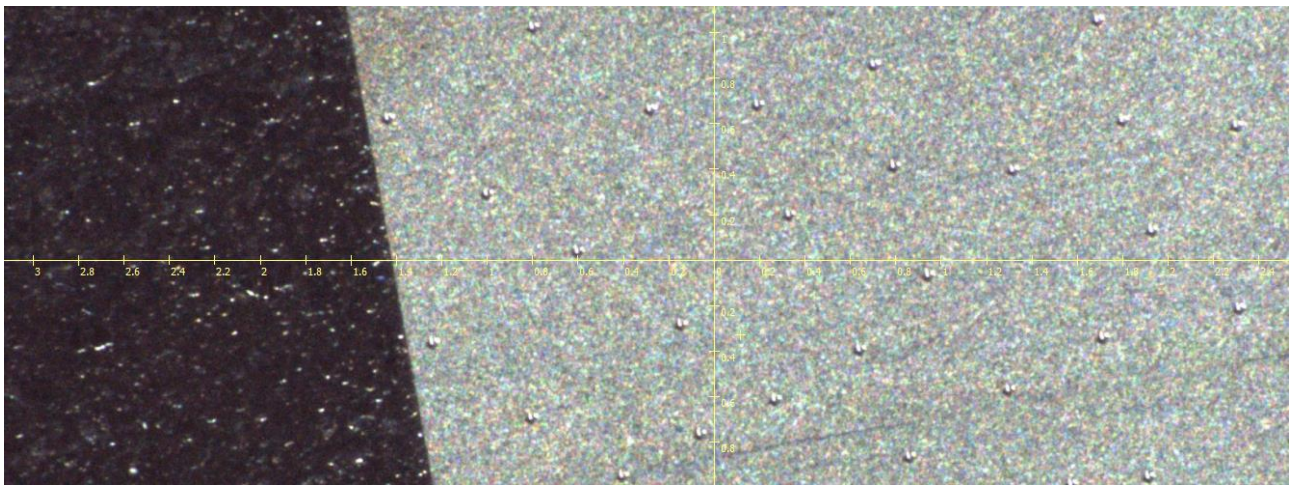
Samples
Steel sample with shear bands (~ 6 mu thick)

Specimens
The sample was put on standard holder. 2 positions are measured:

Pos1:



Pos2:



Experimental
Instrument: Bruker D8 Discover diffractometer, Incoatec Microfocus Source (IμS).
50 kV 1000 μA, Cu Kα radiation. Montel Optics ELM32 with parallel beam, UBC collimator 0.1 mm. UMC 1516 sample stage, Eiger 2 500k detector. Detector settings: LL=7200 keV.

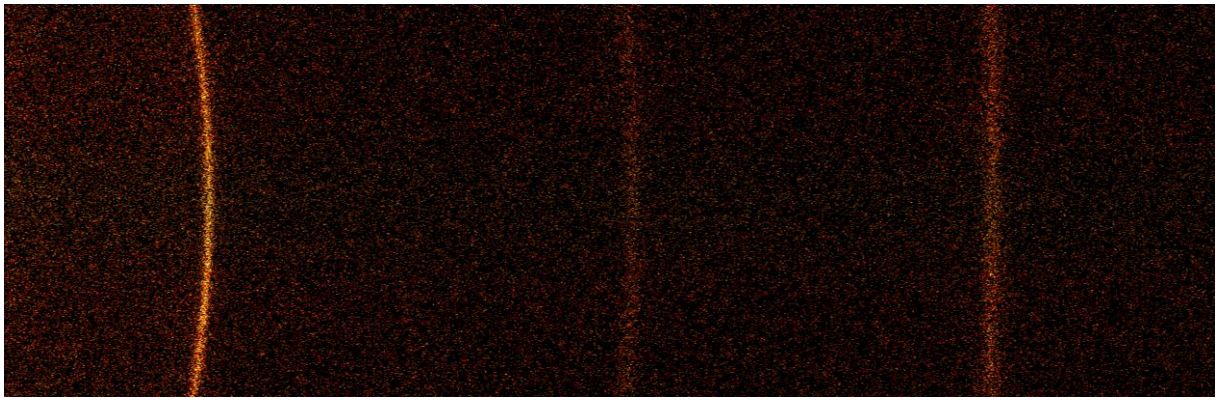
Measurements
Coupled Theta/2theta scan: step size 0.05 º 2θ, counting time per step 2s.

Data evaluation
Bruker software DiffracSuite.EVA vs 7.3

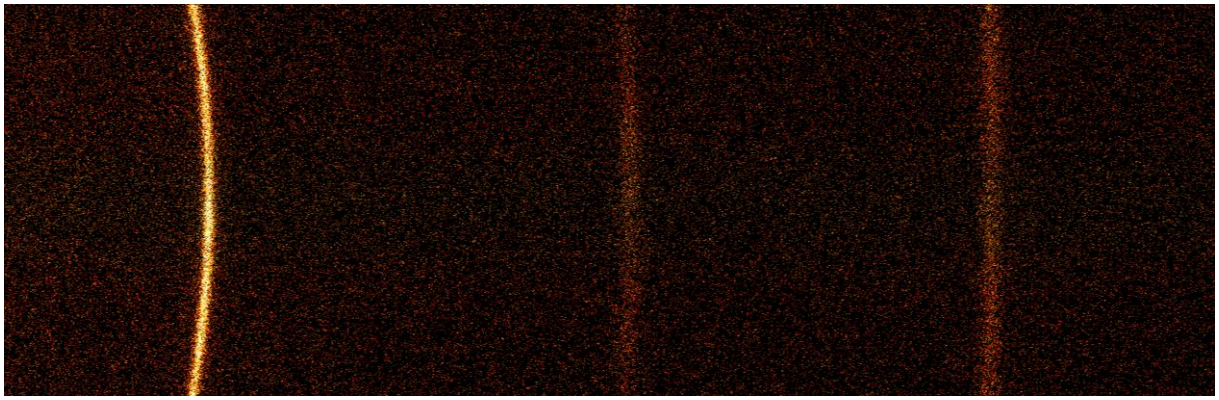
Results
On the following pages the measured XRD patterns are shown.

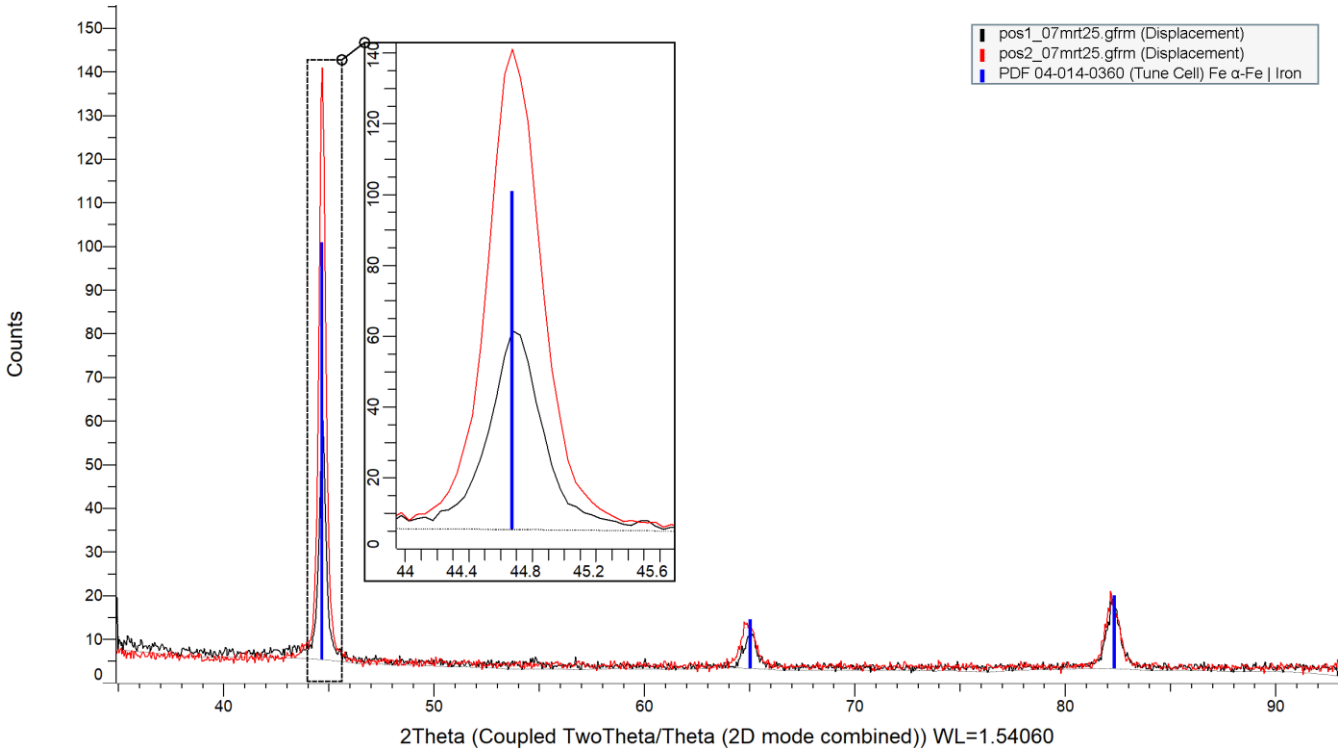
If the analysis is a significant part of a publication, a co-authorship is preferred.
In any case, it is useful to involve us in the preparation of any presentation to ensure optimum and correct use of the analysis results!
Whenever used in a publication, an acknowledgement will be appreciated, e.g.:
"personX at the Department of Materials Science and Engineering of the Delft University of Technology is acknowledged for the X-ray analysis".

Pos 1:



Pos 2:





- In both positions only BCC ferrite / bainite / martensite is detected. No clear austenite peaks are seen.
  Note that BCT is difficult to detect if it is very close to BCC, i.e. the a/c ratio is almost 1.

- Both positions have a fine grain size; seen by the continuous rings (no individual spots are detected).

- The Fe-(110) peak (1st peak around 2theta= 45 deg) is relatively weaker than normal in pos1, while in pos2 it appears slightly stronger (the 'normal' intensity for random texture is roughly indicated by the height of the blue bars). This could indicate a difference in the texture (preferred orientation).

B.3. Extended Drop Weight Test DIC analysis

Armox 440T Drop Weight Test analysis

Author: Lex van der Wekken: 06-08-2025

Table 1 provides rough estimated values for the far field strain of the shot hole Armox 440T plates during drop weight test loading. These values are taken just before visible cracks form and right after full fracture when the elastic strain is recovered and plastic strain maintains.
The rolling direction is expressed with respect to the length of the plate: RD – plate length is along rolling direction, TD – plate length perpendicular to the rolling direction.

It is interesting to note that from this data the residual plastic strain for RD samples show more plastic deformation at fracture. This can be caused by the different deformation behaviour, as it is seems that in general the RD samples experience global elongation before failure, whereas the TD show clear banded straining from the hole to the sides of the plate as shown by figure 1-4. This indication is challenging to read due to the limit of the scalebar, except for the dynamic scale bar used in sample A4.

Drop weight mass: 9100 kg

Table 1: Rough estimate of far field strain from visual DIC data related to crack growth and full fracture of shot hole Armox 440T plates during drop weight test loading.

Sample ID	Rolling direction	Hole diameter	Average/Far field strain at crack growth	Plastic strain after fracture
		[mm]	%	%
A1	RD	24.1	1.1	0.5-0.6
A2	RD	24.1	…	…
A3	RD	24.1	…	…
A4	RD	31.6	1.1	0.5-0.6
A5	RD	31.8	1.0	0.4-0.5
A6	TD	24.4	0.8	0.1
A7	TD	24.2	0.7	0.05
A8	TD	24.5	0.7	0.1-0.15
A9	TD	31.4	0.6-0.7	0.2

Figures of consecutive frames of first sign of crack growth, at the point of significant fracture and at full fracture. For DIC results available for samples: A1, A4, A5, A6, A7, A8, A9

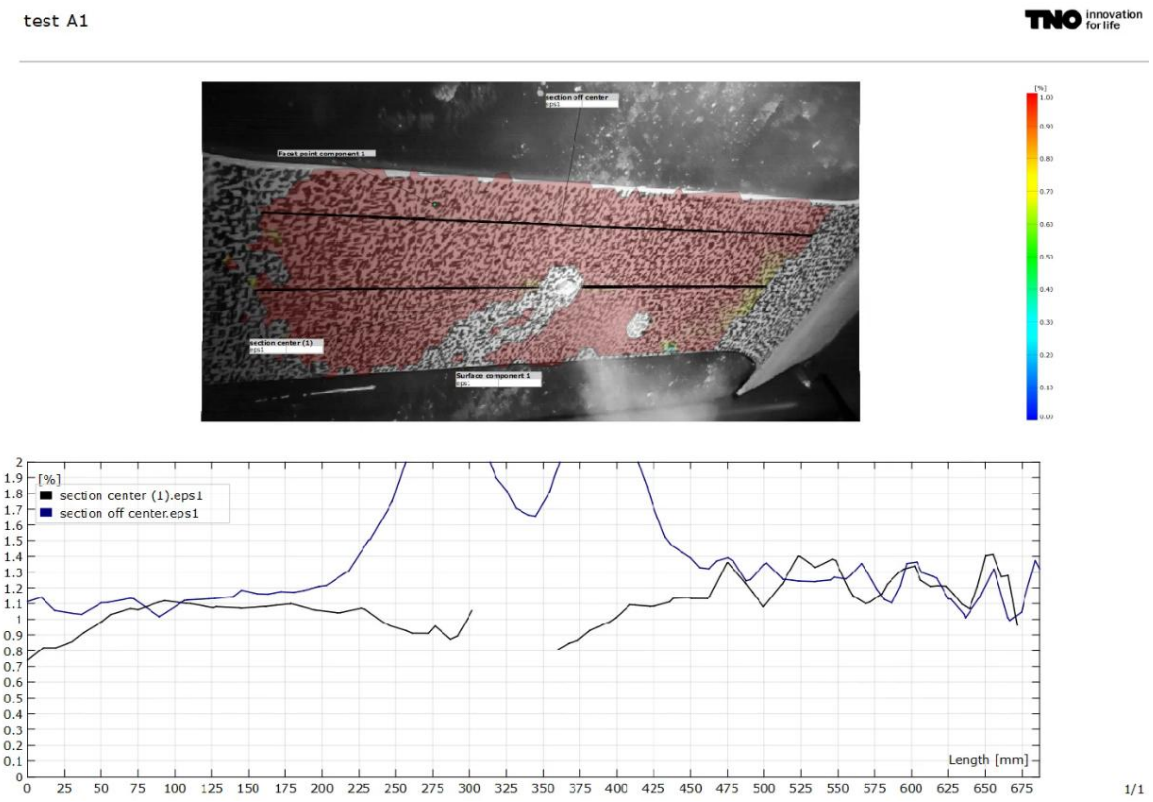


Figure 1a: Sample A1 right before crack growth.

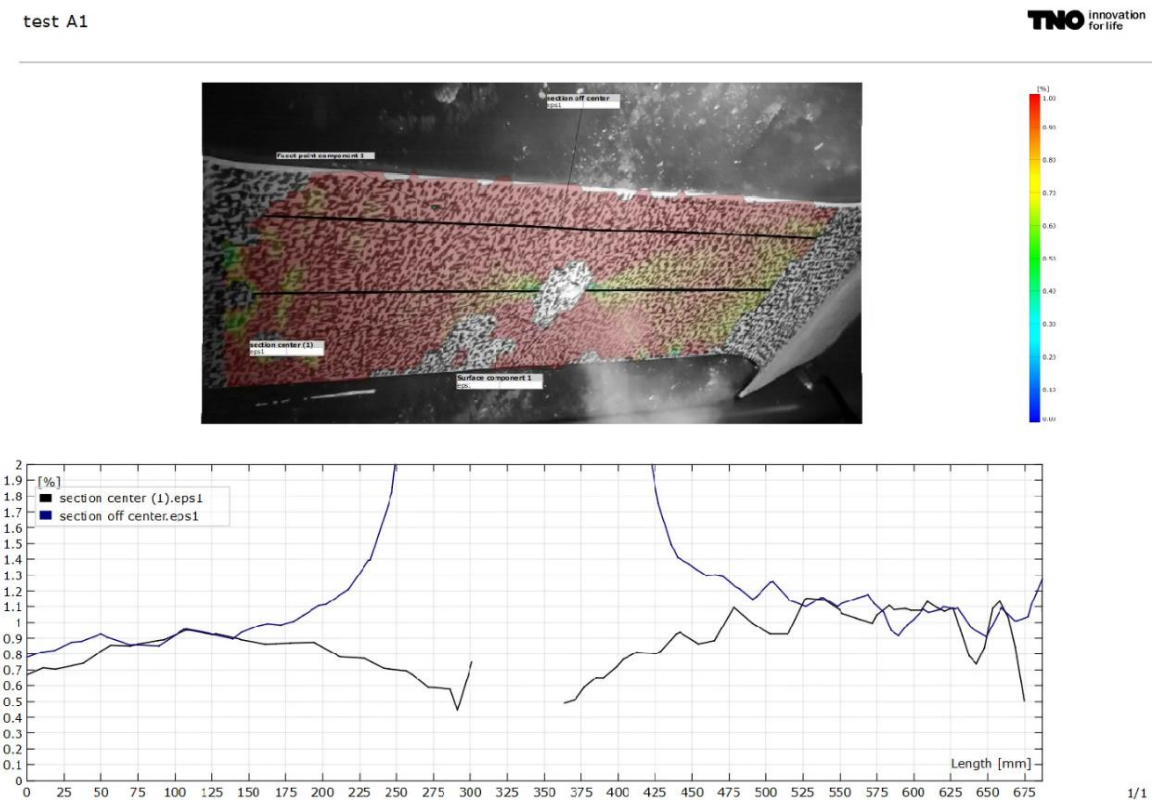


Figure 1b: Sample A1 crack growth.

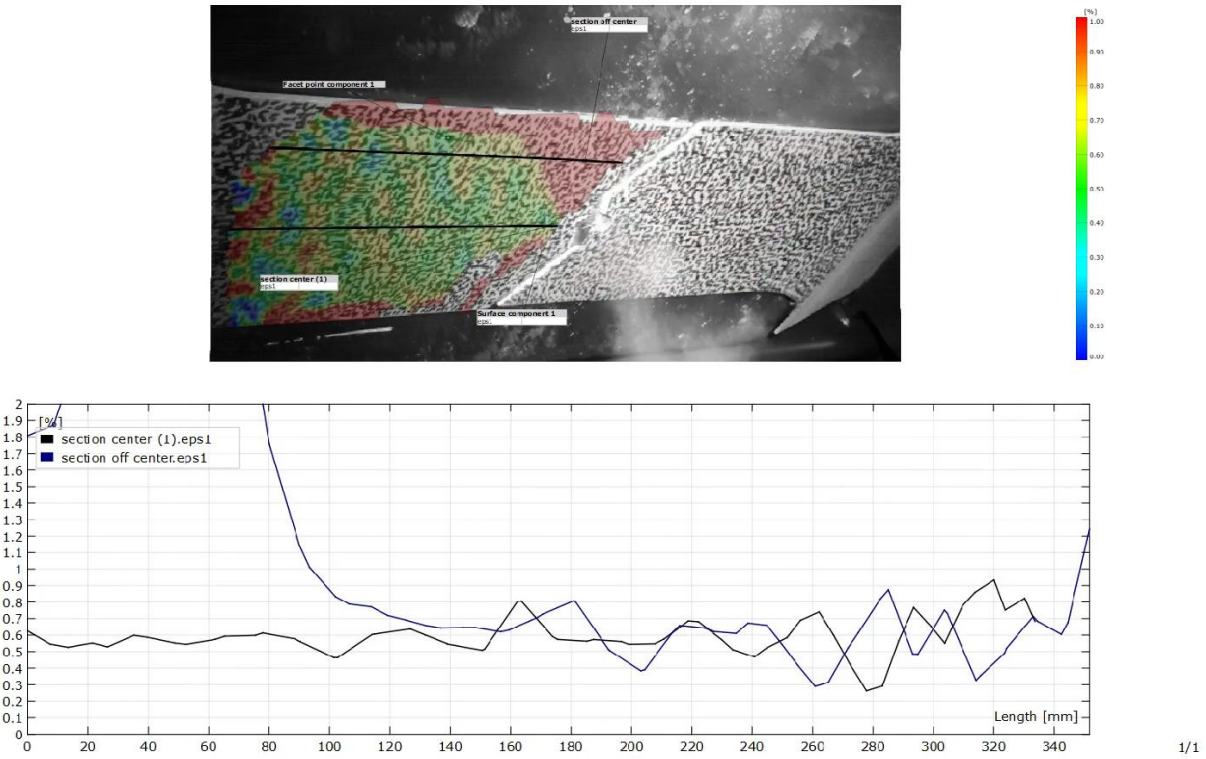
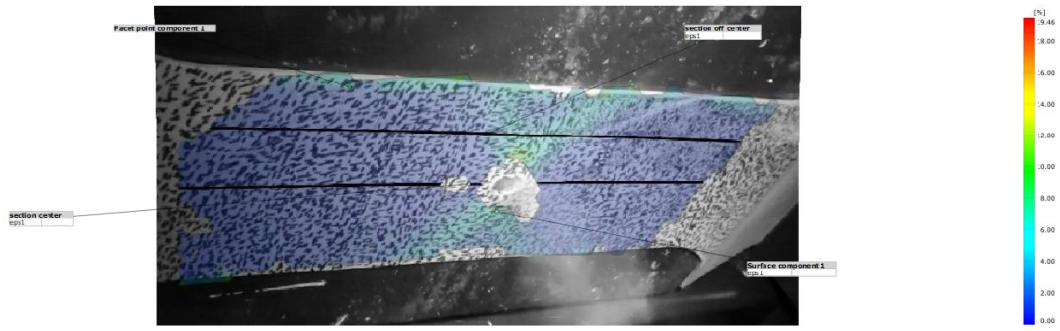


Figure 1c: Sample A1 full fracture.



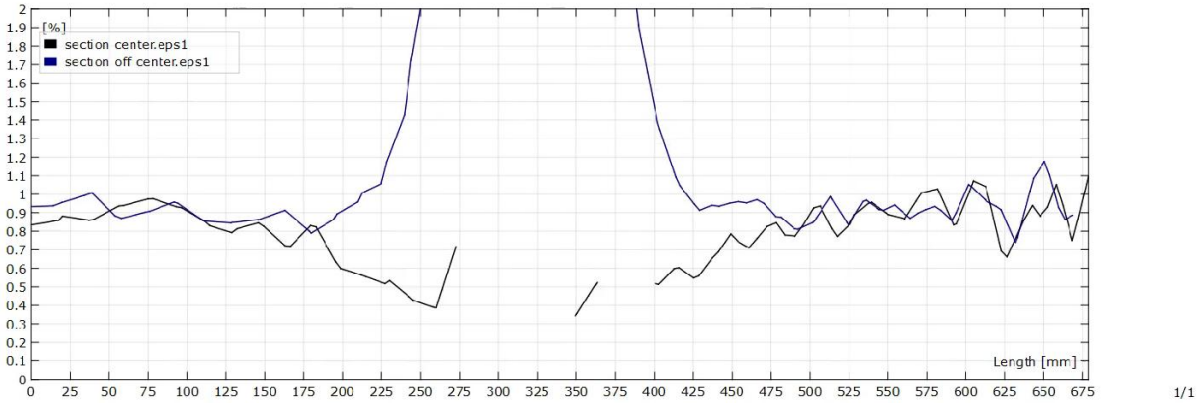
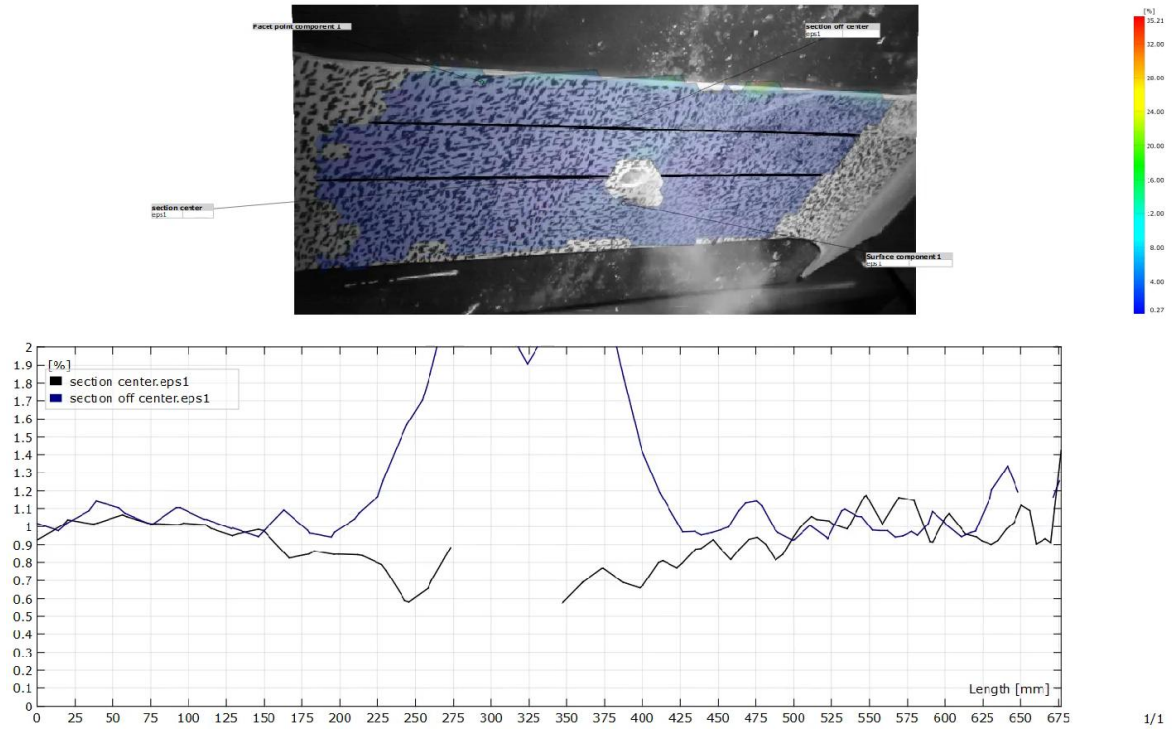
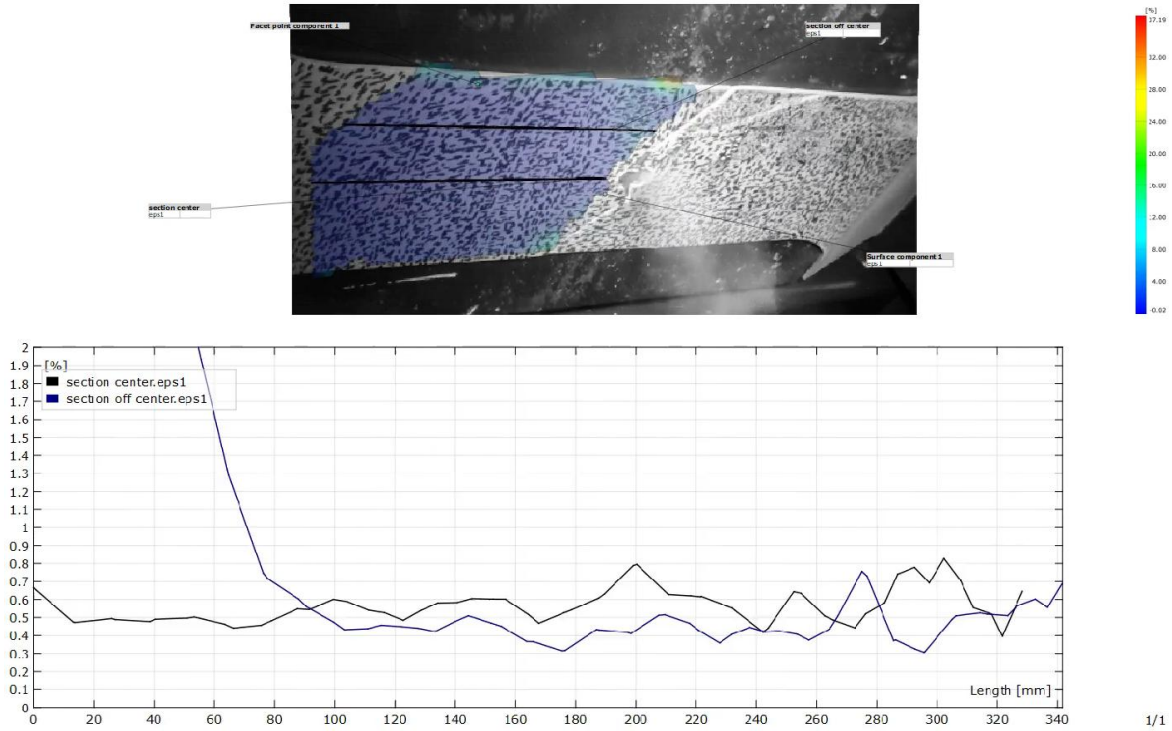


Figure 2a: Sample A4 right before crack growth.



1/1

Figure 2b: Sample A4 crack growth.



1/1

Figure 2c: Sample A4 full fracture.

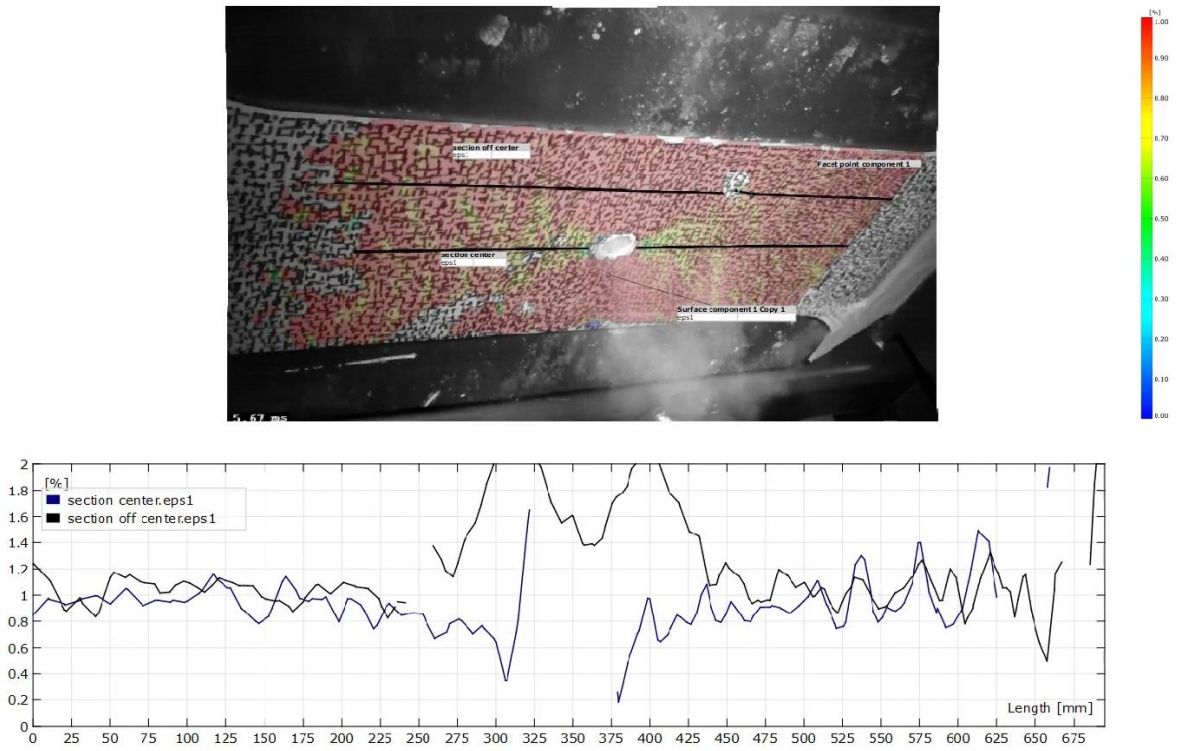
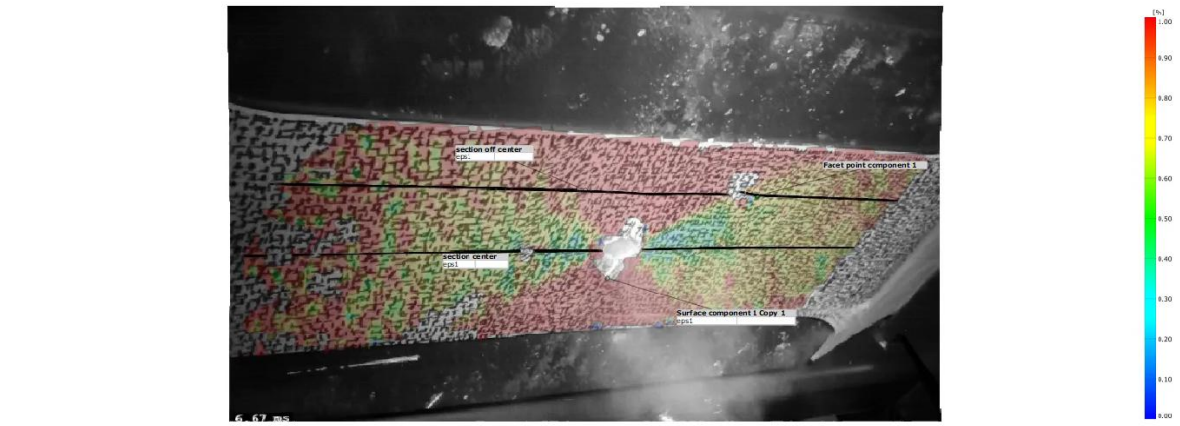


Figure 3a: Sample A5 right before crack growth.



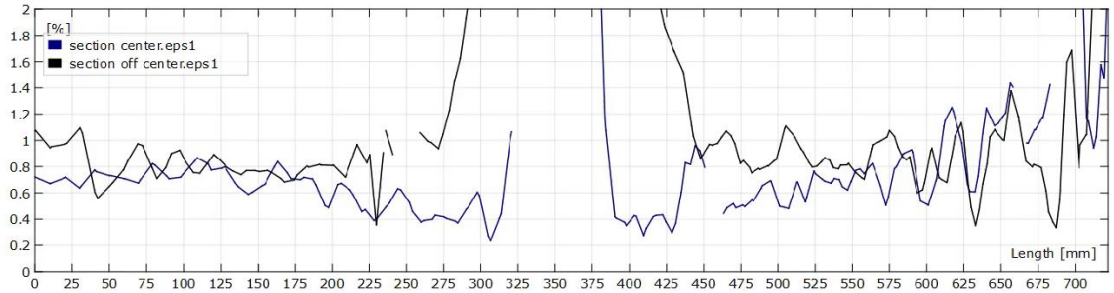
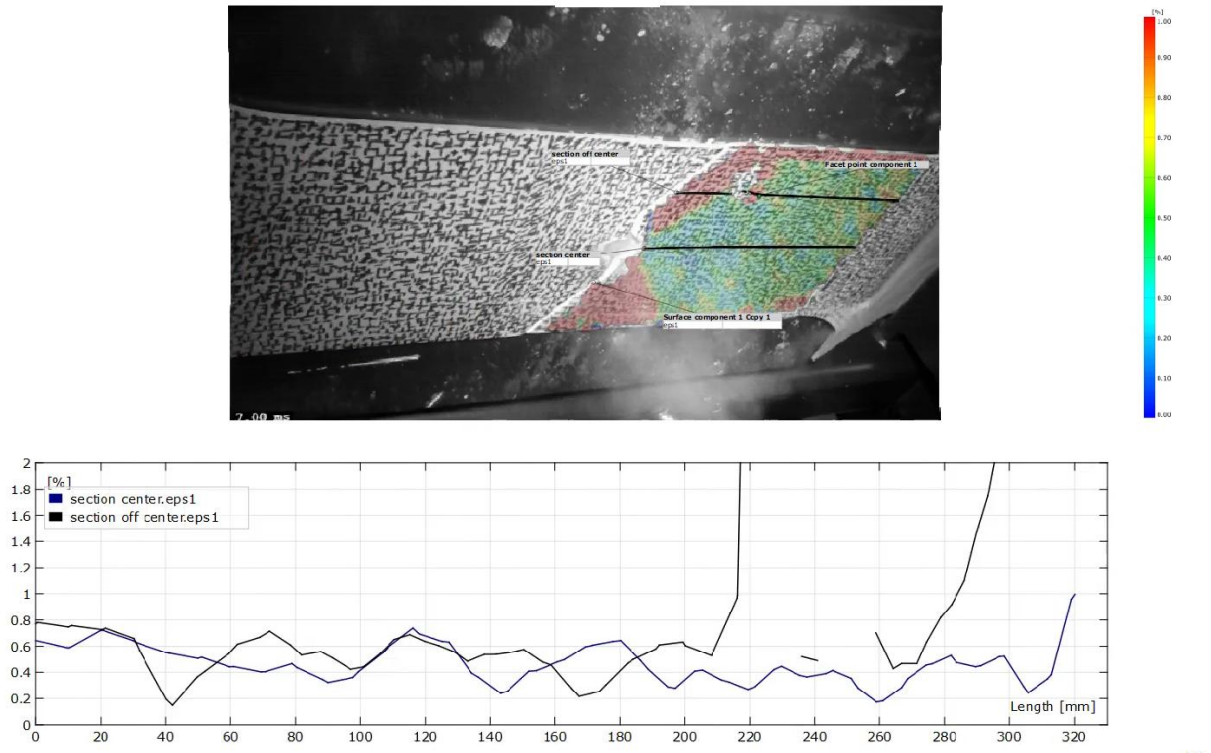
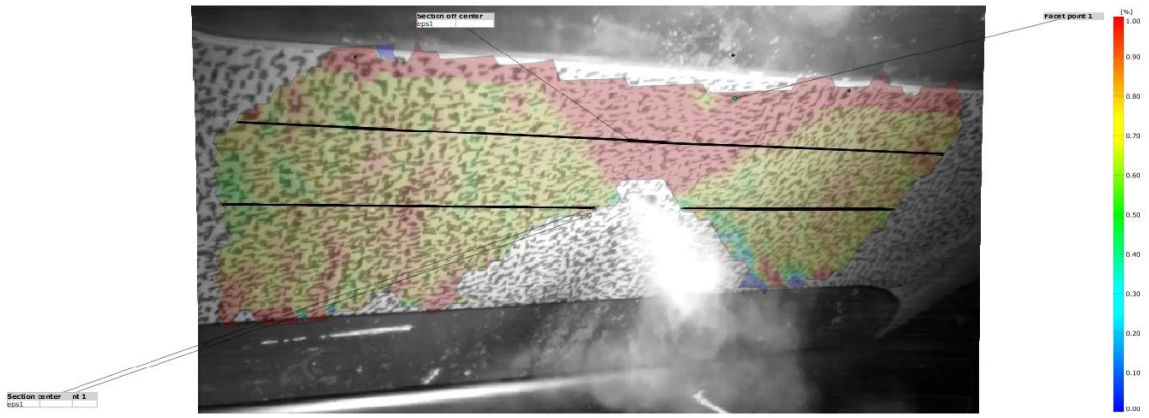


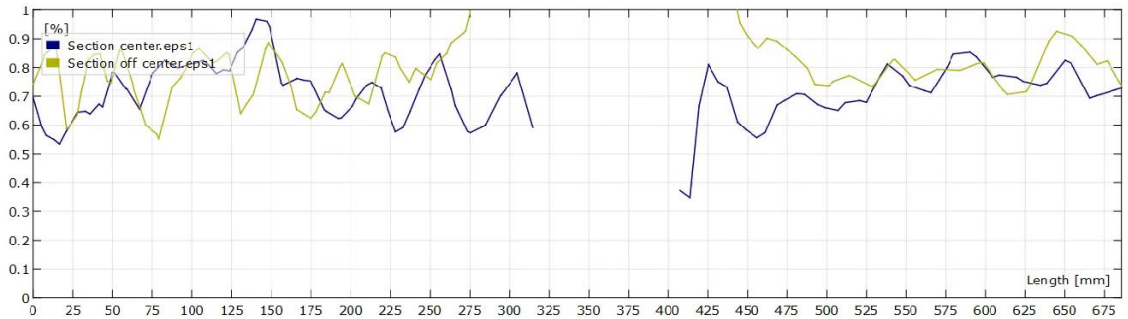
Figure 3b: Sample A5 crack growth.



1/1

Figure 3c: Sample A5 full fracture.





1/1

Figure 4a: Sample A6 right before crack growth.

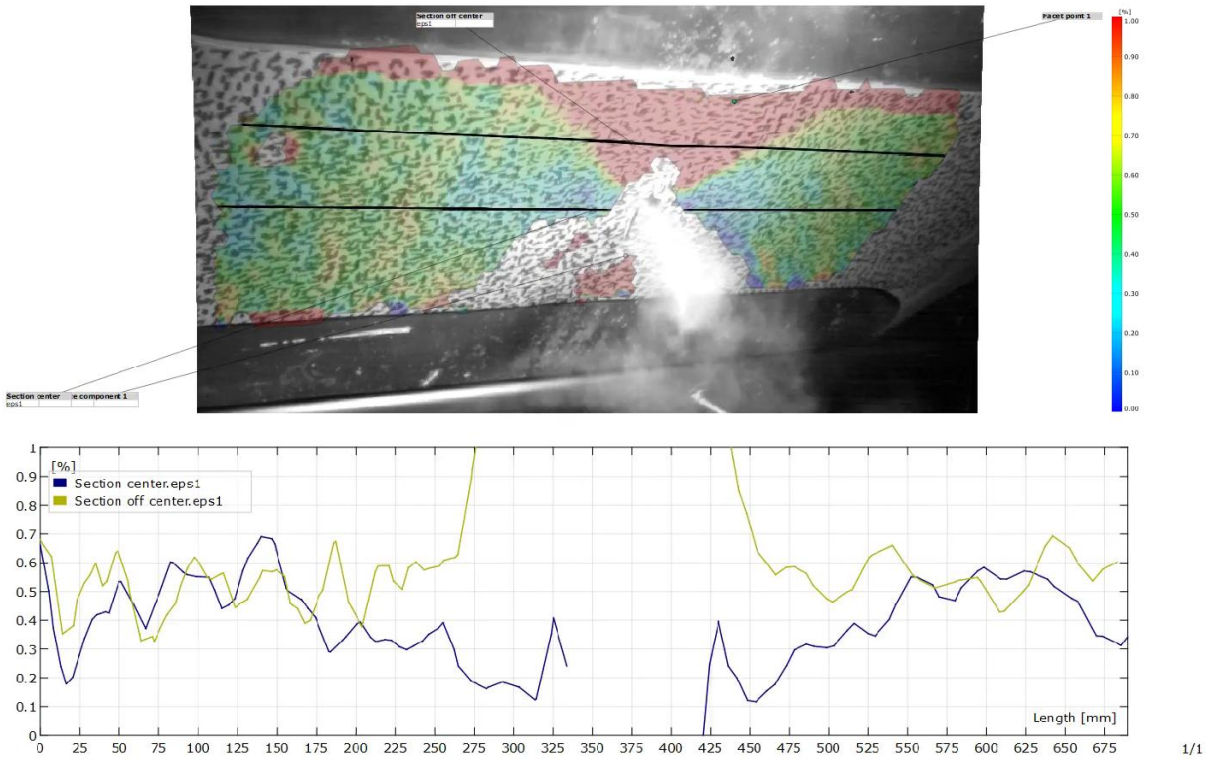


Figure 4b: Sample A6 crack growth.

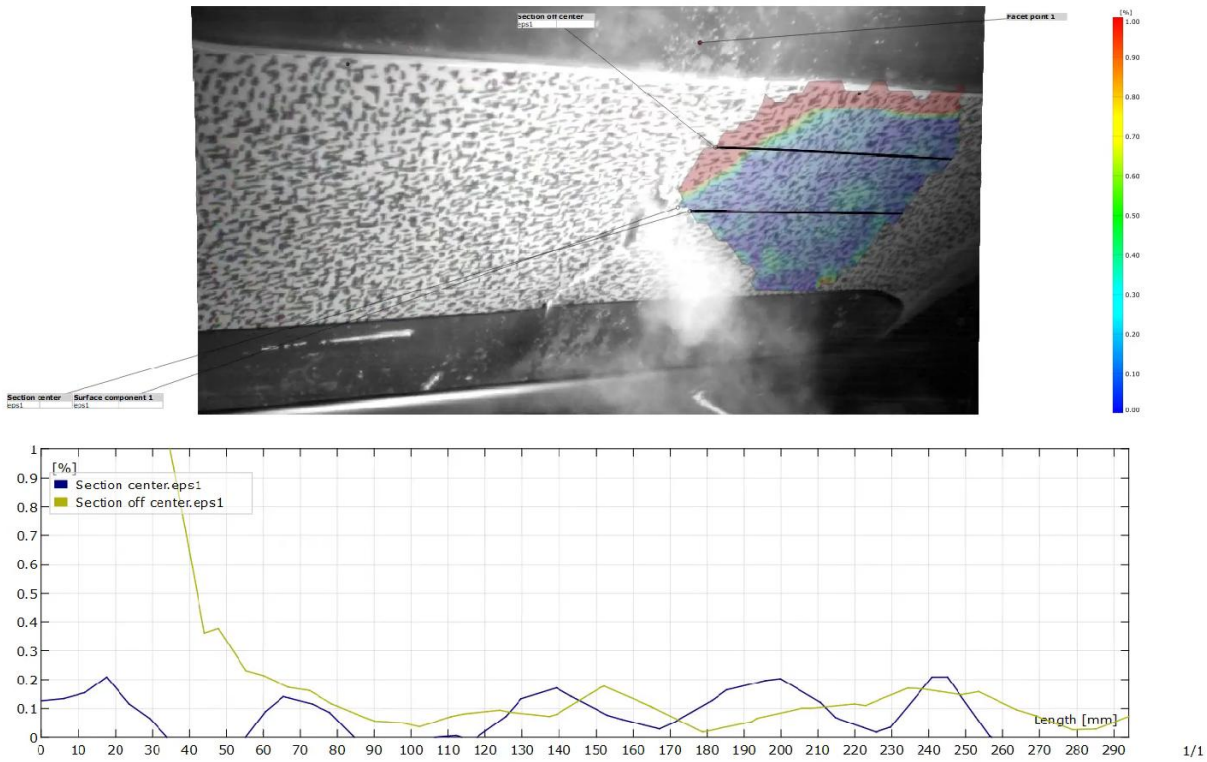
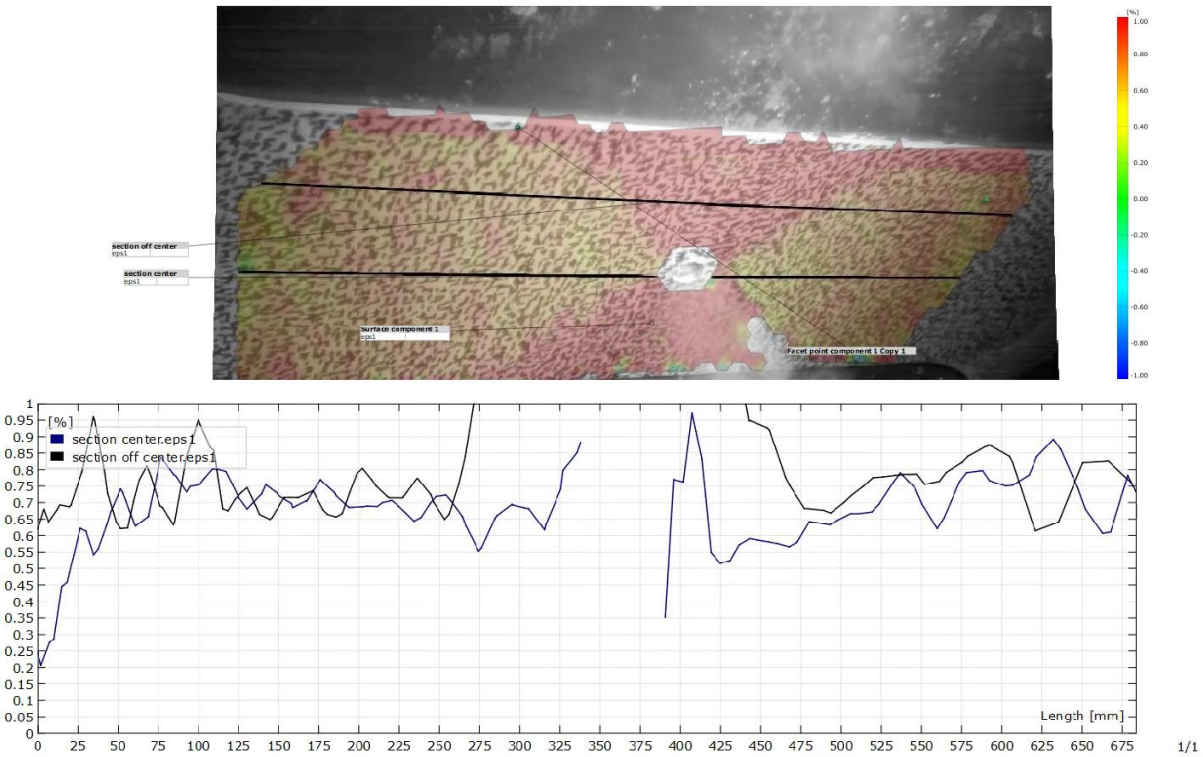
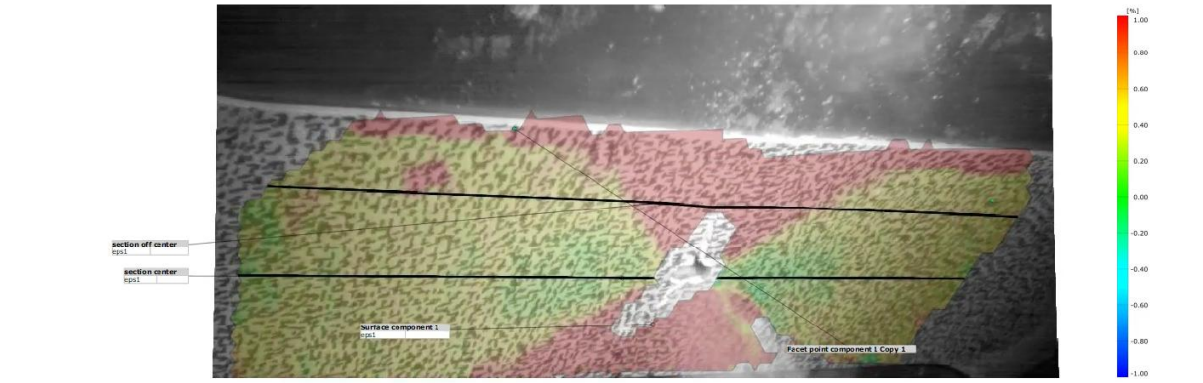


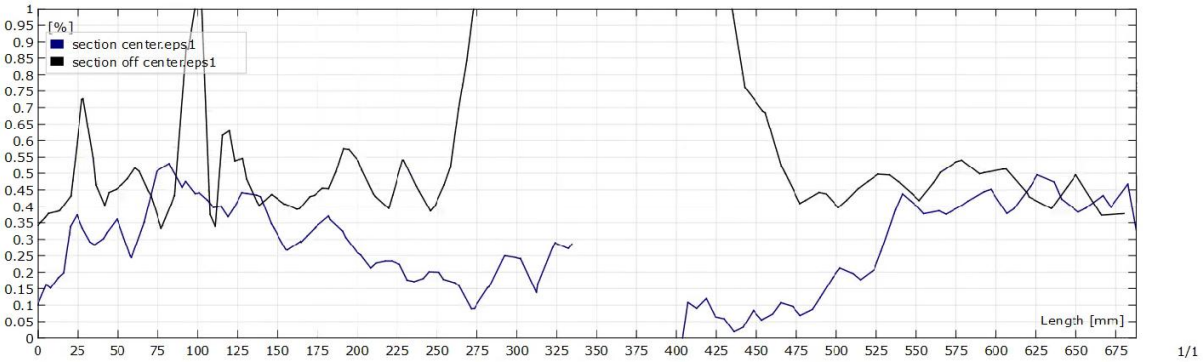
Figure 4c: Sample A6 full fracture.



1/1

Figure 5a: Sample A7 right before crack growth.





1/1

Figure 5b: Sample A7 crack growth.

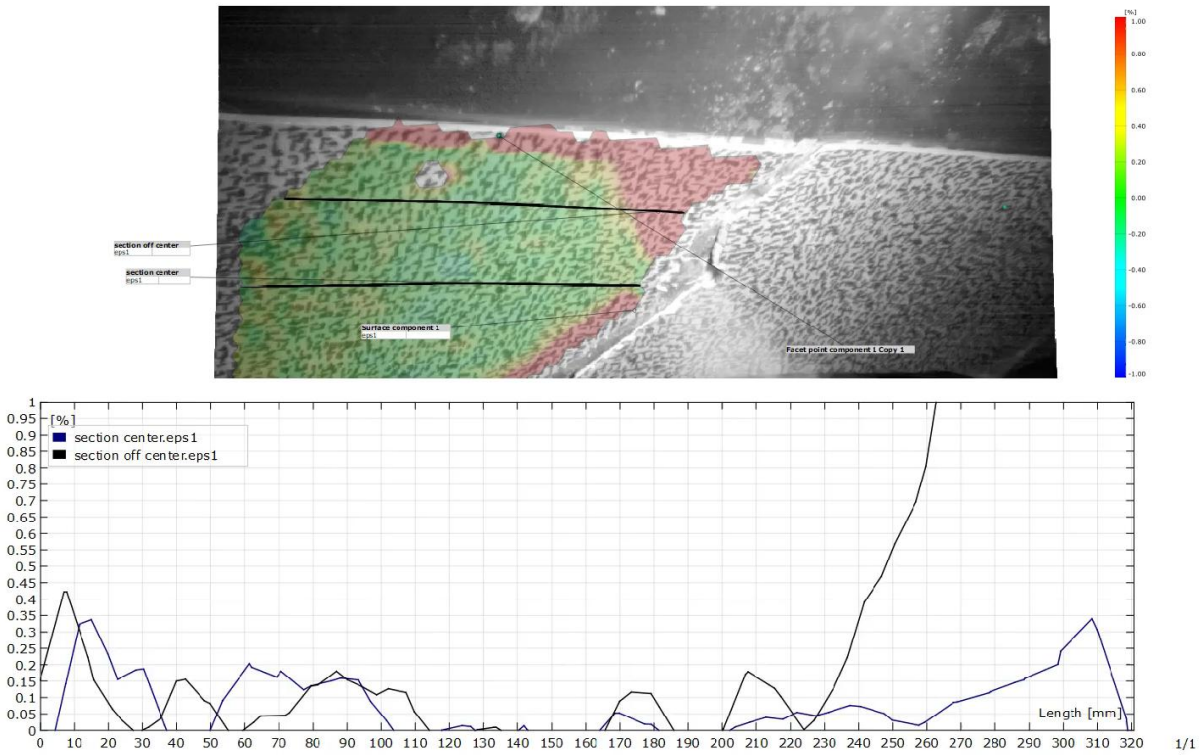
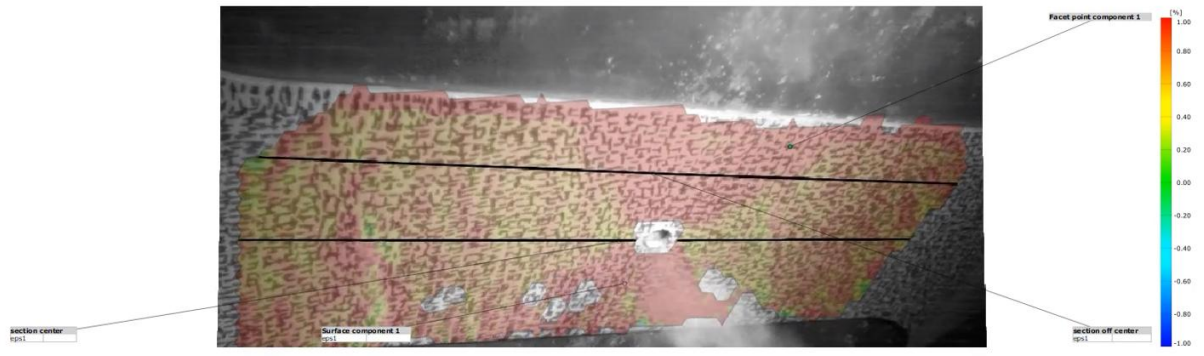


Figure 5c: Sample A7 full fracture.



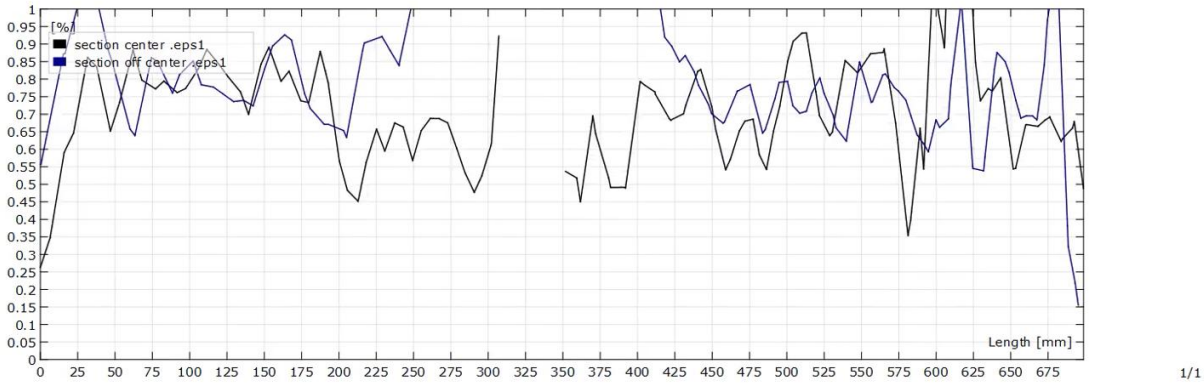
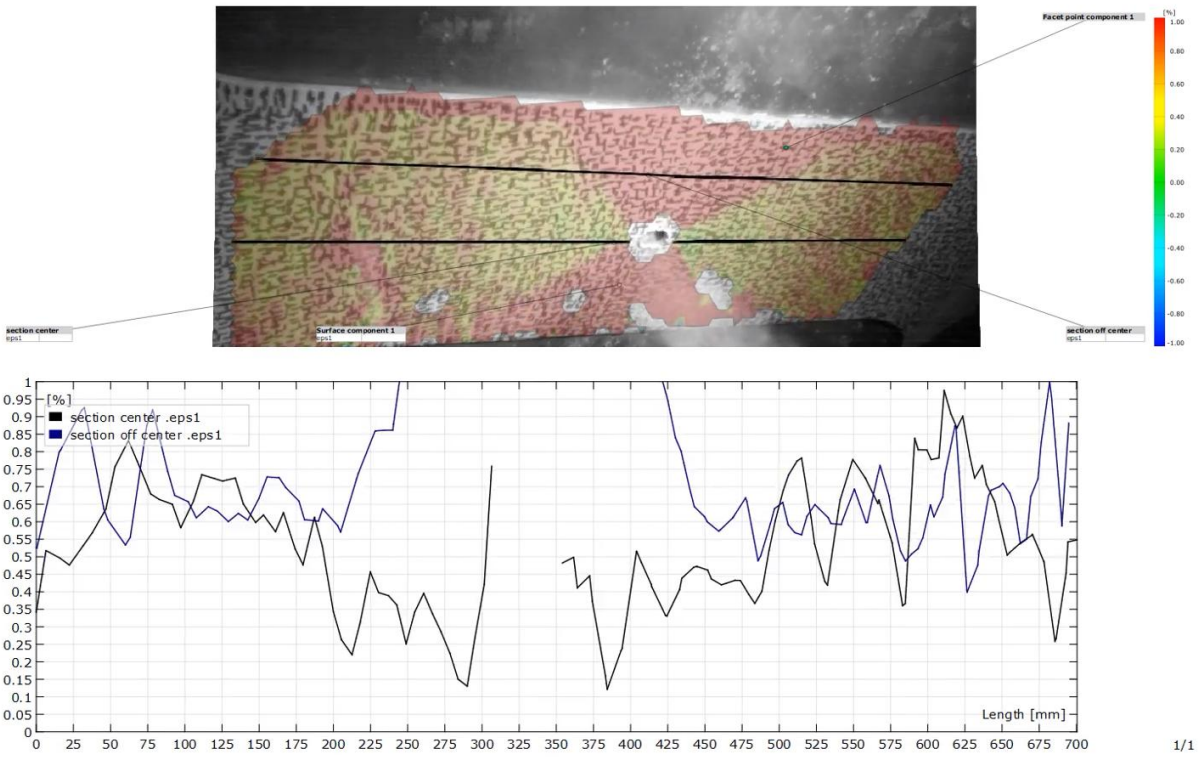
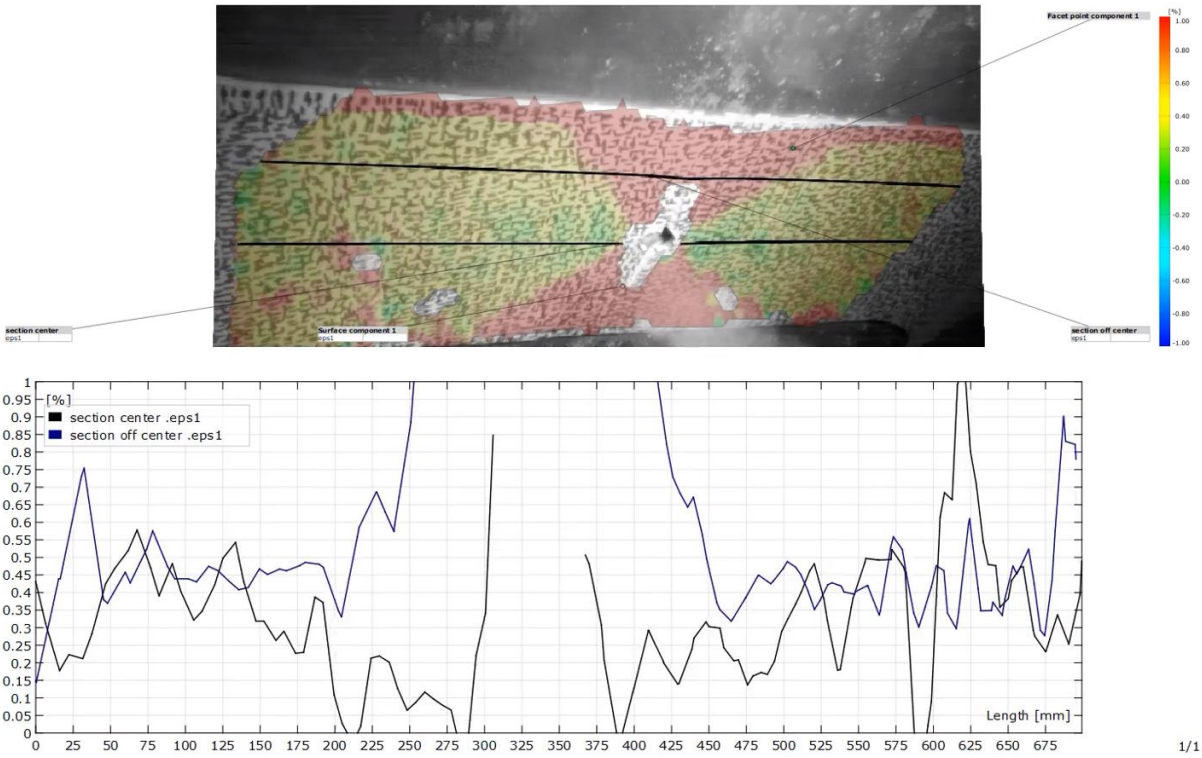


Figure 6a: Sample A8 right before crack growth.



1/1

Figure 6b: Sample A8 crack growth frame 1.



1/1

Figure 6c: Sample A8 crack growth frame 2.

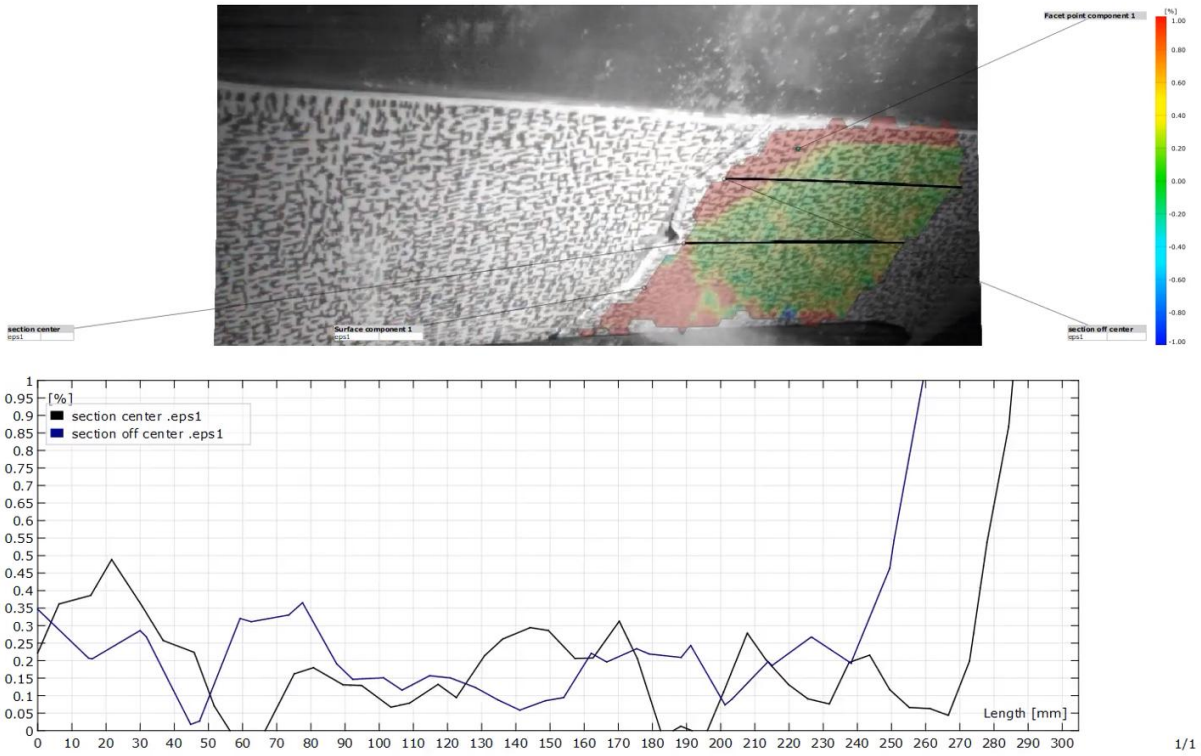


Figure 6d: Sample A8 full fracture.

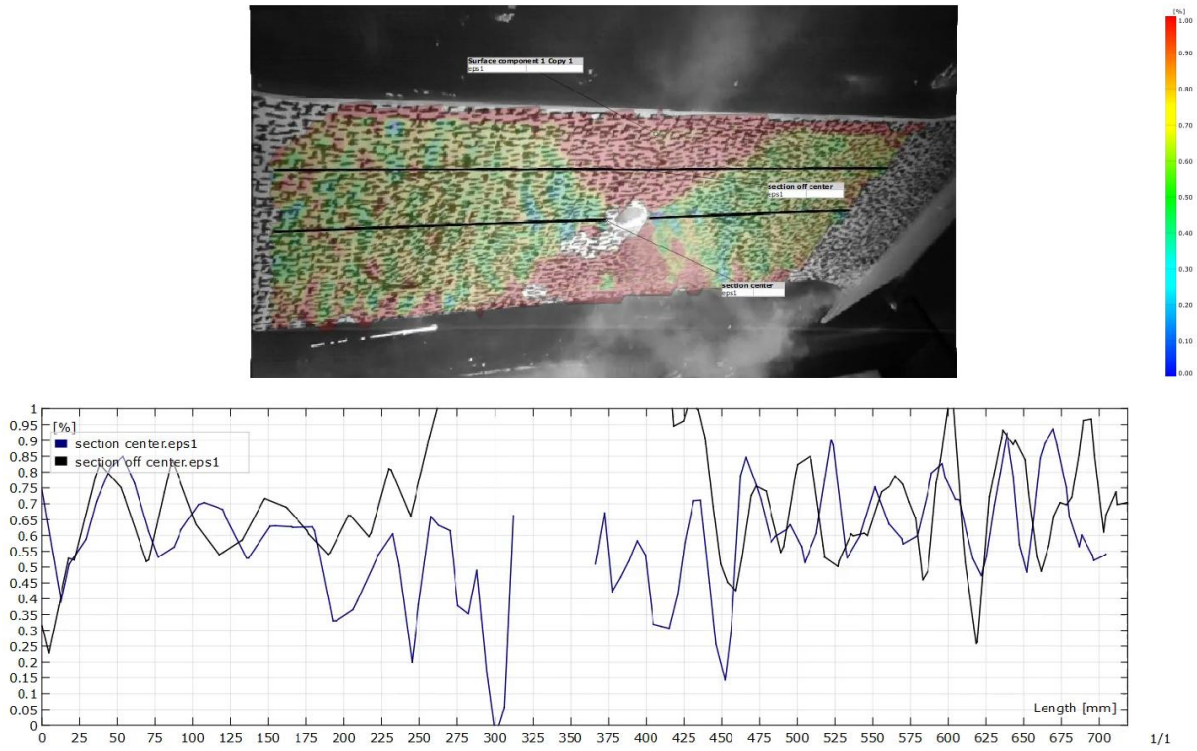


Figure 7a: Sample A9 right before crack growth.

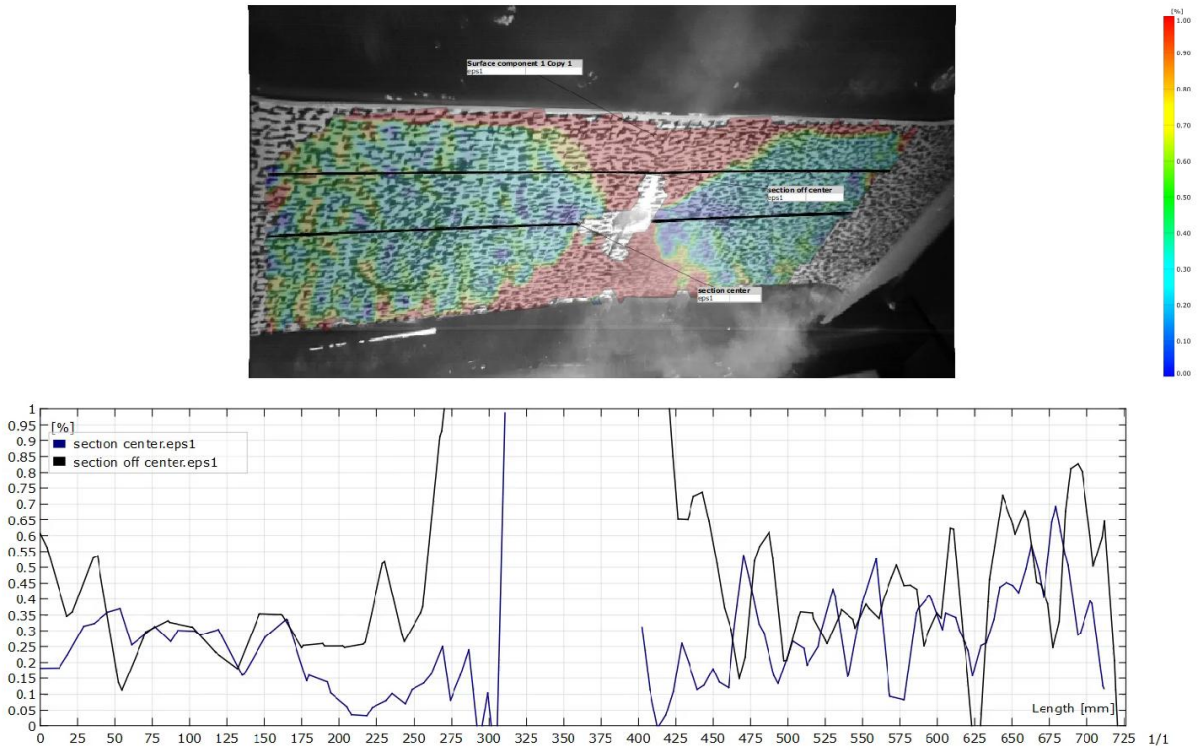


Figure 7b: Sample A9 crack growth.

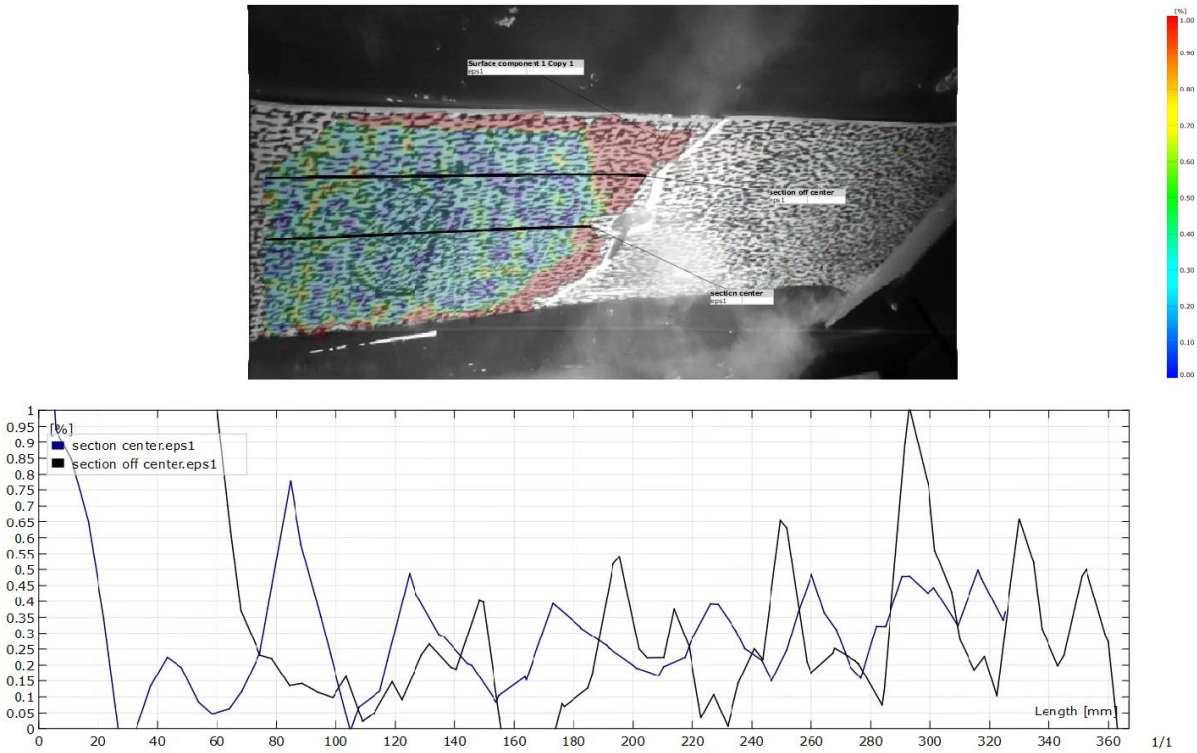


Figure 7c: Sample A9 full fracture.